ABSTRACT

PERELYGIN, VLADISLAV R. Local Properties of Bio- and Nanointerfaces by Spin Labeling EPR. (Under the direction of Professor Alex I. Smirnov).

Spin labeling Electron Paramagnetic Resonance (EPR) is an extremely versatile tool that allows for obtaining local physicochemical properties of various molecular and nanoscale systems. This work summarizes the results of three diverse research projects focusing on (i) local dielectric and electrostatic properties of water-silica nanoparticle interface (Chapter 1 and 2) and (ii) thermal effect on unfolding and oligomerization in membrane proteins on an example of *Anabaena* sensory rhodopsin (ASR).

In Chapter 1, interfacial electrostatic properties of monodisperse silica nanoparticles (SiNPs) in aqueous suspensions as a function of bulk *p*H were characterized by spin labeling EPR of two ionizable nitroxides: (1) IMTSL (*S*-(1-oxyl-2,2,3,5,5-pentamethylimidazolidin-4-yl)methyl methanesulfo-nothioate) and (2) IKMTSL (*S*-4-(4-(dimethylamino)-2-ethyl-5,5-dimethyl-1-oxyl-2,5-dihydro-1*H*-imidazol-2-yl). SiNPs of *ca*. 116 nm in average diameter (by particle number) were synthesized using the Stöber method and their surface was modified by silanization under harsh conditions to ensure robust attachment of the thiol-terminated ligands to the silica surface. These ligands were consequently modified with either IMTSL or IKMTSL to characterize the surface electrostatic potential of the nanoparticles from their EPR spectra. EPR titration data for these two *p*H-sensitive nitroxides allowed for differentiating the dielectric and electrostatic contributions to the interfacial properties of SiNPs. Surface electrostatic potential calculated from EPR titration of IKMTSL demonstrated an approximately linear increase in the magnitude starting at about zero at *p*H≈4.0 and reaching ≈-150 mV at *p*H≈8.5. This is in agreement with the existing literature on the surface potential associated with the silanol deprotonation developing over a wide *p*H range.

In Chapter 2, effects of ionic strength on local properties of water-silica interface were investigated. Monodispersed silica nanoparticles with average diameter of 108 nm were synthesized and surface-modified with thiol-terminated silane ligands, which were then covalently labeled with EPR-active electrostatic molecular probes via thiol-specific chemistry. Two pH-sensitive EPR probes with pKa=3.33 (IMTSL) and 5.92 (IKMTSL) were employed in order to separate pH regions where acidic ($pK_a \approx 4.5$) and basic ($pK_a \approx 8.5$) silanols undergo reversible protonation. To determent the effect of ionic strength, DI water solutions with a range of NaCl concentrations were used ([NaCl] = 0.05 M ÷ 2.0 M). Dependences of the surface potential of silica nanoparticles as a function of both bulk pH and the ionic strength were established. These data show that the electrostatic surface potential of silica nanoparticles in aqueous suspensions could be adjusted from ca. -200 mV to 0 mV by simply changing pH and/or salt concentration.

Chapter 3 describes the results of study of local unfolding kinetics and thermal effect on oligomerization in a membrane protein *Anabaena* sensory rhodopsin (ASR). Two Cys mutants of ASR, N148C and S26C, were labeled with a nitroxide S-(1-oxyl-2,2,5,5-tetramethyl-2,5-dihydro-1H-pyrrol-3-yl)methyl methanesulfonothioate (MTSL) and reconstituted into DMPC-DMPA lipid vesicles. Unfolding kinetics of ASR was investigated using X-band (9.5 GHz) CW EPR. While the thermal unfolding as monitored from local side-chain dynamics at two sites was found to be fully reversible, the temperature ranges of these events were found to be strikingly different. Specifically, the thermal unfolding of the loops containing residues N148 and S26 demonstrated denaturation midpoints (T_m) equal 62.0 ± 0.4 °C and 87.3 ± 0.4 °C, respectively. Thermal unfolding enthalpy (ΔH) and entropy (ΔS) for both mutants were estimated. Double electron-electron resonance (DEER) measurements of freeze-trapped S26C mutant showed that, upon thermal exposure, ASR retains its trimeric structure; however, some monomers seem to migrate from its

initial trimer to a neighboring one, thus effectively exchanging positions between the trimers. The rates and energetic cost of such transition were estimated (E_0 = 76.60 ± 8.19 kcal mol^{-1} K^{-1}). Although some experimental evidence supports the proposed monomer exchange mechanism, additional experiments are required to fully confirm it.

Local Properties of Bio- and Nanointerfaces by Spin Labeling EPR

by
Vladislav Romanovich Perelygin

A dissertation submitted to the Graduate Faculty of
North Carolina State University
in partial fulfillment of the
requirements for the degree of
Doctor of Philosophy

Chemistry

Raleigh, North Carolina
2021

APPROVED BY:

_____	_____
Dr. Alex I. Smirnov Committee Chair	Dr. Alexander Nevzorov
_____	_____
Dr. Erin Baker	Dr. Reza Ghiladi

_____
Dr. Joseph Tracy

DEDICATION

To my wonderful family, whose unconditional love has supported and encouraged me to achieve new goals.

BIOGRAPHY

Vladislav was born in 1994 in a loving family of two Chemical Engineers, Svetlana and Roman. He was raised in an atmosphere where genuine curiosity was always encouraged. When he went to the first grade, his parents gave him two popular science books "*Mechanics for entertainment*" and "*Physics Everywhere*", which formed a foundation of his passion for natural sciences.

In 2012 Vladislav was accepted to a prestigious Russian university, Moscow State University, in Physics Department. That was the time when he found his interest in Physical Chemistry, as he joined the Nanosensorics group under the guidance of Professor Elizaveta Konstantinova, where he was introduced to Magnetic Resonance research field for the first time. As a result of his two years' work as an undergraduate researcher, Vladislav defended his undergraduate thesis "Structure and properties of spin centers in solid solutions based on zinc and cadmium sulfate".

In 2016 Vladislav was accepted to North Carolina State University, where he joined Professor Alex. I. Smirnov's group. The atmosphere of constant support and encouragement for independent thinking allowed him to try his hand in various research projects ranging from studies of protein folding to interfacial properties of colloidal systems.

ACKNOWLEDGMENTS

There are a lot of incredible people who supported me through the time I have been engaged in research, and to whom I am very grateful. However, there are a few to whom I would like to express my special gratitude.

First of all, I am grateful to Prof. Alex I. Smirnov for constant care and support both inside and outside of the lab settings;

Prof. Tatyana I. Smirnova, for inspiration and invaluable suggestions;

Prof. Maxim Voynov, for uncountable hours spent on educating me about various chemistry aspects, help with designing experiments and many discussions;

Dr. Sergey Milikisiyants, for numerous advices about Magnetic Resonance theory and practice;

Dr. Antonin Marek, for countless help with experiments;

Prof. Alexander Nevzorov, Prof. Reza Ghiladi, Prof. Joseph Tracy and Prof. Erin Baker, for agreeing to be a part of Advisory Committee;

Prof. Elizaveta Konstantinova, for guidance during my first steps in the field.

Finally, to all members of Prof. Smirnov, Prof. Smirnova and Prof. Nevzorov groups for being supportive and creating a sense of community.

TABLE OF CONTENTS

LIST OF TABLES

LIST OF FIGURES

LIST OF ABBREVIATIONS

NP	Nanoparticle
SiNP	Silica nanoparticle
DFT	Density functional theory
MD	Molecular dynamics
EDL	Electrical double layer
SFG	Sum frequency generation
SHG	Second harmonic generation
XPS	X-ray photoelectron spectroscopy
NMR	Nuclear magnetic resonance
ssNMR	Solid-state NMR
cryo-EM	Cryogenic electron microscopy
AFM	Atomic force microscopy
EPR	Electron paramagnetic resonance
DEER	Double Electron-Electron Resonance
TEOS	Tetraethyl orthosilicate
MMTS	*S*-methyl methanethiosulfonate
MPTMS	3-mercaptopropyl trimethoxysilane
TEA	Trimethylamine
TGA	Thermogravimetric analysis
SEM	Scanning electron microscopy
FESEM	Field emission scanning electron microscopy

Tris	Tris(hydroxymethyl)aminomethane
SSA	Surface specific area
BET	Brunauer–Emmett–Teller;
MTSL	*S*-(1-oxyl-2,2,5,5-tetramethyl-2,5-dihydro-1*H*-pyrrol-3-yl)methyl sulfonothioate;
IMTSL	*S*-(1-oxyl-2,2,3,5,5-pentamethylimidazolidin-4-yl)methyl methanesulfonothioate;
IKMTSL	*S*-4-(4-(dimethylamino)-2-ethyl-5,5-dimethyl-1-oxyl-2,5-dihydro-1*H*-imidazol-2-yl;
IMTSL-ME	IMTSL-2-mercaptoethanol.
IKMTSL-	IKMTSL-2-mercaptoethanol.

PR	Bacteriorhodopsins
TR	Thermophilic rhodopsin
ASR	*Anabaena* sensory rhodopsin
SDSL	Site-directed spin labeling
SEC	Size-Exclusion Chromatography
CD	Circular dichroism spectroscopy
DDM	n-dodecyl-ß-D-maltoside
DMPC	1,2-dimyristoyl-sn-glycero-3-phosphocholine
DMPA	DMPA 1,2-Dimyristoyl-sn-glycero-3-phosphate, sodium salt
FESEM	Field Emission Scanning Electron Microscope
NCSU	North Carolina State University

HMI	2,2,3,4,5,5-hexamethylimidazolidin-1-oxyl nitroxide

CHAPTER 1

Dielectric and Electrostatic Properties of the Silica Nanoparticle - Water Interface by EPR of pH-Sensitive Spin Probes

Vladislav Perelygin, Maxim A. Voinov, Antonin Marek, Erkang Ou, Jacqueline Krim, Donald Brenner, Tatyana I. Smirnova, and Alex I. Smirnov

An adapted version of this chapter is published in The Journal of Physical Chemistry C **2019**, 123, 49, 29972–29985

1.1 Introduction

1.1.1 *Silica nanoparticles: applications and properties*

Among many inorganic nanopartcles (NPs) available today, silica nanoparticles (SiNPs) and silica-coated NPs represent, perhaps, some of the most versatile nanomaterials for applications across chemical, materials science, and biomedical fields. Specific examples include the use of SiNPs in heterogeneous catalysis[1] and as building blocks of nanocomposite materials,[2] pseudostationary phase for capillary electrophoresis separation,[3] nanocarriers for drug delivery[4,5] and biosensing,[6] biomedical imaging agents,[7] and active components of nanoformulations to reduce friction.[8] The main reasons for such a widespread use of silica-based nanomaterials are the readily available fabrication methods and, even more importantly, favorable structural and chemical properties of the silica surface. Indeed, many applications dictate precise control over particle size, shape, pore size, and pore geometry and all these features could be attained by synthesizing specific SiNPs. Because of an exceptionally large surface area possessed by mesoporous silica such a material is suitable for nonspecific absorption of various molecules. Furthermore, hydroxyl groups of silica surface could be readily modified by various silane-based

coupling agents,[9] thus, opening an additional avenue for attaching different molecules to NPs. Silica is also chemically stable over a wide range of conditions and was shown to be biologically compatible.[10] For these reasons it was found to be very effective for encapsulating catalytic inorganic core,[1] enzymes,[11] and various drugs[12] including oligonucleotides for gene delivery.[13]

Having NP surface covered with silica and/or modifying silica surface with various functional groups has been shown to reduce particle aggregation and nonspecific binding.[14] Generally, untreated silica nanoparticles are highly negatively charged[15] at neutral and alkaline *p*H and the resulting repulsive electrostatic forces provide for an extended stability of such colloids. Surface electrostatic potential also plays a crucial role in NP interactions with other molecules and cellular components that could lead to the formation of protein coronas and determine intracellular uptake and biocatalytic activity.[16] Thus, understanding and probing these charge-based interactions at the bio-nano interface is important from the perspective of developing new nanomaterials and their safe use.[17] The same surface electrostatic properties are also essential for developing new nanoparticle-based lubricating technologies.[8,18]

Ionization state of the surface hydroxyl groups, also known as silanols, has been investigated in detail by both experimentally and theoretically. Thus, detailed studies showed that surface silanols could be divided into two types with different properties[19,20]. First type is known as out-of-plane silanols with acidic pK_a in the range from 4.5[19] to 5.6[21] pH units. These silanols are capable of forming strong hydrogen bonds with the surface water molecules. The second type, in-plane silanols, demonstrates an alkaline behavior with pK_a of 8.5 that results in a weak silanol-water bonding[21]. In some studies, particularly in computer simulations, silanols are separated even into four distinguished groups: isolate, H-bonded, vicinal and geminal, with pK_a values ranging from pK_a=2.9 for vicinal silanols, and up to pK_a=10.3 for isolated[22] ones.

1.1.2 *Methods to study water-silica nanoparticle interface*

Electrostatic properties in colloidal systems are greatly dependent on the properties of a dispersion medium. Typically, a colloidal particle is surrounded by multiple layers of counter ions. Their affinity and layer thickness depend on the type of ions and the solution ionic strength. The ion distribution can be described using an electrical double layer (EDL) model.[23] This model takes into account the type and degree of ion affinity to a charged surface and distinguish ions associated with colloidal particle into two layers (Figure 1.1). The layer that is tightly bound to the particle surface is called the Stern layer. These counter ions are considered to be inseparable from the surface. In the Stern layer, the ion attraction is governed by a strong Coulomb force. The second part of EDL is called the diffuse or the Gouy – Chapman. This layer is known to effectively screen charge of a particle. It consists of ions that are loosely attached with the particle surface. However, the border of the diffuse layer and, accordingly, EDL can only be roughly estimated. Moreover, division into the Stern and the diffuse layer is also somewhat arbitrary.

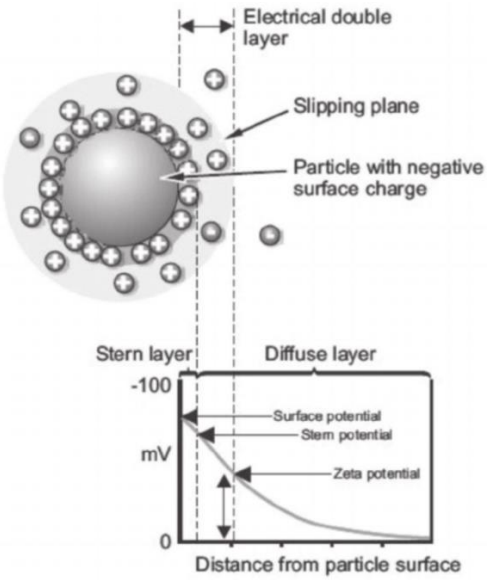

Figure 1.1. A cartoon representation of electrical double layer (EDL) composition of a negatively charged colloidal particle. Adapted from literature.[24]

The significance of electrostatic phenomena near silica surfaces stimulated several seminal theoretical studies which employed density functional theory (DFT)[25,26] and molecular dynamics (MD)[27–29] simulations. Although computational methods provide a valuable insight into interactions on the molecular scale, they have several limitations. Firstly, in a typical simulation, silica is treated as planar quartz structure with several tens of atomic layers; water and ionic species are presented by a small number of molecules. Such an approach focuses only on specific local interactions, and this information is often hard to extrapolate on a large scale, such as SiNP in a solution. Secondly, such computations usually struggle to simulate a dynamic process at any significant time scale. We note here that DFT provides a static representation of the system based on the energy minimum condition. MD simulations are severely limited by the complexity of the calculation. This leads to the fact that any simulation relies on numerous assumptions and requires a simplified model. While some of the silica studies were focused on water molecule interactions with silica surface,[25,26] other papers focused on the bimodal behavior of silanol groups and the estimation of the magnitudes of their dissociation constants (pK_a).[21,30] Water molecules distribution and orientation at silica surface as a function of type of salt and its concentration has also been studied using theoretical approach.[31] Simulation of pH and salt dependent biomolecule adsorption on silica surfaces represents an example of a complicated computational design.[29] However, the result was achieved at the cost of reduction of the number of interacting ions, thus, revealing the interaction pattern on an extremely small scale in a highly diluted system.

Electrostatic interactions can be treated explicitly (e.g., in MD simulations) or treated using a continuum electrostatic approach.[32–34] In this model the surface potential develops as the silanol groups on the silica surface become deprotonated, which leads to increment in the surface potential. For a colloidal particle surface potential is described by the Poisson–Boltzmann (PB)

equation. Analytical solution for PB equation is usually obtained with some assumptions about the nanoparticle geometry.[35] Most commonly a nanoparticle is assumed to be either much larger or much smaller than a characteristic thickness of ionic layer, which is also referred as the Debye screening length (k^{-1}). Thus, when the Debye screening length is much smaller than a particle size the surface is considered to be planar, which simplifies solution of PB equation. If the Debye length is much larger than particle size, the NP is considered to be infinitely small, allowing to use "point-charge" approximation. The first case is applicable to particles of hundreds of nanometers in diameter at low ionic strength, where Debye length is short. The second approximation is for very small nanoparticles of a few nanometers or in solutions with high salt concentration.[36] Although solving the Poisson–Boltzmann equation provides a good estimate for the surface potential, it is based on many assumptions and requirements for a colloidal system, such as cooperative silanol protonation/deprotonation, presence of thermal equilibrium between particle surface and ionic species, aqueous solution with no buffer, the fact that only strong electrolytes are suitable and a solution is limited to several ionic species at a time.[37] All these assumptions limit the number of problems where this method can be applied.

However, that while theoretical models of silica-water interface continue to evolve, the number of experimental studies, especially at the atomic scale level that is of interest to physical chemistry, remains to be limited. The likely reason for this is that only very few experimental methods are suitable for such studies and the data provided by some of the methods are rather limited to specific sample configurations and/or experimental conditions and in many cases interpretation of the experimental results is based on specific assumptions.

As an example, let us consider characterization of NP electrostatic properties in suspensions by measurements of their electrophoretic mobility. While the method is suitable for a

wide range of NPs and does not require relatively high concentrations of NPs or chemical functionalization of their surfaces,[38,39] it reports on an electrokinetic potential, or ζ-potential, which calculations are model-based.[23] The ζ-potential is an electrostatic potential at the slipping plane of the NP double layer that in turn can be related to the total charge contained behind the slipping plane (Figure 1.2). However, such calculations rely on a number of assumptions that are not always valid. ζ-potential results are highly dependent on the measurement set up, such as a choice of calculation model, experiment temperature and dilution factor. Although measurements of ζ-potential are rather simple, the measured potential corresponds to a slipping plane with an ill-defined location and, therefore, such data are difficult to convert to the surface charge density without making additional assumptions. Moreover, defining of the slipping plane is further complicated for the surfaces decorated with any type of ligand, making the method hardly applicable in such cases. Therefore, ζ-potential experiments are recommended to be used either for multi-point experiments with variation of system parameter, such as pH and salt concertation, or as a complimentary method.[40]

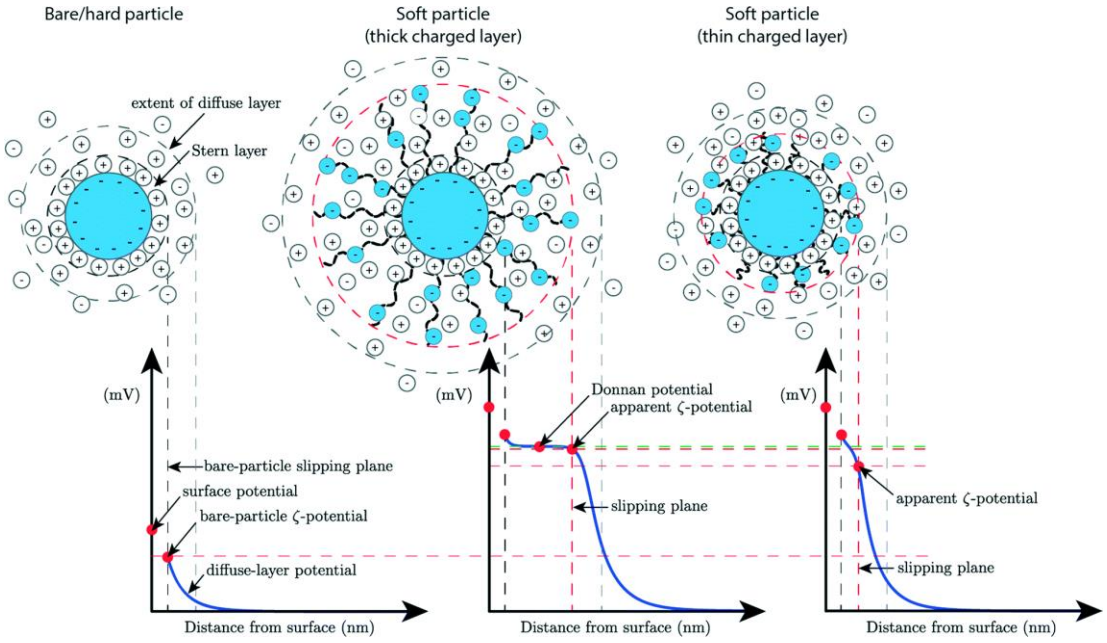

Figure 1.2. Electrical double layer (EDL) of hard (bare) and soft (decorated with ligands) nanoparticles. Slipping plane is ill-defined feature that depends on many factors. The complexity of its estimation increases dramatically if surface is decorated with any type of ligand. Adapted from.[40]

Another common method to measure static surface charge is a potentiometric titration.[41] While simple and readily available, the method requires independent measurements of NP surface area and again is making several assumptions regarding the model of surface charging. Electrostatic potential of interfaces has also been probed using sum frequency generation (SFG) and second harmonic generation (SHG)[42–44] as well as x-ray photoelectron spectroscopy (XPS) [45].

Each of such methods also has some advantages but also known limitations. Atomic structure of the surface silanol groups can be specifically probed by ^{29}Si NMR[46,47] owing to the high response of ^{29}Si chemical shift to the local environment. However, the main disadvantage of ^{29}Si NMR is low ^{29}Si isotope abundance and sensitivity of the method, which necessitates the use of extremely large surface areas in order to distinguish the surface and the internal silicon. We

note that for some of SiNP systems the NMR sensitivity issue could be resolved by applying rapidly advancing DNP methods.[48]

Finally, silicon oxide-based electrodes and pH sensors were used to empirically determine the potential of a planar silica surface. The methods included electrolyte-on-insulator (EOS), impedance and ion-sensitive field-effect transistor (ISFET). The results of these studies were summarized by Lowe *et al*[49] (Figure 1.3).

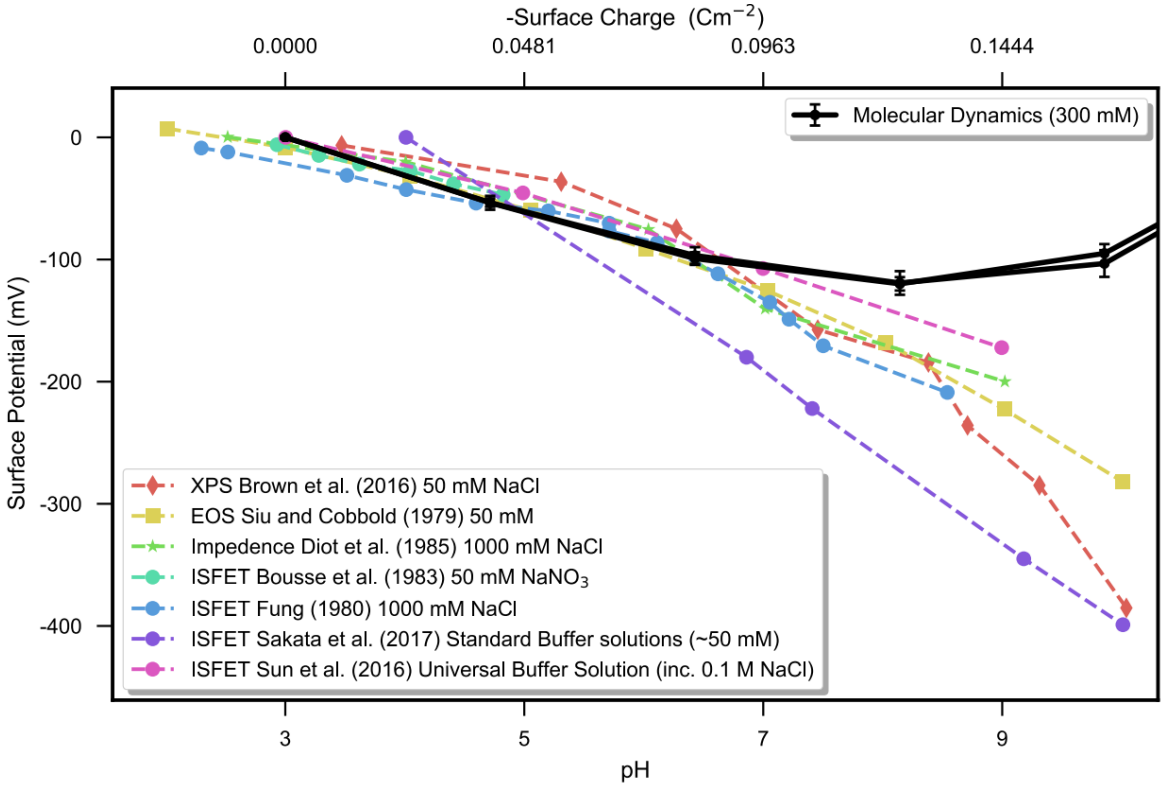

Figure 1.3. Summary of a number of studies reported previously. The methods included electrolyte-on-insulator (EOS), impedance, ion-sensitive field-effect transistor (ISFET), XPS and MD simulations. The major focus of the reports was on the surface charge of silicon oxide films deposited at the flat surface due to particular importance of such system to electronics and the specifics of applied techniques. Adapted from literature.[49]

Spin labeling Electron paramagnetic resonance (EPR), on the other hand, has sufficient sensitivity to study nanoparticle-liquid interface even at low concentrations.[50–53] The method is also fully applicable to opaque materials and solutions for which the optical methods are expected to fail. When extended to *p*H-sensitive nitroxides, the method is suitable for probing local electric field potentials at interfaces[54–57] and effective proton activities in the nanopores.[58,59] In application to NPs, the authors aware of only one report of probing surface electrostatic properties of carboxylate-terminated tiopronin-protected 1.8 nm Au NPs using a series of variable length disulfide ligands labeled with a *p*H-sensitive imidazoline nitroxide.[53] In this study, the nitroxide was attached to the NPs surface through ligand-exchange reaction.

1.1.3 *Spin labeling Electron paramagnetic resonance (EPR)*

Electron paramagnetic resonance is a method that allows one to measure paramagnetic systems such as molecules with unpaired electron, anionic compounds, dangling bonds in crystalline structures, some coordination complexes, and others. It is based on the phenomena of the Zeeman splitting. When a paramagnetic sample is placed in an external magnetic field its S=1/2 spins rearrange to have their projection of angular and associated magnetic moment either parallel ($m_s = -\frac{1}{2}$) or antiparallel ($m_s = \frac{1}{2}$) to the field, corresponding to higher and lower energy states, respectively (Figure 1.4 A). For spins in thermal equilibrium these levels are populated based on the Boltzmann distribution, and the energy difference between them is proportional to external magnetic field (B_0), constant called Bohr magneton (μ_β) and a constant specific for a particular paramagnetic center, called g-factor (g_e). Thus, by applying electromagnetic irradiation of an appropriate energy ($\Delta E = h\nu$), a transition from a lower, more populated level to a higher energy level can be induced. This will occur when the resonance condition is satisfied:

$$h\nu = g_e \mu_\beta B_0 \quad (1.1)$$

The most common way of EPR measurements is when the irradiation wave is kept at constant frequency, corresponding to a certain wave band (the most common ones are X-band: 9.5 GHz, Q-band: 34 GHz, W-band: 95 GHz), while external magnetic field gradually changes, making a "field sweep". When the resonance condition is met, paramagnetic sample absorbs the irradiation, indicating a peak on EPR spectrum (Figure 1.4 B). First derivative of the absorption spectrum is taken due to the fact that modulation and in-phase detection are used.

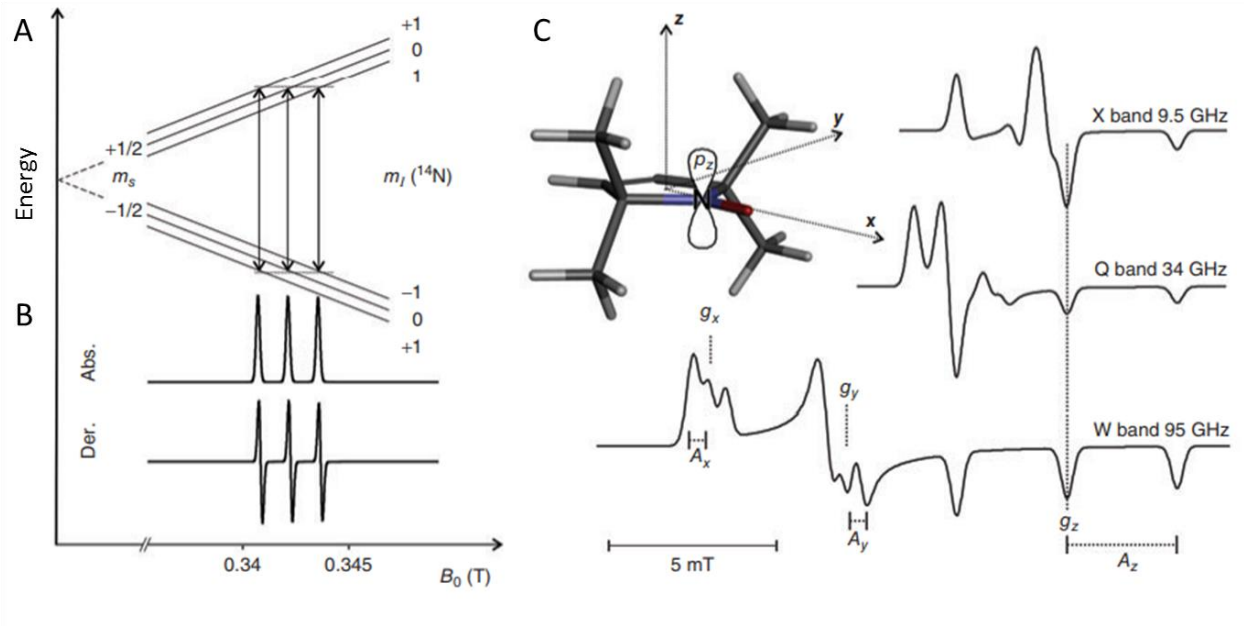

Figure 1.4 EPR spectroscopy of nitroxide radical. (A) Represents energy level splitting in external magnetic field with corresponding spin projections. (B) Typical nitroxide absorption spectrum and its first derivative. (C) Principal axis system in a nitroxide spin probe and spectra demonstrating hyperfine splitting at different microwave bands. Adapted from literature.[60]

However, in many systems, including nitroxide radicals that were used in current research, nucleus surrounding paramagnetic center may also contribute to the observed spectra. Specifically,

nuclear spins interact with both external magnetic field and the electronic spins. Therefore, each electronic spin energy level is split into a number of sublevels depending on the nucleus spin. This effect is called hyperfine interaction and it is defined by hyperfine splitting constant (*A*). When nuclear Zeeman term can be neglected and the electronic Zeeman tern is much larger than the hyperfine interaction, the overall Spin Hamiltonian for such a system is given by:

$$\hat{H} = g_e \mu_\beta B_0 \hat{S}_z + hA\hat{S}_z\hat{I}_z \quad (1.2)$$

In general, *g*-factor and hyperfine splitting constant are anisotropic parameters. Due to the fact that unpaired electron is usually unequally distributed in a molecule of interest, its *g*-factor and hyperfine splitting constant will depend on the molecule orientation relative to the external magnetic field.

To better understand this phenomenon, let us consider a nitroxide radical (Figure 1.4 C). It is convenient to choose a system of coordinate, also known as principal axis system, in a way that it reflects the structure of a molecule. Typically, principal axis system for a nitroxide probe is chosen so that the x-axis is directed along the NO bond and the z-axis being parallel to the p_z orbital of the nitrogen. The nitroxide radical has an unpaired electron, located on the NO bond. Since the electron is unequally distributed along the axis, it will result in a different spectra shapes corresponding to different relative orientation of the nitroxide axis and the external magnetic field. As *g*-factor and hyperfine splitting constant report on local environment of a paramagnetic center, obtaining its anisotropic values provides unique information about the system of interest.

While due to the anisotropy each molecule produces a different spectrum shape depending on its relative orientation, if we consider a system where the molecules are randomly oriented at any given moment, we notice that the anisotropy averages, producing a spectrum with isotropic g-factor (g_{iso}) and hyperfine splitting (A_{iso}) (Figure 1.5). A typical example is a free radical in a

solution. The radicals remain in constant motion and rotation, so they do not indicate any preferred orientation, thus producing an isotropic spectrum.

In EPR, a molecule motion is characterized by rotational correlation time (τ_c), which is an average time required for paramagnetic molecule to rotate through an angle of one radian. If τ_c is close to characteristic timescale of EPR measurement (0.1 to 100 ns), then anisotropy is not fully averaged, thus revealing "slow motion" spectra (Figure 1.5 D and C). "Fast motion" regime corresponds to isotropic hyperfine interaction (A_{iso}).

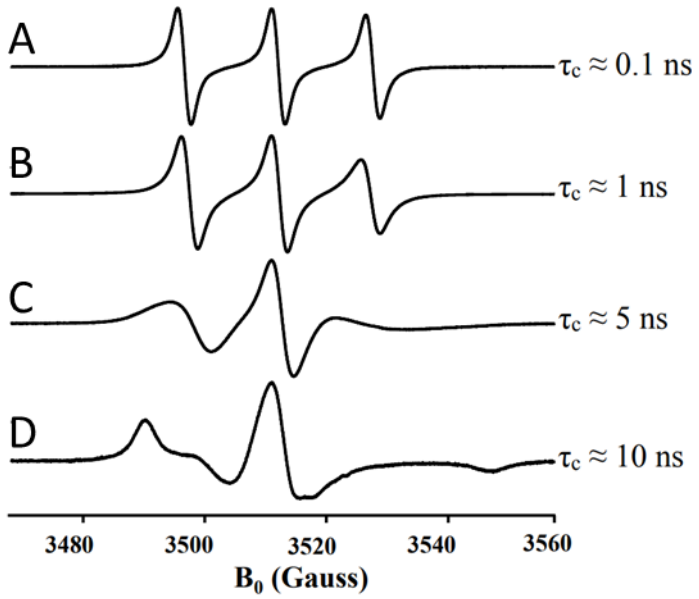

Figure 1.5. EPR spectral lineshape dependent on rotational correlation time (τ_c): (A) Fast motion regime; IMTSL in dilute solution. (B) IMTSL attached to a small peptide in solution. (C) A spin labeled peptide integrated into a phospholipid vesicle. (D) Slow motion regime; The spin label within a vesicle is protonated and experiences an electrostatic attraction to the bilayer interface. Adapted from.[61]

pH - sensitive nitroxide probes can be used to detect local electrostatic properties. Reversible protonation causes redistribution of unpaired electron density and, therefore, changing

its paramagnetic properties, which can be detected by EPR (Figure 1.6). EPR spectra of these nitroxides directly report on their ionization state and local electrostatic potential (Ψ) through changes in nitroxide magnetic parameters and the degree of motional averaging.

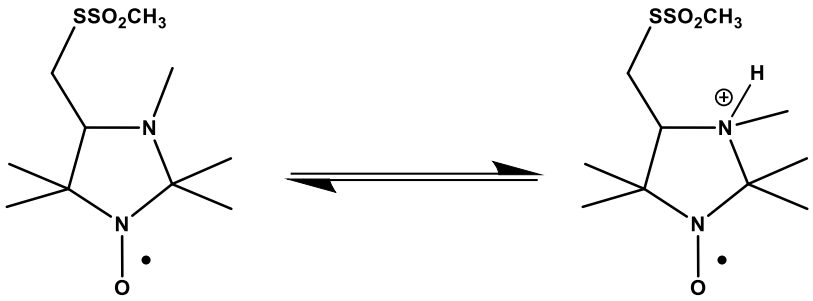

Figure 1.6. Reversible protonation of IMTSL, pH – sensitive nitroxide radical.

Its spectrum at given pH can be decomposed to protonated and deprotonated forms. Finding correlation between fraction of deprotonated nitroxides and pH allows to plot titration curve and find observed dissociation constant (pK_a^{Obs}) for the probe in its local environment. If pH - sensitive probe is covalently attached to a molecule, titration curve will report on molecules local electrostatics by comparing pK_a^{Obs} and probes intrinsic pK_a^w in the same solution.

1.1.4 *Spin labeling EPR to study water-silica nanoparticle interface*

Here for the first time, we report on a spin labeling EPR study of local dielectric and electrostatic properties of the SiNP-water interface by covalently attaching two *p*H-sensitive nitroxides with different *p*K$_a$'s to the silica surface through a short linker. Such covalent attachment ensures that the spectroscopic EPR readout originates from a location at the SiNP-water interface defined by the molecular linker. The nitroxides were attached to monodispersed SiNPs of *ca*. 116 nm in diameter that were decorated with silane ligands terminated by thiol groups. Two *p*H-sensitive nitroxides with significantly different *p*K$_a$ values, *i.e.*, *p*K$_a$≈3.0 and 6.0, were

employed to provide a broader *p*H range for characterization of the surface electrostatic potential. The EPR titration data for these two probes allowed for differentiating the dielectric and electrostatic contributions to the interfacial properties of SiNPs.

1.2 Experimental Section

1.2.1. *Materials and EPR Spin Labels*

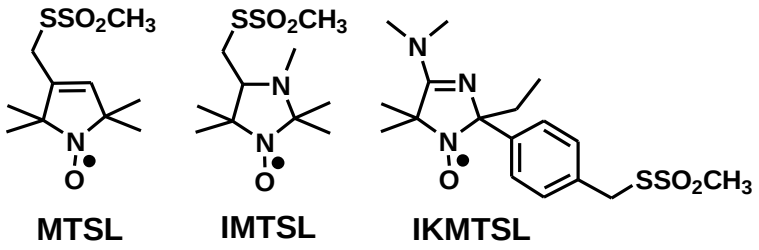

Figure 1.7 Chemical structures of thiol-specific spin labels used in this chapter: MTSL (*S*-(1-oxyl-2,2,5,5-tetramethyl-2,5-dihydro-1*H*-pyrrol-3-yl)methyl methanesulfonothioate), which exhibits EPR spectra insensitive to *p*H changes, and *p*H-sensitive IMTSL (*S*-(1-oxyl-2,2,3,5,5-pentamethylimidazolidin-4-yl)methyl methanesulfonothioate) and IKMTSL (*S*-4-(4-(dimethylamino)-2-ethyl-5,5-dimethyl-1-oxyl-2,5-dihydro-1*H*-imidazol-2-yl).

Tetraethyl orthosilicate (TEOS) and *S*-methyl methanethiosulfonate (MMTS) were purchased from Sigma-Aldrich Corp. (St. Louis, MO). 3-Mercaptopropyl trimethoxysilane (MPTMS) was purchased from Alfa Aesar (Haverhill, MA). All other chemicals and solvents were purchased from VWR International (Radnor, PA) or Sigma-Aldrich, unless otherwise indicated, and used without additional purification. All solvents were reagent grade. Thiol-specific spin label MTSL (*S*-(1-oxyl-2,2,5,5-tetramethyl-2,5-dihydro-1*H*-pyrrol-3-yl)methyl methanesulfonothioate), which exhibits EPR spectra insensitive to *p*H changes, was synthesized by modifying the original procedure.[62] *p*H-sensitive spin label *S*-(1-oxyl-2,2,3,5,5-

pentamethylimidazolidin-4-ylmethyl) ester (IMTSL) was synthesized according to the published procedure.[54] Another *p*H-sensitive spin label *S*-4-(4-(dimethylamino)-2-ethyl-5,5-dimethyl-1-oxyl-2,5-dihydro-1*H*-imidazol-2-yl)benzyl methane-thiosulfonate (IKMTSL) was synthesized using the procedures described previously.[63] Chemical structures of the spin labels are shown in Figure 1.7 while pK_a of aqueous solutions of these nitroxides and their 2-mercaptoethanol (2-ME) adducts are given in the Table 1.1.

Table 1.1. Experimental pK_a of nitroxides IMTSL and IKMTSL and their adducts in aqueous solutions, polarity shifts ΔpK_a^{pol}, and calculated effective local dielectric constant ε_{eff}. All data were obtained at 21 °C except when noted.

Nitroxide	pK_a^w	pK_a^w of 2-ME adduct	pK_a^{obs} of SiNP adduct	ΔpK_a^{pol}	ε_{ef}
IMTSL	1.58±0.03[a]	3.33±0.03[a]	2.92±0.04	-0.41±0.05	70.8±5.0
IKMTSL	5.68±0.01[b]	5.98±0.01[b]	n/a/, broad range of pK_a	≈-0.95	57±4

[a]Measured at 19 °C.[57] [b]Data were reported previously.[63]

1.2.2. *Synthesis of Silica Nanoparticles*

Silica nanoparticles were synthesized using the Stöber method[64] by ammonia-catalyzed hydrolysis of tetraethoxysilane (TEOS). Precise control of ammonia concentration was achieved by saturating ethanol with NH_3 and using such saturated solution as a stock. In a typical procedure, an ethanol solution containing TEOS (0.169 M), H_2O (2.58 M) and NH_3 (0.960 M) was stirred at 60 °C overnight. This ratio of reagents yields nanoparticles with a diameter of d=116±27 nm (average by NP number as determined from dynamic light scattering). The silica nanoparticles

formed were kept in ethanol solution as is before the consequent surface modification, which was typically carried out within a few days of synthesis. No changes in the particle average diameter were observed upon 2 months of storage.

1.2.3. *Nanoparticle Silanization*

SiNP surface was modified with 3-mercaptopropyl silyl ligands using (3-mercaptopropyl) trimethoxysilane (MPTMS) (Figure 1.8). Ethanol solution of silica nanoparticles was centrifuged for 15 min at 5,000 rpm (Microfuge 18 Centrifuge with F241.5P rotor, Beckman Coulter, Brea, CA), the supernatant ethanol was carefully removed with a pipette, and acetonitrile solution of triethylamine (TEA, 10 mM) was added. The mixture was carefully vortexed, centrifuged, the supernatant solvents were removed with a pipette, and the solvent exchange was repeated three times. MPTMS (345 µl of 3 mM solution in acetonitrile) was added to an acetonitrile solution of SiNPs (approximately 1 wt%) and the mixture was stirred for 48 h at 60 ^{o}C under nitrogen. To remove the unreacted silane, nanoparticles were spun down in the centrifuge, the supernatant solvents were removed with a pipette, and a fresh portion of acetonitrile solution of TEA (10 mM) was added. The washing procedure was repeated three times. Further TGA analysis showed that the ligand coverage was 0.36-0.43 silane ligand per nm^2.

1.2.4. *Labeling of Silanized Nanoparticles with Paramagnetic Nitroxide and Diamagnetic Tags*

SiNPs surface-modified with the ligands terminated by thiol (-SH) groups were spin labeled through methanethiosulfonate chemistry (see. Figure 1.8). The labeling procedure was identical for each of the two nitroxides. In a typical procedure a double molar excess of the nitroxide label relative to MPTMS was added to the nanoparticle suspension in an acetonitrile solution of TEA (10 mM) and the reaction mixture was stirred at room temperature for 48 hr. The

unreacted spin labels were removed by spinning down the nanoparticles in the centrifuge, removing the supernatant solvents with a pipette, and then adding a fresh portion of the acetonitrile solution of TEA (10 mM) and re-suspending NPs by vortexing. The washing procedure was repeated three times. The EPR spectra from the acetonitrile supernatant demonstrated a progressive decrease in the intensity of three-line signal characteristic for freely tumbling small nitroxide till essentially no signal was observed after the third wash (Figure 1A.1, Appendix A1).

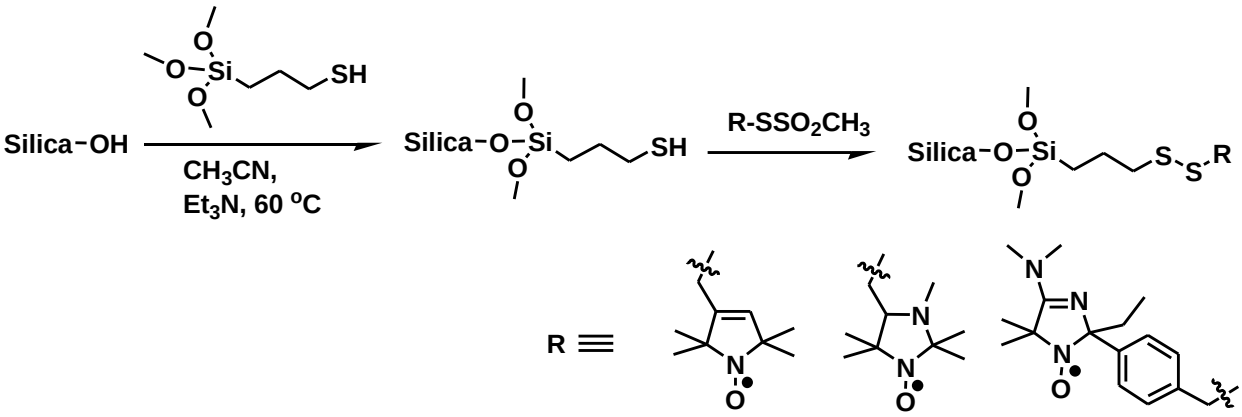

Figure 1.8. Modification of silica nanoparticle surface with (3-mercaptopropyl) trimethoxysilane (MPTMS) and a subsequent labeling with three different nitroxides.

Diamagnetic modification of silanized nanoparticles was carried out using *S*-methyl methanethiosulfonate (MMTS) as the labeling reagent. The labeling procedure was identical to the spin labeling protocol detailed above.

1.2.5. *Nanoparticle Characterization*

Aqueous suspensions of synthesized SiNPs (1.06 wt%) were initially characterized by dynamic light scattering (DLS, Zetasizer, Malvern, Westborough, MA). Morphology of SiNPs has

been further examined by Field Emission Scanning Electron Microscope (FESEM) FEI Verios 460L (FEI Company, Hillsboro, OR) installed and operated by an Analytical Instrumentation Facility (AIF, NCSU). A few microliters of 1.06 wt% aqueous suspension of SiNPs were air-dried on a carbon tape (Electron Microscopy Sciences, Inc., Hatfield, PA). The samples were imaged without any metal coatings. Figure 1.9 shows a typical SEM image of bare SiNPs nanoparticles demonstrating a spherical morphology and diameters which agree well with the DLS measurements.

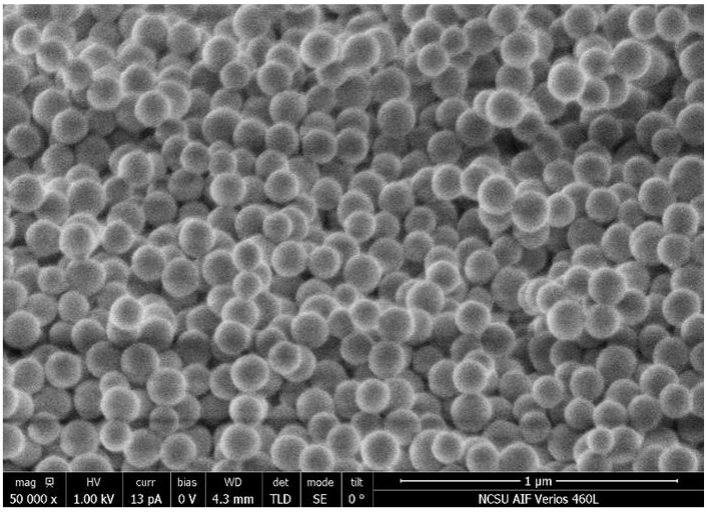

Figure 1.9. Typical FESEM image of bare silica nanoparticles air-dried from an aqueous suspension on a carbon tape. The scale of 1 µm in width is shown as a white bar at the bottom.

Thermogravimetric analysis (TGA Q50, TA Instruments, New Castle, DE) was employed to determine concentration of SiNPs in the stock suspension (1.06 wt%). For determination of the SiNPs' ligand coverage the following literature procedure[65] was employed. NPs were lyophilized overnight and then dried for 1h at 180 ^{o}C in vacuum to remove the physically adsorbed water. TGA was set to ramp temperature at 10 ^{o}C per min up to 120 ^{o}C, followed by 10 min isothermal section, and then to ramp at 20 ^{o}C per min up to 800 ^{o}C. Three types of SiNPs were tested: (1) bare

SiNPs, (2) SiNPs modified with silane, and (3) modified with silane and then labeled with IKMTSL. A relative weight loss of 4.1 – 4.3 % at the region of physically adsorbed water (*i.e.*, upon sample heating to 200 ^{o}C) was observed for all the samples. For bare SiNPs an additional 5.5% weight loss corresponding to silanol removal has been detected from 200 to 650 ^{o}C. The overall weight loss for this sample was 9.8%. For silanized SiNPs and SiNPs labeled with the nitroxide the total losses were 10.18 and 10.03 %, respectively. The higher losses for the last two samples compared to the bare SiNPs were attributed to the surface ligands. Some slight decrease (≈0.15%) in the weight loss for the spin labeled NPs was attributed to a detachment of *ca.* 1.4-1.5 % of the surface ligands after a few additional washes employed to remove the unreacted spin label.

1.2.6. *EPR Measurements*

X-band (9.5 GHz) continuous wave (CW) EPR spectra were recorded at room temperature (21 ^{o}C) with either a Varian (Palo Alto, CA) Century Series E-109 spectrometer interfaced to a PC or a Bruker Biospin (Billerica, MA) ELEXSYS E500 instrument. The Varian spectrometer was equipped with a standard rectangular TE_{102} resonator cavity while the Bruker spectrometer was outfitted with a Selected Super High Sensitivity Resonator with Optical Port. Aqueous suspensions of nanoparticles were drawn into a poly(tetrafluoroethylene) (PTFE) capillary (i.d. = 0.81 mm, o.d. = 1.12 mm, NewAge Industries, Inc., Southampton, PA), and the capillary was folded and inserted into a clear fused quartz EPR tube (i.d. = 3 mm, o.d. = 4 mm) open from both ends (VWR International). The quartz tube contained four passes of flexible PTFE tubing that would go through the entire sensitivity region of the resonator cavity to ensure approximately the same sample volume within EPR resonator even though this experimental arrangement was not used for quantitative spin counting. After an EPR measurement the aqueous sample was recovered

with >90% efficiency and a new PTFE tubing was used for the next sample. Typical Bruker spectrometer settings were as follows: modulation amplitude was set to a quarter or a half of the narrowest line peak-to-peak line width; time constant, 20.48 ms; conversion time 20.56 ms, scan width 120 G, sweep time 42.11 s, incident microwave power, 2 mW. Typically, between 10 and 50 individual scans were acquired. Similar settings were employed for the Varian spectrometer.

EPR experiments using the Bruker spectrometer were carried out at ambient temperature of ≈21 ^{o}C maintained in the spectrometer room. The temperature for the experiments with the Varian spectrometer was maintained at 21.0 ^{o}C using the variable temperature accessory described earlier.[66]

1.2.7. *EPR Titration Experiments*

Before titration experiments a set of Tris buffers with a desired *p*H value was prepared using deionized water. The initial buffer had Tris concentration of 50 mM and *p*H=7.0. Additional buffers were prepared by titrating the initial 50 mM Tris buffer with either concentrated solutions of HCl or NaOH. Such a procedure yielded the buffers with *p*H ranging from *ca*. 1.4 to 12.0. We note that the majority of the experiments with SiNPs was carried out from *p*H=3.0 to 11.0. Based on calculations provided in the Supplemental Information (Section 2.5), the ionic strength of the individual buffers varied from 51 mM to 46 mM (or ±5%) within the latter *p*H range, thus, allowing us to neglect effects of the ionic strength on both the nitroxide pK_a[67] and the screening of the surface potential at the location of the nitroxide.[68] A modest increase in the ionic strength to I≈60 mM at *p*H=2.0 (Figure 1B.1, Appendix 1B) also allowed for neglecting the ionic strength effects.

For EPR titrations spin labeled SiNPs in the acetonitrile solution were re-suspended in 50 mM Tris buffer at *p*H = 5.0. Effective removal of any residual free label and acetonitrile was achieved by repeating a buffer exchange procedure three times. The procedure involved spinning

down the nanoparticles in the centrifuge, carefully removing the supernatant buffer solution with a pipette, and then re-suspending the particles in a fresh *p*H=5.0 buffer. Finally, NP solution was re-suspended in 100 μL of the buffer at 15-fold higher NP concentration for EPR measurements.

*p*H was adjusted the same way by spinning down the nanoparticles, removing the supernatant, re-suspending the particles in a fresh buffer prepared at a desired *p*H value, and repeating the procedure three times. The final *p*H of the sample was measured with a *p*H meter (SympHony SB70P pH meter, VWR International) equipped with InLab Micro electrode (Mettler-Toledo, Columbus, OH). The electrode was three-point calibrated using *p*H reference standard buffers (VWR Chemicals BDH®) at *p*H= 1.68, 4.01, and 7.00. All these procedures were carried out at room temperature (21 ^{o}C).

1.2.8. *Least-squares Decomposition of Experimental EPR spectra into Two Components*

An EPR spectrum of a nitroxide spin probe changes when it acquires a charge because of changes in both the nitroxide magnetic and rotational diffusion parameters.[57] In an EPR titration experiments, we are primarily interested in a fraction of the non-protonated species, *f*, as a function of *p*H rather than in determining complete set of the nitroxide rotational motion and magnetic parameters from the experimental spectra. Then, assuming that a slow chemical exchange model is satisfied for the probe protonation, an experimental EPR spectrum at an intermediate *p*H, $I(B)$, is approximated by a superposition of the spectra from the neutral and the ionized species, $F_R(B)$ and $F_{RH+}(B)$, respectively:

$$I(B) = f \cdot F_R(B) + (1 - f) \cdot F_{RH+}(B) + c \cdot B + d \tag{1.3}$$

where B is the magnetic field variable, and the linear baseline term is given by $(c \cdot B + d)$. All the spectra $I(B)$, $F_R(B)$, and $F_{RH+}(B)$ in eq.(1.3) are normalized by the values of the double integrals.

To simplify the decomposition procedure of the experimental spectrum $I(B)$, the spectra $F_R(B)$ and $F_{RH^+}(B)$ are measured experimentally. Because $p\mathrm{K_a}$ of the nitroxide in specific conditions (*e.g.*, when attached to a nanoparticle) is corresponding to such spectra is not known a priori, the EPR spectra are usually measured at increments of 0.2-0.5 *p*H units and then compared. If no measurable changes are observed in the two consecutive spectra, then those must be outside the ionization range of the probe and could be taken as $F_R(B)$ (if measured above $p\mathrm{K_a}$) or $F_{RH^+}(B)$ (if measured above $p\mathrm{K_a}$). After such an assignment of $F_R(B)$, and $F_{RH^+}(B)$ the spectral decomposition of EPR spectra $I(B)$ measured at intermediate *p*H was carried out using convolution-based least-squares method and software described earlier.[57,69,70] During the Levenberg–Marquardt optimization magnetic field positions and microwave phases of $F_R(B)$ and $F_{RH^+}(B)$ components together with baseline parameters were optimized to derive the fraction f of the non-protonated component. An example of such decomposition is given in the Appendix 1C (Figure 1C.1).

1.2.9. *EPR Measurement of Labeling Efficiency*

Spin label concentration was determined by comparing double integrals of CW EPR spectra of aqueous suspensions of IKMTSL-labeled SiNPs and 33 μM aqueous solution of IKMTSL measured at room temperature (21 ^{o}C). Suspension or solution were drawn into 1.0 mm i.d. 50 μl glass capillary tube, sealed from both ends with Critoseal® (Leica Microsystems GmbH, Wetzlar, Germany), inserted into another capillary tube (i.d. = 2.0 mm, o.d. = 2.4 mm), and then into the standard (i.d. = 3.0 mm, o.d. = 4.0 mm) quartz X-band EPR tube sealed from one end (all from Wilmad-LabGlass, Vineland, NJ). In such a sample arrangement the capillary with the aqueous suspension of SiNPs would go through the entire sensitivity region of the resonator cavity to ensuring that each time the EPR signal is collected from the same volume (estimated as *ca*. 23.5

µl). From comparing double integrals of the experimental EPR spectra from sparsely labeled SiNPs and verifying the concentration of SiNPs by TGA, the labeled SiNPs were found to contain on average 0.12 EPR-active IKMTSL nitroxide per 1 nm^2 of silica surface. The observed nitroxide surface coverage corresponds to the labeling efficiency of ≈30 %.

1.2.10. *Zeta Potential Titrations*

Zeta potential measurements as a function of *p*H were performed using a Zetasizer Nano ZS (Malvern Panalytical Inc., Westborough, MA). Measurements were carried out at 21 ^oC after 120 s equilibration time and analyzed with manufacturer-provided software based on the Smoluchowski model. For the measurements SiNPs were re-suspended in 50 mM NaCl solution in ultrapure (autoclaved) water and the buffer was exchanged using the procedure described above. A coarse *p*H adjustment was achieved by adding dropwise 1 M HCl or NaOH solution while stirring the SiNP solution at 21 ^oC in a PolyScience circulator bath (model 9710, PolySciences Inc., Warrington, PA). The concentration of both solutions was decreased to 0.3 M for finer *p*H adjustments. After adding the final portion of a titrant, the solution was stirred for additional 10 min and then transferred to DTS 1070 Capillary Zeta Cell (Malvern). For each *p*H value the Zeta potential was measured four times to calculate the average value and estimate the standard deviation.

1.2.11. *Surface specific area (SSA)*

Surface specific area (SSA) of bare and modified silica NPs was estimated from Brunauer–Emmett–Teller (BET) nitrogen isotherms measured with a help of a Gemini VII 2390 Surface Area Analyzer (Micromeritics Instrument Corp., Norcross, GA). Prior to the measurements SiNPs were dried for 1 h at 180 ^oC in vacuum and degassed for 2 h at 200 ^oC. Nitrogen gas absorption isotherms were measured using the following settings: 5 s equilibration time, 771.319 mmHg saturation

pressure, and sample mass of 221.1 mg for bare and 154.7 mg for modified silica. BET surface area for bare silica NPs was found to be 37.88 m^2/g out of which 5.48 m^2/g (*i.e.*, ≈14%) was attributed to the pores. For the surface-modified SiNPs the surface area was found to be 39.70 m^2/g out of which 7.86 m^2/g (*i.e.*, ≈20%) was the pore surface. These results indicate that SiNPs synthesized in this work have a low degree of porosity and that the silanization did not block the pores and, therefore, is not expected to prevent free diffusion of ligands and nitroxide labels in and out of the pores.

Assuming spherical morphology of synthesized silica nanoparticles of *ca*. 114 nm in diameter and an effective silica density of 1.87 g/cm^3 for these NPs,[71] the calculated SSA is 27.7 m^2/g, which correlates well with the BET surface area for the surface (32.40 m^2/g). Such a close agreement between the two methods for the surface area indicates that the synthesized SiNPs have a smooth surface and a high monodispersed. From experimental TGA and BET data for SiNPs functionalized with the ligands constituting either partially or fully hydrolyzed MPTMS, the ligand surface coverage was estimated as ≈0.36 or ≈0.43 ligands/nm^2 for the silanized and spin labeled SiNPs, respectively.

1.3 Results and Discussion

1.3.1. *Spin labeling of Silica Nanoparticles*

Typically, the surfaces of inorganic materials are functionalized with organic ligands either through a covalent bonding or by a physisorption.[72] However, physisorbed self-assembled monolayers have drawbacks of being thermally and solvolytically unstable as a result of relatively weak van der Waals forces and/or hydrogen bonding interactions responsible for an adhesion of these molecules to the surface.

Initially, we have attempted to covalently modify the surfaces of silica nanoparticles by

following the literature procedure involving a mere exposure of SiNPs to an ethanol solution of 3-mercaptopropyl trimethoxysilane at room temperature.[73] However, the consequent labeling of these silanized NPs with methanothiosulfonate spin label IKMTSL and further EPR titration experiments revealed that this method failed to provide a robust attachment of the organic ligands to the silica surface. Specifically, a progressive significant decrease in the amplitude of the EPR signal from the spin labeled NPs has been observed with each of the buffer exchange cycles (not shown). This decrease in EPR signal is a likely result of desorption of the physisorbed silane from the SiNP surface. In order to overcome this problem, we have employed a silanization under more harsh conditions such as heating of SiNPs in an acetonitrile solution of silane to 60 ^{o}C similar to the procedures previously described in the literature.[74–76] These silanization protocols afforded a silane coating that was stable in various organic solvents and also in aqueous solutions over a rather broad *p*H range from at least *ca*. 1.5 to 7.0 *p*H units. The amplitude of the EPR signal from these spin labeled nanoparticles remained essentially unchanged even after the numerous buffer exchange cycles (not shown).

Next, the silanization protocol was experimentally adjusted to make the surface ligand density sufficiently low so the dipolar and/or spin exchange broadening effects on the EPR spectra would be minimal if any. Initially, SiNPs were modified with MPTMS at a concentration of 10^{-5} mol/m^2 of silica surface. However, the consequent labeling of such surface-modified NPs with excess of IKMTSL resulted in EPR spectra with excessive line broadening caused by strong dipolar and/or spin exchange interactions (Fig. 1.10 A). A tenfold decrease in MPTMS concentrations to 10^{-6} mol/m^2 of silica surface significantly decreased the magnitude of the inter-spin magnetic interactions and resulted in well resolved X-band EPR spectra such as one shown in Fig. 1.10 B. Such a silanization protocol has been used for all the consecutive labeling

procedures.

While methanethiosulfonate of either IMTSL or IKMTS readily reacts with the SH-moiety in a solution under ambient conditions, unfavorable steric interactions of the SH-terminated ligands may prevent the complete ligand modifications with these reagents. It should be noted that the unreacted thiol groups may also cause the nitroxide detachment from the nanoparticles through the thiol-disulfide exchange reaction.[77,78] To avoid such a detachment and to exclude effects of the remaining free SH groups on the electrostatic properties of the spin labeled SiNPs, the unreacted thiols were further blocked by reacting with S-methyl methanethiosulfonate (MMTS).

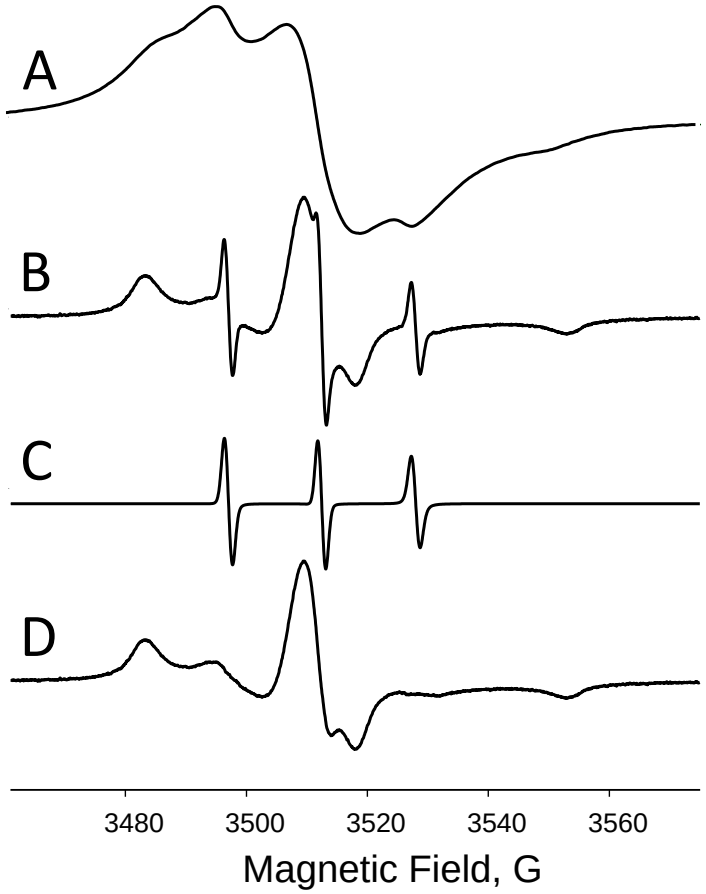

Figure 1.10. Experimental room temperature (21 ^{o}C) X-band EPR spectra of aqueous suspensions of silica nanoparticles of *ca*. 116 nm in diameter with a nitroxide IKMTSL covalently attached to the surface. Nanoparticles were initially modified with MPTMS at 10^{-5} mol/m^2 (A) and 10^{-6} mol/m^2 (B) of silica surface and then labeled with an excess of IKMTSL. The spectrum (A) was measured at *p*H≈7 and (B) at *p*H=8.53. The spectrum (B) was decomposed into a simulated fast (C) and a slow (D) motion component obtained by subtracting the fast component from the experimental spectrum using a least-squares procedure.[79] Based on calculated double integrals the fraction of the fast component (C) in the experimental spectrum (B) was 1.0% with the rest 99.0% of nitroxides giving rise to the slow-motion component (D). See text for details.

At *p*H>6.0 the EPR spectra revealed an appearance of a minor fast motion component in addition to a slow-motion EPR spectrum assigned to spin labeled ligands attached to the SiNP surface (Figure 1.10 B). The parameters of the fast motion component (Figure 1.10 C) were optimized using least-squares criteria applied to a numerically calculated fifth-harmonic of the experimental spectrum using the convolution-based filtering methods described earlier.[79] From calculating the corresponding double integrals the weight of the fast component (Figure 1.10 C) was just 1.0% with the rest 99% arising from the slow-motion components (Figure 1.10 D). The minor fast motion component is possibly originating from a small fraction of spin labeled ligands detaching from the NP surface. Such a detachment has most likely to do with the nature of the silica nanospheres that does not represent a continuous SiO_2 matrix but rather an agglomerate of smaller nanoparticles. Indeed, as it has been recently demonstrated, the formation of the individual silica nanospheres proceeds through an association of the primarily formed particles into larger assemblies and the growth of these assemblies occurs through the continuous addition of the primary much smaller particles to their surface.[80] Finally, we note that the absence of fast motion component in all EPR spectra of spin labeled SiNPs at *p*H<6.0 obtained after the multiple washes of SiNPs in acetonitrile, resuspension and storage of SiNP in an aqueous buffer at *p*H=5.0 demonstrates the robustness of attachment of the nitroxides to the silica surface using the protocols developed here.

As illustrated in Figure 1.10 the least-squares simulated minor fast motion component (Figure 1.10 C) could be subtracted from the experimental spectrum (Figure 1.10 B) yielding a slow-motion component (Figure 1.10 D). The latter component arising from spin labeled ligands attached to the SiNP surface was found to change as a function of *p*H. The changes in lineshape of the slow-motion components were further analyzed in the next section to derive local

electrostatic potential.

1.3.2. *Zeta Potential Measurements and EPR Titrations of Spin labeled Silica Nanoparticles*

The surface charge of silica surface is primarily determined by dissociation of silanol groups at the silica-water interface:[33]

$$\mathrm{SiOH} \leftrightarrows \mathrm{SiO^-} + \mathrm{H^+}$$

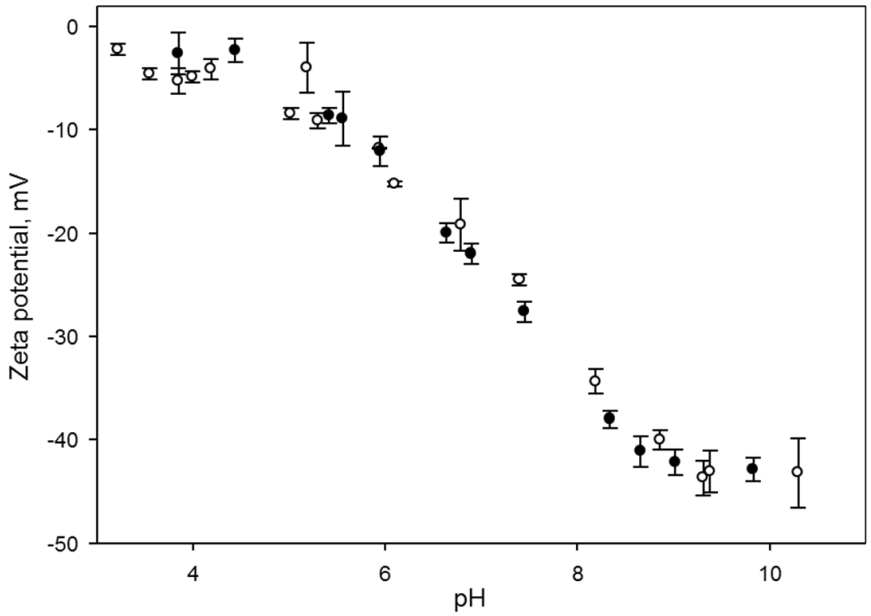

Figure 1.11. Zeta potential of silica nanoparticles as a function of bulk *p*H at room temperature (21 ^{o}C): (open circles) - as-prepared (bare) particles, (filled circles) – particles modified with (3-mercaptopropyl) trimethoxysilane and subsequently labeled with *p*H-sensitive IKMTSL nitroxide.

The surface silanols of SiNPs may not necessary exhibit the same pK_a's and their effective pK_a values are also expected to change with the surface charge. For these reasons, the surface charge density and the surface potential of silica are known to be changing continuously over a broad *p*H range rather than showing a single pK_a transition.[39,81] Such a charging behavior has been

observed for SiNPs from ζ-potential measurements. Figure 1.11 shows that the ζ-potential of as-prepared (bare) SiNPs (open circles) is close to zero (ζ≈- 3 mV) at *p*H<5 indicating an approximately electrically neutral surface of SiNPs. Above *p*H≈5 the ζ-potential is becoming increasingly negative with an increase in *p*H and then reaches a plateau at *p*H≈9 (Figure 1.11, open circles). The observed changes in electrophoretic mobility of bare silica nanoparticles with *p*H are in a close agreement with the results of Kobayashi *et al*.[39] Additional experiments with SiNPs decorated with MMTS and subsequently labeled with IKMTSL spin probe (Figure 1.11, filled circles) revealed essentially the same *p*H dependence of the ζ-potential. Thus, we conclude that the covalent modification of only a small fraction of the surface silanols with silanes and then nitroxides has little if any effects on the particle ζ-potential and, therefore, the surface electrostatic potential is expected to be unchanged.

Figure 1.12 compares room temperature X-band EPR spectra of SiNPs covalently modified with conventional non-ionizable spin label MTSL (A) and with pH-sensitive ionizable nitroxides IMTSL (B). The EPR spectra of SiNP-MTSL could be considered as a superposition of at least two components corresponding to fast and intermediate regimes of nitroxide tumbling with rotational correlation times τ_c<1 ns. Such a motion is expected for a small nitroxide attached to the silica surface via a flexible tether. Notably, the spectral shape is unaffected by *p*H and a significant negative charge, which is expected to develop at the SiNP surface at *p*H≈6.0 according to the ζ-potential data of Figure 1.11. The absence of spectral changes indicates that the immediate environment (*i.e*., microviscosity and polarity/hydrogen bonding environment) of this nitroxide tethered to the nanoparticle are not affected by *p*H at least within the sensitivity limits of the conventional spin labeling EPR. In contrast, EPR spectra of silica modified with ionizable nitroxide IMTSL display significant reversible changes over a broad *p*H range from 4.73 to 1.64

units (Figure 1.12 B). Because the non-ionizable probe MTSL reveals no changes in local microviscosity and polarity (Figure 1.12 A) the observed changes in rotational dynamics of IMTSL labeled silica must be attributable to the appearance of an ionized fraction of the nitroxide and some additional interactions of the charged nitroxide with the solvent and/or silica surface. We note that the changes in the nitroxide magnetic parameters alone would not explain the observed *p*H effects on EPR spectra. This ionized fraction is therefore responsible for the appearance of the low- and high-field shoulder peaks upon progressive increase in *p*H that are characteristic of a slower and a more restricted motion of the probe due to additional interactions. The spectra of the second ionizable nitroxide IMTSL attached to SiNPs were closer to the rigid limit than those for IMTSL (compare Figure 1.12 B and C) because of the additional steric interactions caused by the bulky aromatic ring and the ethyl group in the position 2 of the imidazoline heterocycle (Figure 1.8). While the IKMTSL EPR spectra did not change from *p*H=1.57 to *p*H=3.36 because of the significantly higher $pK_a^w = 5.68 \pm 0.01$ of this probe (Table 1.1), the outer nitrogen hyperfine coupling splitting $2A_{out}$ was measurably larger for the spectrum at *p*H=6.21 (Figure 1.12 C).

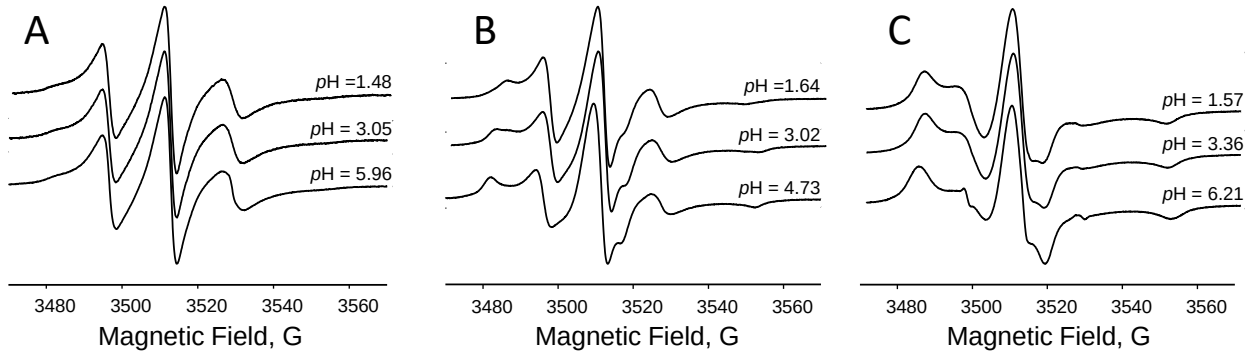

Figure 1.12. Representative room temperature (21 ^{o}C) X-band (9 GHz) EPR spectra of aqueous suspensions of silica nanoparticles modified with non-ionizable nitroxide MTSL (A) and ionizable pH-sensitive IMTSL (B) and IKMTSL (C) at several *p*H values as indicated in the Figure.

The changes in EPR spectra of an ionizable spin probe can be analyzed to reveal electrostatic properties of its local environment.[57] Typically, an experimental EPR spectrum at an intermediate *p*H can be decomposed into non-ionized and ionized components by least squares simulations to derive their fractions from double-integrated intensities.[82] Alternatively, the ionization state could be followed by measuring characteristic spectral parameters such as, for example, distances between the components originated from nitrogen hyperfine coupling.[78] For a series of EPR spectra collected in a course of an EPR titration experiment such parameters are then analyzed as a function of *p*H to derive $p\mathrm{K}_\mathrm{a}^{\mathrm{obs}}$, which is proportional to the logarithm of the apparent dissociation constant. Experimental $p\mathrm{K}_\mathrm{a}^{\mathrm{obs}}$ could be shifted from its intrinsic value $p\mathrm{K}_\mathrm{a}^{\mathrm{w}}$ in bulk water because of the additive contributions to the probe Gibbs free energy arising from effective local dielectric constant and electrostatic potential.[82] Thus,

$$p\mathrm{K}_\mathrm{a}^{\mathrm{obs}} = p\mathrm{K}_\mathrm{a}^{\mathrm{w}} + \Delta p\mathrm{K}_\mathrm{a}^{\mathrm{el}} + \Delta p\mathrm{K}_\mathrm{a}^{\mathrm{pol}} \tag{1.4}$$

where $\Delta p\mathrm{K}_\mathrm{a}^{\mathrm{pol}}$ is the shift due to local polarity/effective dielectric constant being different from that of bulk water and $p\mathrm{K}_\mathrm{a}^{\mathrm{el}}$ is the shift due to local electrostatic potential, Ψ. The latter is related to $\Delta p\mathrm{K}_\mathrm{a}^{\mathrm{el}}$ as:

$$\Delta p\mathrm{K}_\mathrm{a}^{\mathrm{el}} = \frac{-e\Psi}{ln(10)kT} \tag{1.5}$$

where *e* is the elementary charge, *k* is the Boltzmann constant.

Similar to other molecular *p*H probes,[82,83] determination of $\Delta p\mathrm{K}_\mathrm{a}^{\mathrm{el}}$ for ionizable nitroxides and consequently Ψ from the eq.(1.5) requires an accurate estimate of $\Delta p\mathrm{K}_\mathrm{a}^{\mathrm{pol}}$. Such an estimate is typically achieved by a titration of the probe at chemically and physically similar but electrically neutral interface.[82,84] We note that according to zeta potential measurements for SiNPs the surface

remains approximately electrically neutral (or at least ζ does not drop below ≈-5 mV) up to *p*H≈4-5 (Figure 1.11) and such a surface could be used as an electrically neutral reference point. Above *p*H=5 the surface is acquiring a negative charge till reaching the saturation at *p*H≈9 (Figure 1.11). Therefore, by selecting ionizable nitroxide labels with similar tether length but substantially different intrinsic $p\mathrm{K}_\mathrm{a}^\mathrm{w}$ one should be able to measure the polarity shift $\Delta p\mathrm{K}_\mathrm{a}^\mathrm{pol}$ using one nitroxide at *p*H range when the surface is still uncharged and then derive $\Delta p\mathrm{K}_\mathrm{a}^\mathrm{el}$ *vs*. *p*H when the surface is charged using the other nitroxide. Specifically to SiNPs, by selecting IMTSL spin label with intrinsic $p\mathrm{K}_\mathrm{a}^\mathrm{w}$ = 3.33±0.03 for an aqueous solution of its 2-mercaptoethanol adduct (19 $^\mathrm{o}$C, Table 1.1),[84] one should be able to measure $\Delta p\mathrm{K}_\mathrm{a}^\mathrm{pol}$ because at *p*H=3.3±1.0 the silica surface is expected to stay electrically neutral while IKMTSL with the intrinsic $p\mathrm{K}_\mathrm{a}^\mathrm{w}$ = 5.98±0.04 for an aqueous solution of its 2-mercaptoethanol adduct (21 $^\mathrm{o}$C, Table 1.1)[63] would allow for characterization of the surface charging at alkaline *p*H.

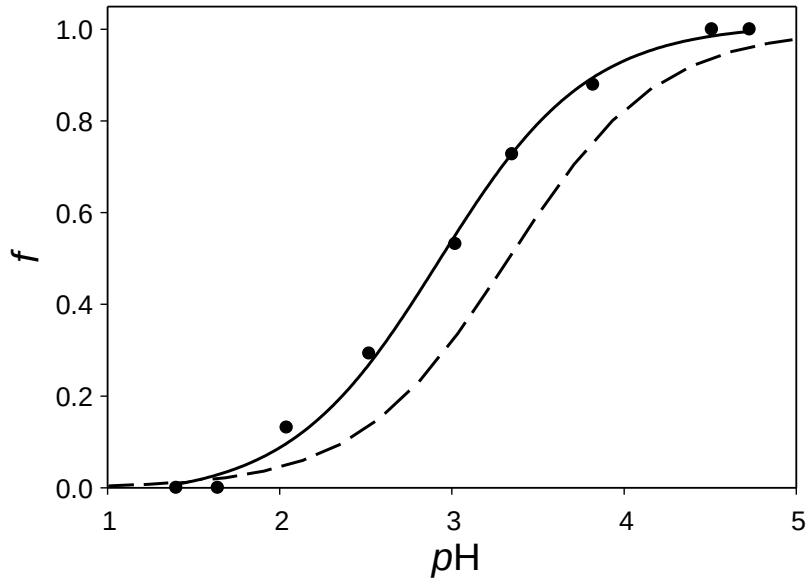

Figure 1.13. Experimental room temperature (21 °C) EPR titration of IMTSL-labeled silica nanoparticles (filled circles) measured as a fraction *f* of non-protonated nitroxide derived from least-squares simulations of EPR spectra. Solid line is least squares fit to the Henderson–Hasselbach equation (eq. 1.6) with $p\mathrm{K}_\mathrm{a}^{\mathrm{obs}} = 2.92 \pm 0.04$. The titration curve for IMTSL-2-mercaptoethanol (IMTSL-ME) in bulk water is shown as a dashed line using literature $p\mathrm{K}_\mathrm{a}$=3.33 data for 20 °C.[84]

Titration of SiNPs labeled with IMTSL revealed reversible changes in EPR spectra between *ca*. 2 and 4 *p*H units that were attributed to the nitroxide protonation. The fraction of the non-protonated nitroxide, *f*, was determined using least-squares fitting methods described earlier[57] and plotted *vs*. *p*H (filled circles, Figure 1.13). Fitting the titration data to the Henderson–Hasselbach equation:

$$f = \frac{1}{1 + 10^{p\mathrm{K}_\mathrm{a}^{\mathrm{obs}} - p\mathrm{H}}} \qquad (1.6)$$

yielded $p\mathrm{K}_\mathrm{a}^{\mathrm{obs}} = 2.92 \pm 0.04$ which is lower than $p\mathrm{K}_\mathrm{a}^{\mathrm{w}} = 3.33 \pm 0.03$ previously determined for IMTSL 2-mercaptoethanol adduct in water at 20 °C.[84] The corresponding titration curves are shown in Figure 1.13 as solid and dashed lines respectively. Considering that according to the ζ-potential data the silica surface remains uncharged below *p*H≈5, the observed $\Delta p\mathrm{K}_\mathrm{a} = -0.41 \pm 0.05$ can be assigned to the polarity effects, *i.e.*, $\Delta p\mathrm{K}_\mathrm{a}^{\mathrm{pol}} = -0.41 \pm 0.05$. Such a significant negative $p\mathrm{K}_\mathrm{a}$ shift indicates an altered dielectric environment near the silica surface *vs*. that of the bulk water. Previously, a series of EPR titrations of IMTSL-ME in water/isopropyl alcohol solutions of different volume proportions allowed for calibrating the polarity-induced changes in the probe dissociation constant measured as $\Delta p\mathrm{K}_\mathrm{a}^{\mathrm{pol}}$ *vs*. the bulk solvent dielectric permittivity, ε.[63,84] The calibration was shown to be linear at least for water/isopropyl alcohol solutions and it allows for estimating the local dielectric permittivity experienced by the nitroxide near silica surface as $\varepsilon_{\mathrm{eff}} = 70.8 \pm 5.0$. It should be noted here that magnetic parameters of the nitroxides – both $\boldsymbol{g}$-matrix and the nitrogen hyperfine coupling tensor $\boldsymbol{A}$ – are known to be affected by the dielectric properties of the solvent[85–87] and, therefore, potentially, could provide another estimate of $\varepsilon_{\mathrm{eff}}$. However, while the Onsager dielectric-continuum model of the reaction field for nitroxides was shown to work reasonably well for aprotic solvents,[87] analysis for the protic solvents employed in this work is complicated by the formation of a hydrogen bond between the oxygen of the nitroxide and the proton donor group of the solvent.[88–91] For this reason we did not attempt here to provide an estimate of $\varepsilon_{\mathrm{eff}}$ solely from magnetic parameters of the nitroxide and leave this question to future research.

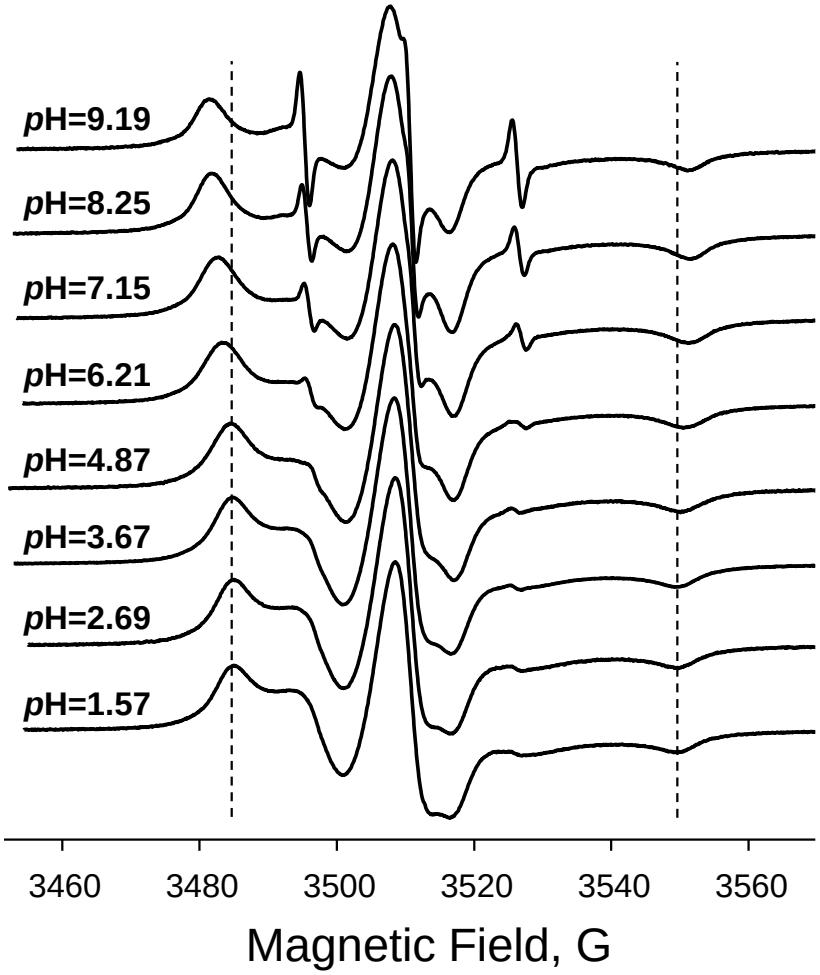

Figure 1.14. Representative room temperature (21 °C) X-band EPR spectra from *p*H titration experiments of aqueous suspension of SiNPs labeled with IKMTSL. Dashed lines indicate the positions of outer nitrogen hyperfine coupling splitting $2A_{out}$ for the fully protonated form of the nitroxide at *p*H=5.3.

Next, an EPR titration of SiNPs labeled with IKMTSL has been carried out. For this *p*H-sensitive spin label $pK_a^w = 5.98 \pm 0.04$ at 21 °C based on experimental data for the IKMTSL-ME adduct (Table 1.1)[63] and, therefore, its titration range overlaps with the dissociation region of the surface silanol groups that causes the surface to acquire a gradually increasing negative charge.

When attached to SiNPs, the EPR spectra of IKMTSL indicated a slow-motion regime with the outer nitrogen hyperfine coupling splitting $2A_{out}$ progressively increasing with increase in *p*H over a rather broad range (see Figure 1.14). This change in $2A_{out}$ is attributed to both changes in the nitroxide magnetic parameters upon deprotonation and some changes in the nitroxide rotational dynamics as the surface becomes negatively charged.

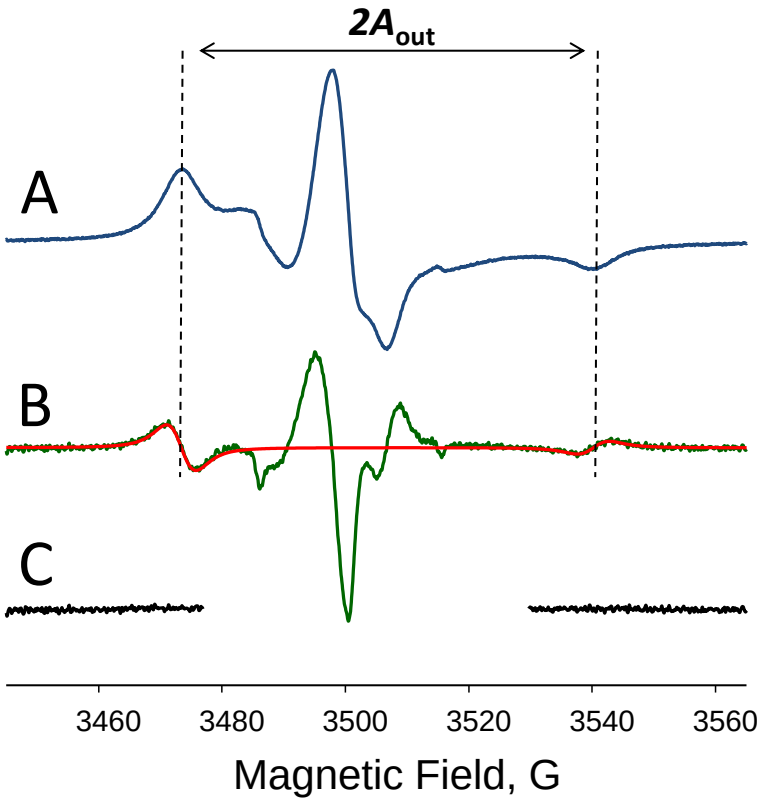

Figure 1.15. An illustration of a least-squares fitting procedure to determine the outer nitrogen hyperfine coupling splitting $2A_{out}$ from experimental slow motion EPR spectra on an example of room temperature (21 ^{o}C) spectrum (A, blue line) from an aqueous suspension of SiNPs labeled with IKMTSL and measured at pH=5.3.

On Figure 1.15, the calculated filtered second derivative spectrum (B, green line) improves

the resolution and allows for an empirical fitting of the outer spectral features to Voigt lineshapes (B, red line is superimposed on top of the green line) to derive $2A_{out}$ as the distance between position of the lines (shown as an arrow between the two dashed lines). (C, black line) is the fit residual, *i.e.*, the difference between a portion of the second derivative spectrum and the model.

Another notable feature was an appearance of fast motion component at *p*H>6 corresponding to a small fraction of the nitroxide detaching from the surface and discussed above. While the fast motion components could be effectively separated from the slow motion one as was demonstrated in Figure 1.10, for the measurements of the surface potential we have chosen a simpler route based on measurements of $2A_{out}$ from the experimental spectra.

In order to improve the accuracy in $2A_{out}$ determination without computationally intensive simulations of the multicomponent EPR spectra or subtracting the minor fast motion component as in Figure 1.10, a least-squares fitting to an empirical simplified model was employed (Fig. 1.15). Firstly, a filtered second derivative EPR spectrum (Fig. 1.15 B, green line) was calculated by a digital convolution of an experimental spectrum (Fig. 1.15 A) digitized to 2048 data points with a Lorentzian first derivative line with a peak-to-peak width of 3 data points. Such a convolution procedure was shown to yield a minimally broadened second-derivative EPR spectrum with a suppressed noise.[92] The broad spectral components in the second-derivative spectrum are getting suppressed allowing for fitting of the outer peaks to an empirical model of Voigt lineshapes (Fig. 1.15 B, red line). The fit residual of the outer peak region (Fig. 1.15 C) shows no systematic deviation between such a model and the digitally calculated second-derivative spectrum. Then the outer splitting $2A_{out}$ originating from the nitrogen hyperfine coupling is measured at the distance between the two simulated Voigt lineshapes (shown as an arrow and two dashed lines in Fig. 1.15).

Figure 1.16 summarizes results of A_{out} measurements from EPR titrations of SiNPs labeled

with only IKMTSL (open circles) and with IKMTSL and then MMTS to block the remaining free SH groups (filled circles). The data indicate a broad *p*H range for the probe coexisting in the protonated ($R^{\bullet}H^{+}$) and non-protonated ($R^{\bullet}$) forms because the plateaus were only reached below *p*H≈3 and above *p*H≈8-9 (Figure 1.16). From averaging the corresponding data points for both samples $A_{out}(R^{\bullet}H^{+})$=32.15±0.08 G and $A_{out}(R^{\bullet})$= 34.94±0.03 G were determined. Thus, changes in protonation state of IKMTSL attached to the SiNP surface results in ΔA_{out}=2.79±0.09 G. Assuming that changes in the nitroxide protonation state mainly affect A_{zz} and because $A_{\mathrm{iso}} = \frac{1}{3}\left(A_{\mathrm{xx}} + A_{\mathrm{yy}} + A_{\mathrm{zz}}\right)$, then for a spectrum approaching the rigid limit:

$$\Delta A_{\mathrm{iso}} = \frac{1}{3}\left(\Delta A_{\mathrm{xx}} + \Delta A_{\mathrm{yy}} + \Delta A_{\mathrm{zz}}\right) \approx \frac{1}{3}\Delta A_{\mathrm{zz}} \approx \frac{1}{3}\Delta A_{\mathrm{out}} \tag{1.7}$$

where A_{ii} are the principal components of the nitrogen hyperfine coupling tensor. Then the observed value $\Delta A_{\mathrm{out}} = 2.79 \pm 0.09$ G agrees well with $3A_{\mathrm{iso}} = 2.67 \pm 0.03$ G reported previously for the IKMTSL-ME adduct[63] indicating that essentially all of the changes in ΔA_{out} upon the nitroxide protonation are caused by the changes in the magnetic parameters of nitroxide but not the rotational motion.

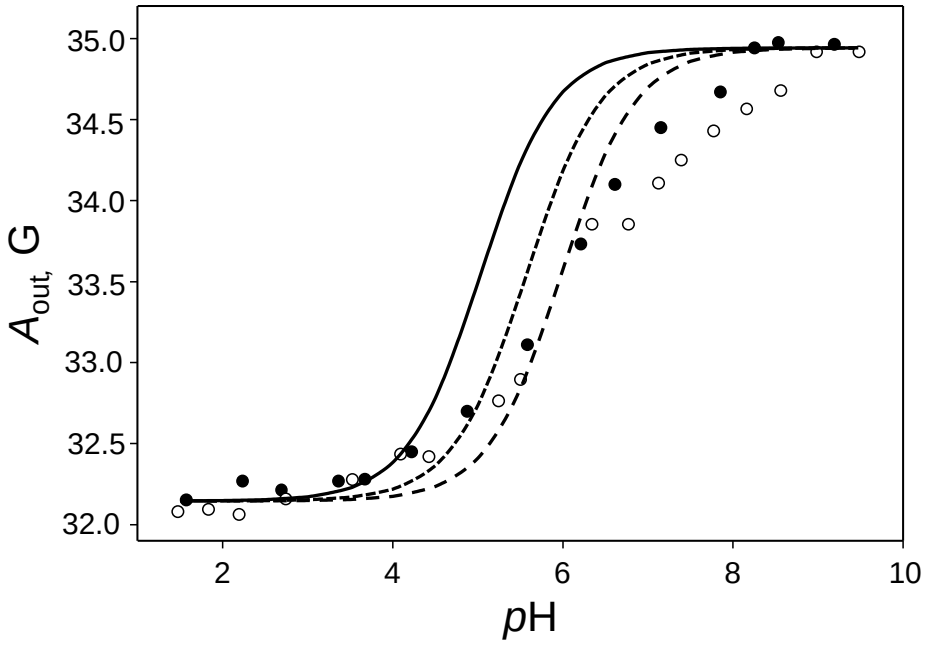

Figure 1.16. Experimental room temperature (21 °C) EPR titration A_{out} *vs*. *p*H curves measured for silica nanoparticles labeled with IKMTSL (open circles) and with IKMTSL and then MMTS to block the remaining free SH groups (filled circles). The nitrogen hyperfine coupling parameters for both of the samples were determined as $A_{out}(R^{\bullet}H^{+})$=32.15±0.08 G and $A_{out}(R^{\bullet})$= 34.94±0.03 G. Theoretical Henderson–Hasselbach titration curves for pK_a=5.02, 5.57, and 5.98 are shown as solid, short-dashed, and long-dashed lines, respectively. See text for details.

For a comparison, a theoretical Henderson–Hasselbach titration curve for IKMTS-ME in a bulk aqueous phase (pK_a=5.98 at 21 °C, Table 1.1)[63] is shown as a long-dashed line. Some large systematic deviations of the experimental data points from the theoretical curve provide a clear demonstration that local polarity and electric fields play large roles in the probe protonation state. If one assumes that the local effective dielectric constant experienced by IKMTSL is the same as for IMTSL, then the titration curve should be shifted by $\Delta pK_a^{pol} = -0.41$. Such a curve, shown as a short-dashed line in Figure 1.16, would intersect with the experimental data points at *p*H≈5

indicating *point of zero charge* (*pzc*) for SiNP surface. However, this value is significantly higher than *pzc*≈3-4 of *p*H units reported in both experimental[81] and theoretical studies.[32,34] Furthermore, our data on ζ-potential of SiNPs also indicate *pzc*≈4 units of *p*H (Figure 1.11). If the latter value of *pzc* is assumed, then $\Delta p\mathrm{K}_\mathrm{a}^{\mathrm{pol}} \approx -0.95$ and the corresponding theoretical curve in the absence of any electrostatic potential will be given by the solid line in the Figure 1.16. According to calibration data published earlier,[63] $\Delta p\mathrm{K}_\mathrm{a}^{\mathrm{pol}} \approx -0.95$ corresponds to $\varepsilon_{\mathrm{eff}} = 57\pm4$ for the label location.

In presence of an electrostatic potential, Ψ, the probe $p\mathrm{K}_\mathrm{a}$ is further shifted by $\Delta p\mathrm{K}_\mathrm{a}^{\mathrm{el}}$ given by eq.(1.5). Then from eqs.(1.4) and (1.6):

$$\Psi = \frac{-\ln(10)\,kT}{\mathrm{e}}\left(log_{10}\left(\frac{1}{f}-1\right) + p\mathrm{H} - \ p\mathrm{K}_\mathrm{a}^{\mathrm{w}} - \ \Delta p\mathrm{K}_\mathrm{a}^{\mathrm{pol}}\right) \tag{1.8}$$

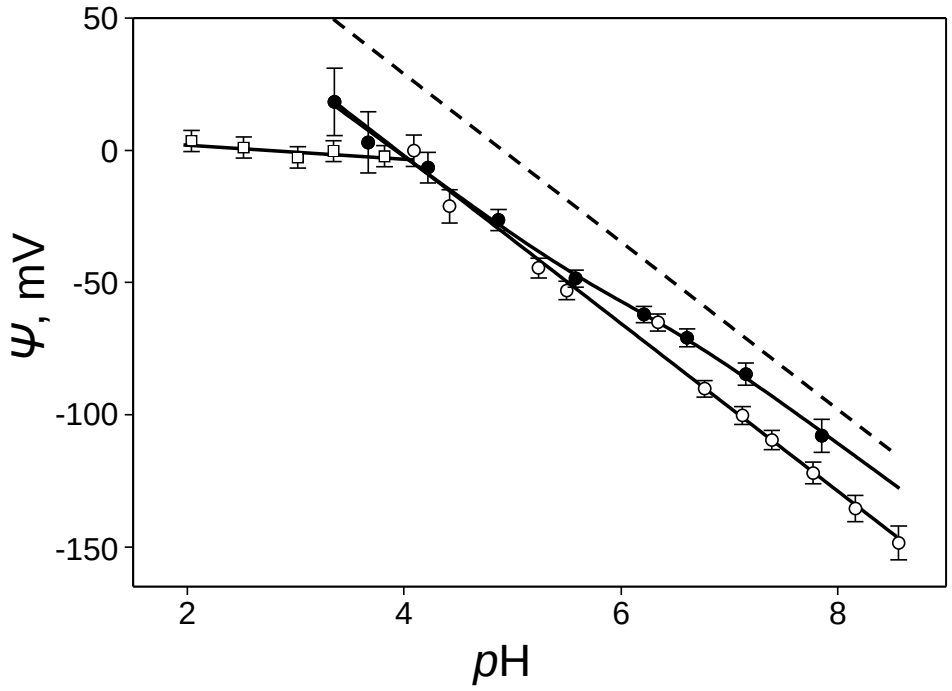

Figure 1.17. Near-surface electrostatic potential of SiNPs suspended in water at room temperature (21 °C) plotted as a function of *p*H. The potential was calculated using eq.(1.8) from the experimental EPR titrations shown in Figure 1.16 and setting $\Delta pK_a^{pol} \approx -0.95$. The data for SiNPs labeled with IKMTSL and containing some unreacted SH groups (open circles) could well fitted to a linear dependence given by eq. (1.8) and shown as a solid line. Dashed line shows Ψ *vs. p*H calculated for $\Delta pK_a^{pol} \approx -0.41$ obtained from EPR titrations of SiNPs labeled with IMTSL. The data for SiNPs labeled with IKMTSL and then MMTS to block the remaining free SH groups (filled circles) show somewhat lower Ψ at *p*H>6; the corresponding solid line is given as a guide for an eye. The data for IMTSL-labeled SiNPs are shown as open circles; the solid line is a linear regression.

Figure 1.17 shows *p*H dependence of the surface electrostatic potential of SiNPs calculated from the EPR titration data of Figure 1.16 using eq.(1.8). We note that because of the

$log_{10}\left(\frac{1}{f}-1\right)$ term the values of Ψ are only determined for $0 < f < 1$ and the function diverges at both $f \to 0$ and $f \to 1$. For these reasons only the data points that make physical sense were plotted in Figure 1.17. The error bars were estimated by assuming 2% error in determination the fraction *f* of the non-ionized nitroxide. The choice of $\Delta p\mathrm{K}_\mathrm{a}^{\mathrm{pol}}$ provides for a vertical offset of the data but does not change the gradient of Ψ changes with *p*H; the data shown were calculated for $\Delta p\mathrm{K}_\mathrm{a}^{\mathrm{pol}} \approx -0.95$. The data for SiNPs labeled with IKMTSL and containing some unreacted SH groups (open circles) were least-squares fitted to the following linear dependence:

$$\Psi = (125.0 \pm 2.8) - (31.73 \pm 0.45) \cdot p\mathrm{H}, \qquad R^2 = 0.991 \tag{1.9}$$

where Ψ is in mV. The corresponding linear regression is shown as a solid line in Figure 1.17. The dashed line shows Ψ *vs*. *p*H calculated for $\Delta p\mathrm{K}_\mathrm{a}^{\mathrm{pol}} \approx -0.41$ obtained from EPR titrations of SiNPs labeled with IMTSL. The latter dependence would correspond to $pzc \approx 4.9$ units of *p*H which would contradict the ζ-potential data of Figure 1.11.

We note that the linear model approximates the charging of the surface of SiNPs with *p*H surprisingly well (Figure 1.17). The data also show that the surface potential, associated with silanol deprotonation, develops at a wide *p*H range, starting at *p*H≈4 and continues at least up to *p*H ≈ 8 – 9 where the IKMTSL label reaches its sensitivity limit. However, as it was observed from the ζ-potential data of Figure 1.11, the latter highly basic region corresponds to the completely deprotonated silanols. When eq.(1.8) was applied to EPR titration data of Figure 1.13 obtained for SiNPs labeled with IMTSL, the corresponding data showed only minor deviations from $\Psi = 0$ (open squares, Figure 1.17). This is in a full agreement with the results of other studies.[32,34,49,81] Overall, the EPR titration curves obtained with the two labels cover the full dissociation range of the silica surface groups.

The data for SiNPs labeled with IKMTSL and then MMTS to block the remaining free SH groups (filled circles) demonstrated somewhat lower Ψ at *p*H>6; the corresponding solid line is given as a guide for an eye in Figure 1.17. Alternatively, it could also be fitted to a straight line with a lesser slope of -27.01± 0.30 mV/*p*H. A possible reason for such a deviation is a thiol – silanol proton exchange reaction:

$$\mathrm{R-SH + SiO^- \rightleftarrows R-S^- + SiOH} \tag{1.10}$$

Indeed, deuteron exchange in thiols has been reported previously for molecules in solutions.[93] Proximity of the surface silanol groups and unlabeled thiols could be a reason for the reversible proton transfer. As the surface charge is developing with an increase in *p*H so is the number of the charged silanols. The latter should shift the reaction towards the products. For SiNPs containing thiol-terminated ligands which were blocked by reacting with MMTS the number of available thiols is expected to decrease dramatically. Because the nitroxide tags are covalently attached to silanes, the surface silanols are partially screened from the *p*H-reporting nitroxides and such a screening would affect the measured surface potential. The observed linear growth in the magnitude of the negative surface potential suggests that the behavior of the surface ionizable groups is highly dependent on their local environments. Thus, it is more natural to consider the silanol dissociation constant as a shifting parameter affected by the state of the surrounding groups, rather than a constant.

Finally, we note that according to spin labeling EPR data the near surface electric potential at $p\mathrm{H} \approx 8.5$ is $\Psi = -148 \pm 6$ mV, which is significantly higher in magnitude than the zeta potential $\zeta = -44 \pm 2$ mV measured from DSL experiments. Such a large – more than threefold – difference is likely caused by effective screening of the surface charges by the counter ions at the position of the slipping plane where the zeta potential is measured.

1.4. Conclusions

For the first time, the surface potential of monodispersed silica nanoparticles in aqueous solution has been measured over a broad range of *p*H by spin labeling EPR of two ionizable nitroxides covalently attached to the nanoparticle surface. Monodispersed nanoparticles of *ca*. 116 nm in diameter were synthesized using the Stöber method. Silanization method under harsh conditions including heating of nanoparticles in an acetonitrile solution of silane to 60 ^{o}C has been developed to ensure robust attachment of the thiol-terminated ligands to the silica surface. These ligands were consequently modified with either of the two *p*H-sensitive nitroxides to provide a broader *p*H range – essentially from *p*H≈2 to *p*H≈9 for characterization of the surface electrostatic potential of the nanoparticles. The spin labeling procedures have been optimized to reduce effects of magnetic interspin interactions and to yield well-resolved EPR spectra.

EPR titration data for these two *p*H-sensitive nitroxide probes allowed for differentiating the dielectric and electrostatic contributions to the interfacial properties of SiNPs. At the acidic *p*H<4 the surface of SiNPs is expected to be uncharged and therefore the EPR titration with the first *p*H EPR molecular tag, IMTSL, was expected to be unaffected by the surface electrostatic potential. From such a titration an effective local dielectric constant at the silica nanoparticle-water interface was found to be ε_{eff}=70.8±5.0 (Table 1.1). EPR titration of SiNPs labeled with the second EPR tag IKMTSL, which has a higher intrinsic $p\mathrm{K}_\mathrm{a}^\mathrm{w} = 5.98 \pm 0.04$ at 21 ^{o}C (Table 1.1), allowed to monitor charging of the silica surface up to *p*H≈9. By assuming *pzc*≈4.0 units of *p*H for silica that was confirmed by parallel zeta potential measurements, the local dielectric environment of IKMTSL EPR tag was found to have a somewhat lower $\varepsilon_{\mathrm{eff}} = 57$±4 (Table 1.1). This lower $\varepsilon_{\mathrm{eff}}$ could be related to a more hydrophobic nature of the IKMTSL label so it would become more closely associated with the surface hydrophobic ligands than IMTSL. This is in

agreement with IKMTSL demonstrating X-band EPR spectra close to the rigid limit whereas as IMTSL spectra demonstrated a higher rate of molecular tumbling (compare characteristic EPR spectra shown in Figs. 1.12 A and Figure 1.12 B).

EPR titration data were then used to calculate surface electrostatic potential as a function of *p*H. The data demonstrated an approximately linear dependence of the surface potential on *p*H starting at *p*H≈4 and increasing in magnitude up to *p*H ≈ 8 – 9 where the IKMTSL EPR label reaches its sensitivity limit. This is in agreement with the existing literature on the surface potential associated with the silanol deprotonation that is known to develop over a wide *p*H range. While the attachment linker employed for the two nitroxides has some flexibility, it still ensures the location of the *p*H-sensitive tags close to the surface. Specifically, the distance between the N of the amidine moiety undergoing protonation and the nearest Si atom of the electrically neutral silica cluster was estimated to be 17.9 Å using molecular modelling (Figure 1D.1, Appendix 1D). This distance decreased 3.1 Å when the tether was bent by placing three negative charges on the silica cluster and giving the nitroxide amidine group a positive charge. We note that although in the nitroxide the N-O moiety is the EPR reporting group, it is the nitroxide amidine group that undergoes protonation. Therefore, the measured local dielectric constant and electrostatic potential should be attributed to the midpoint of the N atom of the amidine group but not the midpoint of the N-O bond.

Because of the close (0.3-1.8 nm) proximity of the nitroxide *p*H-sensing moiety to the surface, the values of the electrostatic surface potential reported by these molecular probes are significantly higher than those reported by the zeta potential measurements. Specifically, according to EPR, the surface potential increases up to $\Psi = -148 \pm 6$ mV at *p*H ≈ 8.5 whereas the zeta potential reaches $\zeta = -44 \pm 2$ mV plateau at about the same *p*H values. It is worthwhile

to note here that $\psi \approx -148$ mV at the surface of SiNPs is about the same as the near surface electrostatic potential of lipid bilayer membranes composed of 100% of anionic phospholipids (from -124 to -183 mV depending on temperature and electrolyte concentration).[82] The latter measurement have been carried out using the same nitroxide IMTSL tethered to the head group of a phospholipid.[82] Thus, potentially, SiNPs could be employed as model objects with very similar surface electrostatic properties as small unilamellar lipid vesicles.

Overall, spin labeling methods developed here expand the applicability of spin labeling EPR to interfacial electrostatic properties of metal oxide nanoparticles as very similar labeling procedures could be employed for other surfaces terminated by OH groups. Both local effective dielectric constants and electrostatic potential could be measured. Such measurement capability and especially a better-defined location of *p*H-reporting moiety with respect to the interface are viewed to be important for developing and further refining theoretical model for nanoparticle-water interface as well for studying other nanostructures to which conventional zeta potential measurements cannot be applied.

References

(1) Shylesh, S., Schünemann, V. & Thiel, W. R. Magnetically separable nanocatalysts: bridges between homogeneous and heterogeneous catalysis. *Angew. Chem. Int. Ed. Engl.* **49**, 3428–3459 (2010).

(2) Manoudis, P. *et al.* Polymer-Silica nanoparticles composite films as protective coatings for stone-based monuments. *J. Phys. Conf. Ser.* **61**, 1361–1365 (2007).

(3) Li, H., Ding, G.-S., Chen, J. & Tang, A.-N. Amphiphilic silica nanoparticles as pseudostationary phase for capillary electrophoresis separation. *J. Chromatogr. A* **1217**, 7448–7454 (2010).

(4) López, T. *et al.* Treatment of Parkinson's disease: nanostructured sol-gel silica-dopamine reservoirs for controlled drug release in the central nervous system. *Int. J. Nanomedicine* **6**, 19–31 (2010).

(5) Tang, L., Fan, T. M., Borst, L. B. & Cheng, J. Synthesis and Biological Response of Size-Specific, Monodisperse Drug–Silica Nanoconjugates. *ACS Nano* **6**, 3954–3966 (2012).

(6) Slowing, I. I., Trewyn, B. G., Giri, S. & Lin, V. S.-Y. Mesoporous Silica Nanoparticles for Drug Delivery and Biosensing Applications. *Adv. Funct. Mater.* **17**, 1225–1236 (2007).

(7) Caltagirone, C., Bettoschi, A., Garau, A. & Montis, R. Silica-based nanoparticles: a versatile tool for the development of efficient imaging agents. *Chem. Soc. Rev.* **44**, 4645–4671 (2015).

(8) Acharya, B., Chestnut, M., Marek, A., Smirnov, A. I. & Krim, J. A Combined QCM and AFM Study Exploring the Nanoscale Lubrication Mechanism of Silica Nanoparticles in Aqueous Suspension. *Tribol. Lett.* **65**, 115 (2017).

(9) Jal, P. K., Patel, S. & Mishra, B. K. Chemical modification of silica surface by immobilization of functional groups for extractive concentration of metal ions. *Talanta* **62**, 1005–1028 (2004).

(10) Asefa, T. & Tao, Z. Biocompatibility of Mesoporous Silica Nanoparticles. *Chem. Res. Toxicol.* **25**, 2265–2284 (2012).

(11) Betancor, L. & Luckarift, H. R. Bioinspired enzyme encapsulation for biocatalysis. *Trends Biotechnol* **26**, 566–572 (2008).

(12) Tan, S. Y., Ang, C. Y., Li, P., Yap, Q. M. & Zhao, Y. Drug Encapsulation and Release by Mesoporous Silica Nanoparticles: The Effect of Surface Functional Groups. *Chem. – A Eur. J.* **20**, 11276–11282 (2014).

(13) Zhou, Y. *et al.* Mesoporous silica nanoparticles for drug and gene delivery. *Acta Pharm. Sin. B* **8**, 165–177 (2018).

(14) Bagwe, R. P., Hilliard, L. R. & Tan, W. Surface modification of silica nanoparticles to reduce aggregation and nonspecific binding. *Langmuir* **22**, 4357–4362 (2006).

(15) Kim, K.-M. *et al.* Surface treatment of silica nanoparticles for stable and charge-controlled colloidal silica. *Int. J. Nanomedicine* **9 Suppl 2**, 29–40 (2014).

(16) Lundqvist, M. *et al.* Nanoparticle size and surface properties determine the protein corona with possible implications for biological impacts. *Proc. Natl. Acad. Sci.* **105**, 14265 LP – 14270 (2008).

(17) Nel, A. E. *et al.* Understanding biophysicochemical interactions at the nano-bio interface. *Nat. Mater.* **8**, 543–557 (2009).

(18) Liu, Z. *et al.* Tribological properties of nanodiamonds in aqueous suspensions: effect of the surface charge. *RSC Adv.* **5**, 78933–78940 (2015).

(19) Ong, S., Zhao, X. & Eisenthal, K. B. Polarization of water molecules at a charged interface: second harmonic studies of the silica/water interface. *Chem. Phys. Lett.* **191**, 327–335 (1992).

(20) Ostroverkhov, V., Waychunas, G. A. & Shen, Y. R. New Information on Water Interfacial Structure Revealed by Phase-Sensitive Surface Spectroscopy. *Phys. Rev. Lett.* **94**, 46102 (2005).

(21) Sulpizi, M., Gaigeot, M.-P. & Sprik, M. The Silica-Water Interface: How the Silanols Determine the Surface Acidity and Modulate the Water Properties. *J. Chem. Theory Comput.* **8**, 1037–1047 (2012).

(22) Pfeiffer-Laplaud, M., Costa, D., Tielens, F., Gaigeot, M.-P. & Sulpizi, M. Bimodal Acidity at the Amorphous Silica/Water Interface. *J. Phys. Chem. C* **119**, 27354–27362 (2015).

(23) Delgado, A. V, González-Caballero, F., Hunter, R. J., Koopal, L. K. & Lyklema, J. Measurement and interpretation of electrokinetic phenomena. *J. Colloid Interface Sci.* **309**, 194–224 (2007).

(24) Tarafdar, J. & Adhikari, T. Nanotechnology in Soil Science. in 775–807 (2015).

(25) Goumans, T. P. M., Wander, A., Brown, W. A. & Catlow, C. R. A. Structure and stability of the (001) α-quartz surface. *Phys. Chem. Chem. Phys.* **9**, 2146–2152 (2007).

(26) Bandura, A. V, Kubicki, J. D. & Sofo, J. O. Periodic Density Functional Theory Study of Water Adsorption on the α-Quartz (101) Surface. *J. Phys. Chem. C* **115**, 5756–5766 (2011).

(27) Sulpizi, M., Gaigeot, M. P. & Sprik, M. The silica-water interface: How the silanols determine the surface acidity and modulate the water properties. *Journal of Chemical Theory and Computation* vol. 8 1037–1047 (2012).

(28) Leung, K., Nielsen, I. M. B. & Criscenti, L. J. Elucidating the Bimodal Acid−Base Behavior of the Water−Silica Interface from First Principles. *J. Am. Chem. Soc.* **131**, 18358–18365 (2009).

(29) Patwardhan, S. V *et al.* Chemistry of Aqueous Silica Nanoparticle Surfaces and the Mechanism of Selective Peptide Adsorption. *J. Am. Chem. Soc.* **134**, 6244–6256 (2012).

(30) Leung, K., Nielsen, I. M. B. & Criscenti, L. J. Elucidating the bimodal acid-base behavior of the water-silica interface from first principles. *J. Am. Chem. Soc.* **131**, 18358–18365 (2009).

(31) Dewan, S. *et al.* Structure of Water at Charged Interfaces: A Molecular Dynamics Study. *Langmuir* **30**, 8056–8065 (2014).

(32) Atalay, S., Ma, Y. & Qian, S. Analytical model for charge properties of silica particles. *J. Colloid Interface Sci.* **425**, 128–130 (2014).

(33) Behrens, S. H. & Grier, D. G. The charge of glass and silica surfaces. *J. Chem. Phys.* **115**, 6716–6721 (2001).

(34) Barisik, M., Atalay, S., Beskok, A. & Qian, S. Size dependent surface charge properties of silica nanoparticles. *J. Phys. Chem. C* **118**, 1836–1842 (2014).

(35) White, L. R. Approximate analytic solution of the Poisson-Boltzmann equation for a spherical colloid particle. *J. Chem. Soc. Farday II* **73**, 377–396 (1977).

(36) Bhattacharjee, S. DLS and zeta potential - What they are and what they are not? *J. Control. Release* **235**, 337–351 (2016).

(37) Liu, X., Li, H., Li, R. & Tian, R. Analytical solutions of the nonlinear Poisson–Boltzmann equation in mixture of electrolytes. *Surf. Sci.* **607**, 197–202 (2013).

(38) Conte, M., Miyamura, H., Kobayashi, S. & Chechik, V. Enhanced acyl radical formation in the Au nanoparticle-catalysed aldehydeoxidation. *Chem. Commun.* **46**, 145–147 (2010).

(39) Kobayashi, M., Juillerat, F., Galletto, P., Bowen, P. & Borkovec, M. Aggregation and Charging of Colloidal Silica Particles: Effect of Particle Size. *Langmuir* **21**, 5761–5769 (2005).

(40) Lowry, G. V *et al.* Guidance to improve the scientific value of zeta-potential measurements in nanoEHS. *Environ. Sci. Nano* **3**, 953–965 (2016).

(41) Lützenkirchen, J. *et al.* Potentiometric Titrations as a Tool for Surface Charge Determination. *Croat. Chem. Acta* **85**, 391–417 (2012).

(42) Schaefer, J., Gonella, G., Bonn, M. & Backus, E. H. G. Surface-specific vibrational spectroscopy of the water/silica interface: screening and interference. *Phys. Chem. Chem. Phys.* **19**, 16875–16880 (2017).

(43) Lovering, K. A., Bertram, A. K. & Chou, K. C. New Information on the Ion-Identity-Dependent Structure of Stern Layer Revealed by Sum Frequency Generation Vibrational Spectroscopy. *J. Phys. Chem. C* **120**, 18099–18104 (2016).

(44) Fitts, J. P. *et al.* Second-harmonic generation and theoretical studies of protonation at the water/α-TiO2 (110) interface. *Chem. Phys. Lett.* **411**, 399–403 (2005).

(45) Brown, M. A. *et al.* Measure of surface potential at the aqueous-oxide nanoparticle interface by XPS from a liquid microjet. *Nano Lett.* **13**, 5403–5407 (2013).

(46) Na Kim, H. & Keun Lee, S. *Atomic Structure and Dehydration Mechanism of Amorphous*

Silica: Insights from 29Si and 1H Solid-State MAS NMR Study of SiO2 Nanoparticles. vol. 120 (2013).

(47) Murray, D. K. Differentiating and characterizing geminal silanols in silicas by (29)Si NMR spectroscopy. *J. Colloid Interface Sci.* **352**, 163–170 (2010).

(48) Kobayashi, T., Perras, F. A., Slowing, I. I., Sadow, A. D. & Pruski, M. Dynamic Nuclear Polarization Solid-State NMR in Heterogeneous Catalysis Research. *ACS Catal.* **5**, 7055–7062 (2015).

(49) Lowe, B., Skylaris, C.-K., Green, N., Shibuta, Y. & Sakata, T. Calculation of Surface Potentials of the Silica-Water Interface using Molecular Dynamics: Challenges and Opportunities. *Jpn. J. Appl. Phys.* **57**, 04FM02 (2018).

(50) Ionita, P., Caragheorgheopol, A., Gilbert, B. C. & Chechik, V. Mechanistic Study of a Place-Exchange Reaction of Au Nanoparticles with Spin-Labeled Disulfides. *Langmuir* **20**, 11536–11544 (2004).

(51) Zachary, M. & Chechik, V. Hopping of Thiolate Ligands between Au Nanoparticles Revealed by EPR Spectroscopy. *Angew. Chemie Int. Ed.* **46**, 3304–3307 (2007).

(52) Ionita, P., Volkov, A., Jeschke, G. & Chechik, V. Lateral Diffusion of Thiol Ligands on the Surface of Au Nanoparticles: An Electron Paramagnetic Resonance Study. *Anal. Chem.* **80**, 95–106 (2008).

(53) Khlestkin, V. K., Polienko, J. F., Voinov, M. A., Smirnov, A. I. & Chechik, V. Interfacial Surface Properties of Thiol-Protected Gold Nanoparticles: A Molecular Probe EPR Approach. *Langmuir* **24**, 609–612 (2008).

(54) Smirnov, A. I., Ruuge, A., Reznikov, V. A., Voinov, M. A. & Grigor'ev, I. A. Site-Directed Electrostatic Measurements with a Thiol-Specific pH-Sensitive Nitroxide: Differentiating Local pK and Polarity Effects by High-Field EPR. *J. Am. Chem. Soc.* **126**, 8872–8873 (2004).

(55) Voinov, M. A., Ruuge, A., Reznikov, V. A., Grigor'ev, I. A. & Smirnov, A. I. Mapping local protein electrostatics by EPR of pH-sensitive thiol-specific nitroxide. *Biochemistry* **47**, 5626–5637 (2008).

(56) Voinov, M. A. & Smirnov, A. I. Spin Labels and Spin Probes for Measurements of Local pH and Electrostatics by EPR. in *Electron Spin Resonance Specialist Periodical Reports* (ed. Chechik, V.) vol. 22 71–106 (The Royal Society of Chemistry, 2010).

(57) Voinov, M. A. & Smirnov, A. I. Ionizable Nitroxides for Studying Local Electrostatic Properties of Lipid Bilayers and Protein Systems by EPR. *Methods Enzymol.* **564**, 191–217 (2015).

(58) Kovaleva, E. G. *et al.* Acid–Base Properties of Nanoconfined Volumes of Anodic Aluminum Oxide Pores by EPR of pH-Sensitive Spin Probes. *J. Phys. Chem. C* **120**, 2703–2711 (2016).

(59) Kovaleva, E. G. *et al.* Interfacial Electrostatic Properties of Hydrated Mesoporous and Nanostructured Alumina Powders by Spin Labeling EPR. *Cell Biochem. Biophys.* **75**,

159–170 (2017).

(60) Bordignon, E. EPR Spectroscopy of Nitroxide Spin Probes. *eMagRes* 235–254 (2017) doi:https://doi.org/10.1002/9780470034590.emrstm1513.

(61) Donohue, M. P. On the Nature of Electrostatics at the Interface of Transmembrane Peptides and Lipid Bilayers. (2014).

(62) Berliner, L. J., Grunwald, J., Hankovszky, H. O. & Hideg, K. A novel reversible thiol-specific spin label: papain active site labeling and inhibition. *Anal. Biochem.* **119**, 450–455 (1982).

(63) Voinov, M. A., Scheid, C. T., Kirilyuk, I. A., Trofimov, D. G. & Smirnov, A. I. IKMTSL-PTE, a Phospholipid-Based EPR Probe for Surface Electrostatic Potential of Biological Interfaces at Neutral pH: Effects of Temperature and Effective Dielectric Constant of the Solvent. *J. Phys. Chem. B* **121**, 2443–2453 (2017).

(64) Stöber, W., Fink, A. & Bohn, E. Controlled growth of monodisperse silica spheres in the micron size range. *J. Colloid Interface Sci.* **26**, 62–69 (1968).

(65) Zhuravlev, L. T. The surface chemistry of amorphous silica. Zhuravlev model. *Colloids Surfaces A Physicochem. Eng. Asp.* **173**, 1–38 (2000).

(66) Alaouie, A. M. & Smirnov, A. I. Ultra-stable temperature control in EPR experiments: Thermodynamics of gel-to-liquid phase transition in spin-labeled phospholipid bilayers and bilayer perturbations by spin labels. *J. Magn. Reson.* **182**, 229–238 (2006).

(67) Margita, K., Voinov, M. A. & Smirnov, A. I. Effect of Solution Ionic Strength on the pK(a) of the Nitroxide pH EPR Probe 2,2,3,4,5,5-Hexamethylimidazolidin-1-oxyl. *Cell Biochem. Biophys.* **75**, 185–193 (2017).

(68) Kovaleva, E. G. *et al.* Proton Activity in Nanochannels Revealed by Electron Paramagnetic Resonance of Ionizable Nitroxides: A Test of the Poisson-Boltzmann Double Layer Theory. *J. Phys. Chem. C* **122**, 20527–20538 (2018).

(69) Smirnov, A. I. & Belford, R. L. Rapid Quantitation from Inhomogeneously Broadened EPR Spectra by a Fast Convolution Algorithm. *J. Magn. Reson. Ser. A* **113**, 65–73 (1995).

(70) Smirnov, A. I. & Smirnova, T. I. Convolution-based algorithm: from analysis of rotational dynamics to EPR oximetry and protein distance measurements. in *EPR: Instrumental Methods* 277–348 (Springer, 2004).

(71) Kimoto, S. *et al.* Characterization of nanosized silica size standards. *Aerosol Sci. Technol.* **51**, 936–945 (2017).

(72) Zhao, B. & Brittain, W. Polymer Brushes: Surface-Immobilized Macromolecules. *Prog. Polym. Sci.* **25**, 677–710 (2000).

(73) Steinberg, G., Stromsborg, K., Thomas, L., Barker, D. & Zhao, C. Strategies for covalent attachment of DNA to beads. *Biopolymers* **73**, 597–605 (2004).

(74) Brunel, D. Functionalized micelle-templated silicas (MTS) and their use as catalysts for fine chemicals. *Microporous Mesoporous Mater.* **27**, 329–344 (1999).

(75) Hoegaerts, D., Sels, B. F., De Vos, D. E., Verpoort, F. & Jacobs, P. A. Heterogeneous tungsten-based catalysts for the epoxidation of bulky olefins. *Catal. Today* **60**, 209–218 (2000).

(76) Shylesh, S., Sharma, S., Mirajkar, S. P. & Singh, A. P. Silica functionalised sulphonic acid groups: synthesis, characterization and catalytic activity in acetalization and acetylation reactions. *J. Mol. Catal. A Chem.* **212**, 219–228 (2004).

(77) Hermanson, G. The Reactions of Bioconjugation. in 229–258 (2013). doi:10.1016/B978-0-12-382239-0.00003-0.

(78) Khramtsov, V. V & Volodarsky, L. B. Use of Imidazoline Nitroxides in Studies of Chemical Reactions ESR Measurements of the Concentration and Reactivity of Protons, Thiols, and Nitric Oxide. in *Biological Magnetic Resonance: Volume 14: Spin Labeling* (ed. Berliner, L. J.) 109–180 (Springer US, 2002). doi:10.1007/0-306-47072-1_4 LB - Khramtsov2002.

(79) Smirnov, A. I. Post-processing of EPR spectra by convolution filtering: Calculation of a harmonics' series and automatic separation of fast-motion components from spin-label EPR spectra. *J. Magn. Reson.* **190**, 154–159 (2008).

(80) Carcouët, C. C. M. C. *et al.* Nucleation and growth of monodisperse silica nanoparticles. *Nano Lett.* **14**, 1433–1438 (2014).

(81) Brown, M. A. *et al.* Determination of Surface Potential and Electrical Double-Layer Structure at the Aqueous Electrolyte-Nanoparticle Interface. *Phys. Rev. X* **6**, 11007 (2016).

(82) Voinov, M. A., Rivera-Rivera, I. & Smirnov, A. I. Surface Electrostatics of Lipid Bilayers by EPR of a pH-Sensitive Spin-Labeled Lipid. *Biophys. J.* **104**, 106–116 (2013).

(83) Fromherz, P. Lipid Coumarin Dye as a Probe of Interfacial Electrical Potential in Biomembranes. *Methods Enzymol.* **171**, 376–387 (1989).

(84) Voinov, M. A., Kirilyuk, I. A. & Smirnov, A. I. Spin-labeled pH-sensitive phospholipids for interfacial pKa determination: synthesis and characterization in aqueous and micellar solutions. *J. Phys. Chem. B* **113**, 3453–3460 (2009).

(85) Griffith, O. H., Dehlinger, P. J. & Van, S. P. Shape of the hydrophobic barrier of phospholipid bilayers (Evidence for water penetration in biological membranes). *J. Membr. Biol.* **15**, 159–192 (1974).

(86) Smirnov, A. I. & Smirnova, T. I. Resolving domains of interdigitated phospholipid membranes with 95 GHz spin labeling EPR. *Appl. Magn. Reson.* **21**, 453–467 (2001).

(87) Marsh, D. Reaction fields and solvent dependence of the EPR parameters of nitroxides: the microenvironment of spin labels. *J. Magn. Reson.* **190**, 60–67 (2008).

(88) Gagua, A. V, Malenkov, G. G. & Timofeev, V. P. Hydrogen bond contribution to the isotropic hyperfine splitting constant of a nitroxide free radical. *Chem. Phys. Lett.* **56**, 470–473 (1978).

(89) Smirnova, T. I., Smirnov, A. I., Paschenko, S. V & Poluektov, O. G. Geometry of

hydrogen bonds formed by lipid bilayer nitroxide probes: A high-frequency pulsed ENDOR/EPR study. *J. Am. Chem. Soc.* **129**, 3476–3477 (2007).

(90) Smirnova, T. I. *et al.* Local polarity and hydrogen bonding inside the Sec14p phospholipid-binding cavity: High-field multi-frequency electron paramagnetic resonance studies. *Biophys. J.* **92**, 3686–3695 (2007).

(91) Owenius, R., Engström, M., Lindgren, M. & Huber, M. Influence of Solvent Polarity and Hydrogen Bonding on the EPR Parameters of a Nitroxide Spin Label Studied by 9-GHz and 95-GHz EPR Spectroscopy and DFT Calculations. *J. Phys. Chem. A* **105**, 10967–10977 (2001).

(92) Smirnov, A. I. Post-processing of EPR spectra by convolution filtering: Calculation of a harmonics series and automatic separation of fast-motion components from spin-label EPR spectra. *J. Magn. Reson.* **190**, 154–159 (2008).

(93) Khurma, J. R. & Fenby, D. V. Thermodynamics of Deuterium Exchange Reactions in Water-Thiol and Alcohol-Thiol Systems. *Aust. J. Chem.* **32**, 755–759 (1979).

Appendix 1A: EPR spectra of acetonitrile supernatants from consecutive washes of spin labeled silica nanoparticles

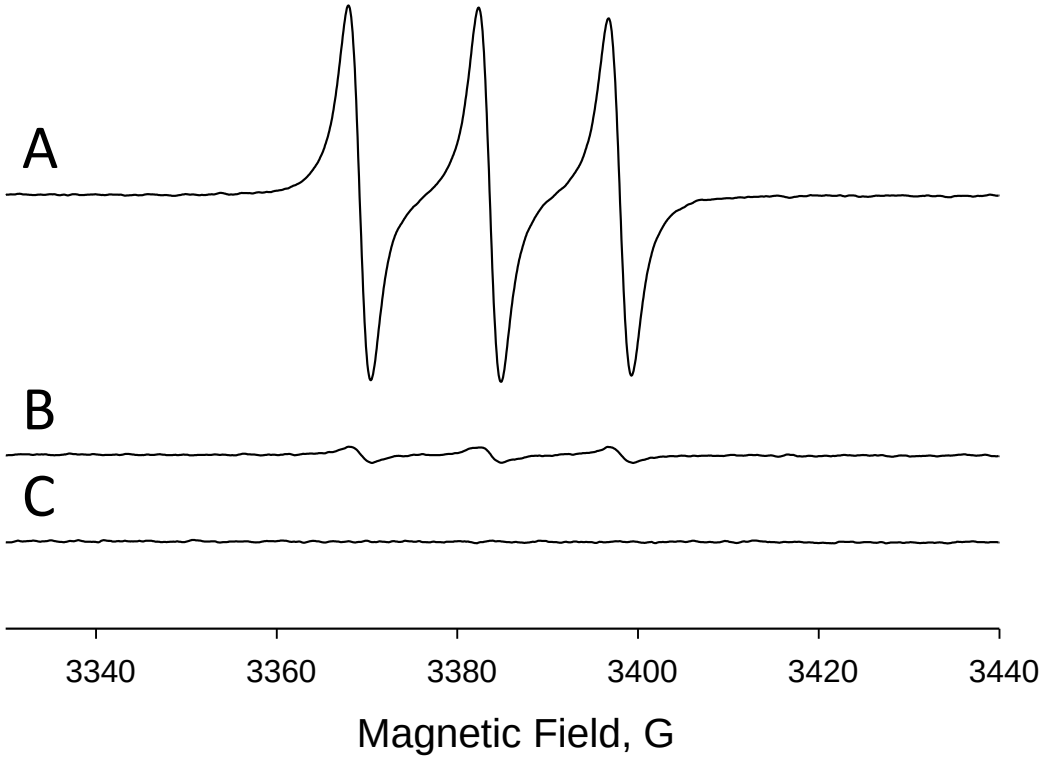

Figure 1A.1. Representative room temperature X-band (9 GHz) EPR spectra of acetonitrile supernatant collected after consecutive washes of spin labeled silica nanoparticles: (A) – after first wash, (B) – second wash, (C) – third wash. All the solutions were studied as collected without any further processing or deoxygenation.

Appendix 1B: Calculations of ionic strength vs. pH

Before titration experiments a set of Tris buffers with a desired pH value was prepared using deionized water. The initial buffer had Tris concentration of 50 mM and *p*H=7.0. Additional buffers were prepared by titrating the initial 50 mM Tris buffer with either concentrated solutions of HCl or NaOH.

Ionic strength of such buffer solutions at different *p*H values was estimated by using the standard acid-basic equilibrium equations and the known equilibria dissociation constants for H_2O and Tris at 25 °C (K_w=1·10^{-14} M^2 and K_a=8.5·10^{-9} M, respectively). Specifically, the electro-neutrality condition for all the ions involved yields:

$$[\mathrm{H^+}] + [\mathrm{Na^+}] + [\mathrm{Tris^+}] = [\mathrm{Cl^-}] + [\mathrm{OH^-}] \tag{1B.1}$$

Further,

$$K_\mathrm{w} = [\mathrm{H^+}][\mathrm{OH^-}] \tag{1B.2}$$

$$K_\mathrm{a} = \frac{[\mathrm{H^+}][\mathrm{Tris}]}{[\mathrm{Tris^+}]} \tag{1B.3}$$

Finally, we write the mass balance equation for total Tris concentration $[\mathrm{Tris}]_\mathrm{o}$:

$$[\mathrm{Tris}]_\mathrm{o} = [\mathrm{Tris^+}] + [\mathrm{Tris}] \tag{1B.4}$$

and the total salt concentration $[\mathrm{NaCl}]_\mathrm{o}$:

$$[\mathrm{NaCl}]_\mathrm{o} = [\mathrm{Na^+}] + [\mathrm{Cl^-}] \tag{1B.5}$$

Provided that one either performs acidic titration with a constant $[\mathrm{Na^+}] = [\mathrm{Na^+}]_0 = \mathrm{const}$ concentration or alkaline titration with $[\mathrm{Cl^-}] = [\mathrm{Cl^-}]_0 = \mathrm{const}$, there are 4 equations for 4 unknown ion concentrations. The system of equations was readily solved using a Matlab (MathWorks, Inc., Natick, MA) script. Then the ionic strength for the monovalent species is calculated as:

$$\begin{aligned} I = \frac{1}{2}([\mathrm{H^+}] + [\mathrm{Na^+}] + [\mathrm{Tris^+}] + [\mathrm{Cl^-}] + [\mathrm{OH^-}]) = \\ = [\mathrm{H^+}] + [\mathrm{Na^+}] + [\mathrm{Tris^+}] = [\mathrm{Cl^-}] + [\mathrm{OH^-}] \end{aligned} \tag{1B.6}$$

The results of such calculations of the ionic strength *I* are plotted in Figure 1B.1 as a function of *p*H.

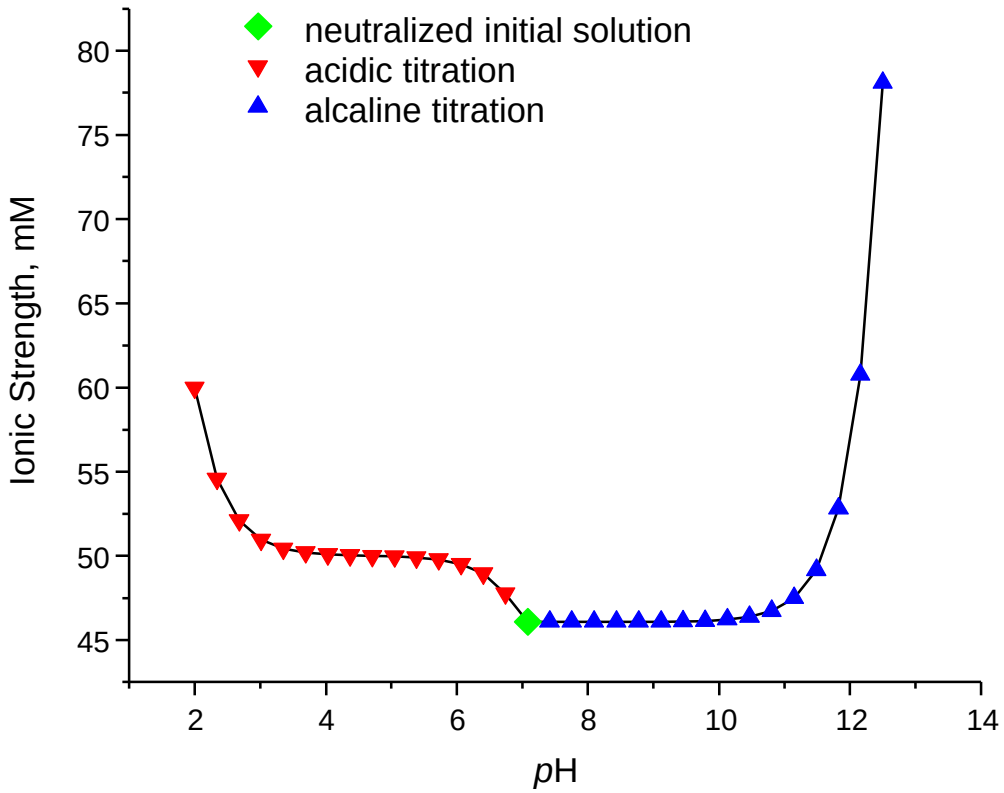

Figure 1B.1. Ionic strength of 50 mM Tris buffer solution in deionized water as a function of *p*H for SiNP titration experiments at room temperature (25 ^{o}C). Initially, 50 mM Tris buffer was prepared at *p*H=7.0. Ionic strength of this neutralized solution was calculated to be $I \approx 46$ mM (green diamond). The points corresponding to the acidic titration upon adding a concentrated solution of HCl are shown as red triangles while the points of the alkaline titration obtained by adding concentrated NaOH solution are shown as blue triangles. The solid line is a guide for an eye. The results indicate that the ionic strength of the individual buffers varied from 51 mM to 46 mM (or ±5%) within *p*H=3.0 to pH=11.0 range. See the main text for further details.

Appendix 1C: An example of a decomposition of an EPR spectrum of a spin labeled SiNP into two components corresponding to protonated and non-protonated forms.

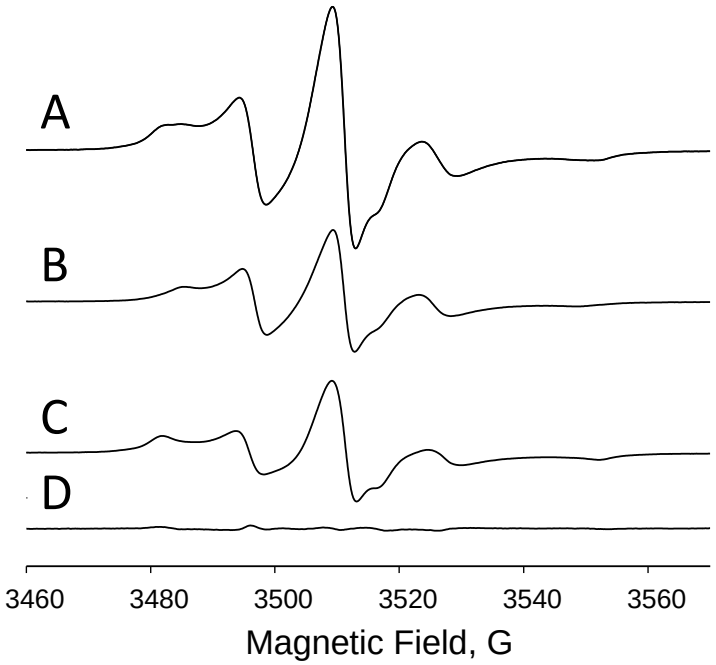

Figure 1C.1. (A) X-band (9.5 GHz) room temperature (21 ^{o}C) EPR spectrum of aqueous suspensions of silica nanoparticles modified with ionizable *p*H-sensitive nitroxide IMTSL and equilibrated with 50 mM Tris buffer at *p*H=3.02. The spectrum (A) was decomposed into a superposition of a spectrum at *p*H=1.64 (B) corresponding to the fully protonated nitroxide and a spectrum at *p*H=4.73 (C) corresponding to fully non-protonated nitroxide. From calculating the double integrated intensities, the fraction of the non-protonated nitroxide in the spectrum (A) is *f*=54%. (D) Residual of the fit, *i.e.*, the difference between the spectrum (A) and the sum of spectra (B) and (C). Note that (A), (B), and (C) spectra are the results of the digital convolution of the experimental spectra with a first integral Lorentzian function with full width at half height of $\Delta B_{1/2} = 0.253$ G.

Appendix 1D: Estimation of distances between the N atom of the nitroxide amidine group and the silica surface

While in *p*H-sensitive nitroxides the N-O moiety is the EPR reporting group, it is the nitroxide amidine group that undergoes reversible protonation. Therefore, the measured local dielectric constant and electrostatic potential should be attributed to the midpoint of the N atom of the amidine group but not the N-O bond. In order to estimate the possible distances between the midpoint of the N atom of the amidine group of IKMTSL and the silica surface, the silica surface was modelled as a cluster consisting of 9 Si and 18 O atoms (Figure 1D.1). The structure of such a model silica cluster attached to (3-mercaptopropyl) trimethoxysilane and labeled with the nitroxide IKMTSL was optimized using MM2 method (Chem3D Ultra 9.0 software, CambridgeSoft, Waltham, MA, USA). The atoms were color-coded as follows: white (H), grey (C), blue (N), red (O), yellow (S), violet (Si), pink (lone pair of electrons).

To estimate the shortest distance between the N atom of the N–H and the silica cluster, the N7 atom (Figure 1D.1A**)** of the amidine group was given a positive charge (+1), and silanoate oxygens O51, O52, and O54 were given negative (-1) charges. The distance between N7 and the nearest Si atom (Si38) of the negatively charged silica cluster was estimated to be 3.1 Å.

To estimate the longest distance between the nitrogen atom N7 of the protonatable amidino group and the nearest Si atom (Si34) of the electrically neutral silica cluster no electrical charges were given to neither the N7 atom of the amidine group or any of the silanoate oxygens. The distance between N7 and the nearest Si atom (Si38) of the negatively charged silica cluster was estimated to be 17.9 Å.

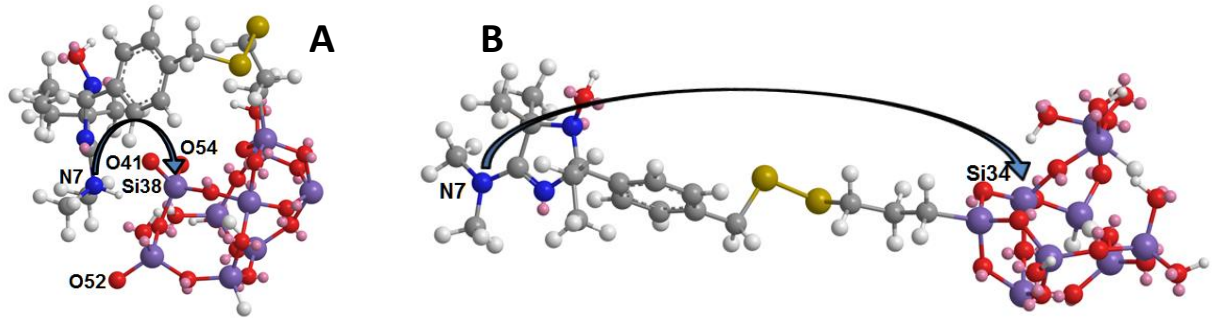

Figure 1D.1. The structures of a model silica cluster attached to (3-mercaptopropyl) trimethoxysilane and labeled with the nitroxide IKMTSL obtained from an optimization using MM2 method (Chem3D Ultra 9.0 software, CambridgeSoft, Waltham, MA, USA). The atoms are color-coded as follows: white (H), grey (C), blue (N), red (O), yellow (S), violet (Si), pink (lone pair of electrons).

(A) The structure for the spin labeled ligand attached to a negatively charged silica surface was approximated by giving the silanoate oxygens O51, O52, and O54 the negative (-1) charges while the N7 atom of the amidine group was given a positive charge (+1). The distance between the N7 atom of the amidino group and the nearest Si atom (Si38) was 3.144 Å. The distance between the N-O midpoint and the nearest Si atom (Si38) was 5.526 Å.

(B) The structure for the spin labeled ligand attached to a neutral silica surface was approximated by not giving charges to any of the atoms, the distance between the N7 atom of the amidino group and the nearest Si atom (Si38) was 17.868 Å. The distance between the N-O midpoint and the nearest Si atom (Si38) was 15.426 Å.

CHAPTER 2

Effects of Ionic Strength on Local Dielectric and Electrostatic Properties of Water-Silica Interface by Spin Labeling EPR

Vladislav Perelygin, Maxim A. Voinov, Antonin Marek, and Alex I. Smirnov

2.1 Introduction

Among all nanomaterials available today, silica nanoparticles (SiNPs) are the most widely used and versatile ones. For example, SiNPs have been employed in various areas of biomedical research as imaging agents[1] and biosensors.[2] Surface-functionalized silica nanoparticles have been used as substrates for proteins[3] and antibodies immobilization.[4] Mesoporous[5] and lipid-coated SiNPs[6] were utilized as a vehicle for controlled drug delivery. Industrial applications of SiNPs include, among the others, using them as the friction-reducing agents[7] and recyclable catalysts for the synthesis of thioethers and thioesters.[8] In the field of agriculture, SiNPs have been reported to increase germination rates[9] and demonstrate pesticide activity while applied to wheat or barley directly.[10] SiNPs also serve as a pesticide agent careers.[11]

Several factors make silica so versatile, such as highly elaborated synthesis pathways that provide a monodispersed product with well controlled average size,[12–14] and chemical stability, that allows silica to retain its properties across a vast range of adverse conditions including extreme pH, salt concentration and temperatures.[15,16] Besides, surface of silica could be readily modified to achieve different goals, for example, for increasing solubility in diverse media[17] or creating magnetic monodisperse NPs.[18] Since the first synthesis of monodisperse silica nanoparticles by Stöber in 1968,[19] the properties of this material have been thoroughly investigated and comprehensive models of NPs stability,[20] synthesis mechanism,[21] and surface chemistry[22,23] have

been developed. However, some of the SiNPs properties, such as local polarity and electrostatics, are hard to address due to the fact that these phenomena operate only in a close proximity to the surface, at the angstrom scale, thus making application of the most analytical techniques problematic.

Surface of bare silica is covered with silanol hydroxy groups – Si-OH, also known as silanols. It is commonly accepted that there are two types of silanols (in approx. 1 to 5 ratio) with $pK_a \approx 4.5$ and $pK_a \approx 8.5$[24]; therefore, silica surface acquires a negative charge under neutral and basic conditions. As a result, positively charged ions along with the counter ions are attracted to the surface of SiNPs forming an electric double layer surrounding NPs. This causes a rearrangement of the hydrogen bonding network at the nanoparticle surface, which, in turn, affects the interfacial polarity. Thus, the properties of silica nanoparticles are mostly determined by the properties of their interfacial region. For example, surface electrostatic potential defines intermolecular interactions, thus, controlling aggregation and stability of NPs.[25] This property is critical for designing efficient nanoparticle-based lubricant additives.[7,20] Hydroxylated surface of silica creates a hydrophilic environment and combined with ionic effects of the electric double layer, might provide favorable conditions for binding of some molecules, while denying the others. Protein adsorption,[26] as well as biocatalytic activity and cellular uptake,[27] heavily rely on fine tuning of these properties.

Ionization state of the surface silanol groups, as well as their capabilities to form hydrogen bonds with the surface water molecules, have been investigated in detail by both experimentally and theoretically.[24,28–31] Water-silanol interactions were thoroughly studied by computation methods, such as density functional theory (DFT)[32,33] and molecular dynamics (MD),[29,30,34,35]

providing insightful information on the interactions on the atomic scale. A series of continuum electrostatic simulations explored macroscale characteristics of the charged surface[36–38] of silica.

Although various aspects of the interfacial properties of silica have been addressed theoretically, there are only a limited number of experimental techniques capable of assessing these properties experimentally. The most conventional of the experimental methods seems to be zeta potential (ζ) determination. It is based on the measurement of electrophoretic mobility of nanoparticles, that allows to calculate the electric potential at the shear plane of the NP double layer, where the surface is effectively screened by ionic species.[20,39] However, zeta potential measurement does not report on the particle electrostatics directly, the electrophoretic mobility data are further employed to calculate potentials using the Smoluchowski theory.[40] Phase-sensitive sum-frequency vibrational spectroscopy (SFVS) has been used to elucidate the interfacial interactions of silanols with water molecules and ionic species.[28,41,42] Other methods, such as second harmonic generation (SHG)[24] and x-ray photoelectron spectroscopy (XPS)[43–45] have also been used to study electrostatic surface potential and screening effect.

The dielectric properties of the interface are well known to strongly depend on the distance from the surface.[46–49] It was reported that the relative permittivity decreases dramatically inside the diffuse double layer. The effect is already seen at the distance of 5 nm from the NP surface and it increases exponentially, so at the region below 1 nm the dielectric constant is approximately as twice as lower than that in a bulk solution.[47] MD simulation also shown that water molecules near the nanoparticle interface, at the distance of 7 nm and closer, are highly polarized, which causes a significant shift in the relative permittivity.[48] The existence of this state, that resembles the structure of ice, has also been confirmed experimentally.[49,50]

One of the currently available experimental techniques that allows for assessing surface electrostatic and polarity effects in structurally-diverse systems, is a spin labeling electron paramagnetic resonance (EPR) spectroscopy. EPR is a highly sensitive technique, it requires only micromolar spin probe concentrations, and, as it has been demonstrated, to be suitable for studying various nanoparticle surface-related phenomena.[51–54] Earlier, we employed the EPR spectroscopy of the pH-sensitive spin labeled ligands to studying the interfacial properties of the thiol-protected Au NPs[55] and to assessing interfacial electrostatics[51–53] and polarity[59–61] of the lipid bilayers and detergent micelles. We also demonstrated the applicability of the pH-sensitive nitroxides for probing the polarity inside the nanopores of Anodic Aluminum Oxide (AAO).[62,63]

Recently, we reported on probing the interfacial electrostatic and polarity properties of silica nanoparticles labeled with pH-sensitive spin probes[64] by means of EPR spectroscopy. In the present work we focused on the effects of ionic screening on dielectric and electrostatic characteristics of water-silica interface. We have covalently modified monodispersed silica nanoparticles (average diameter of 108 nm) with thiol-terminated ligands and spin labeled them with pH-sensitive nitroxides via a thiol-click chemistry. This approach ensures that a spin probe is located in a well-defined region of space in a close proximity to the surface. The spin labeled SiNPs were EPR titrated in solutions with various ionic strengths. We employed two pH-sensitive nitroxide spin labels, *S*-(1-oxyl-2,2,3,5,5-pentamethylimidazolidin-4-yl)methyl methanesulfono-thioate (IMTSL) and *S*-4-(4-(dimethylamino)-2-ethyl-5,5-dimethyl-1-oxyl-2,5-dihydro-1*H*-imidazol-2-yl (IKMTSL) (Fig. 2.1). When attached to a thiol SH group, the pK_a's of these probes are pK_a=3.33[59] and pK_a=5.92,[65] respectively. Magnetic parameters of these nitroxides depend explicitly on their ionization (protonation) state. Changes in magnetic parameters of the IMTSL cover the pH range of pH≈1.33÷5.33, where silica nanoparticles are only weakly negatively

charged due to a small fraction (~15%) of acidic silanols (pK_a≈4.5), while IKMTSL covers the pH range of pH≈3.92÷7.92, where silica nanoparticles are negatively charged due to ionization of both acidic and basic (pK_a≈8.5) silanols.

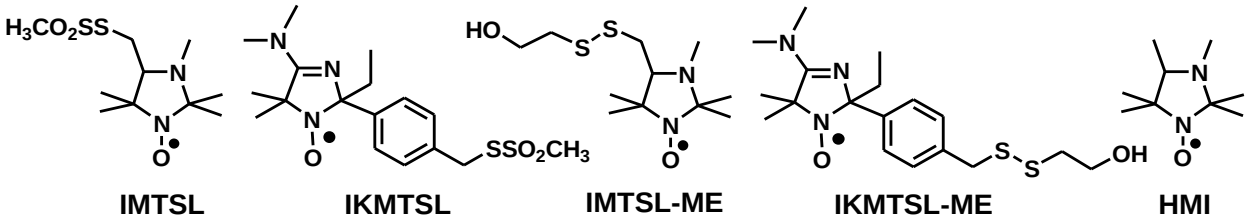

Figure 2.1. Chemical structures of the nitroxides used in this chapter.

This allowed us to target effects of salt concentration on dielectric and electrostatic properties of the silica-water interface within two different ranges of pH.

2.2 Experimental Section

2.2.1. *pH Calibration for Ionic Strength of NaCl*

Standard pH buffers by BDH®, for 5-point calibration were used at pH values 1.68, 4.00, 7.00, 10.00, 12.45 at 25°C. Solutions were prepared using ACS grade sodium chloride (99.0% NaCl) by BDH®, sodium hydroxide pellets, 98% by Alfa Aesar®, hydrochloric acid, certified ACS Plus by Fisher Scientific, and in-house deionized water. Batch solutions of NaCl in DI water at different ionic strength were prepared at concentrations 0.05 M, 0.1 M, 0.2 M, 0.3M, 0.5 M, 1.0 M, 1.5 M, 2.0 M. The titration was automated using a home built titrator. The titration setup consisted of a high precision programmable syringe pump Braintree Scientific, Inc., model BS-800, digital pH meter with 4 significant figures and serial port output Oakton 450 combined with Metler Toledo pH-probe, InLab® Micro. Titration took place in a 50mL beaker enclosed in a water-jacketed beaker connected to PolyScience temperature circulator, model 9710. Whole setup was

controlled using a standard PC and Matlab code allowing for fully automated titration. All solutions were thoroughly bubbled before and during titration with argon gas using a thin PTFET tubing, AWG 21L, connected to pressure tank cylinder. For solution infusion standard BD Luer Lok Tip syringes (20mL, 60mL) connected through needles to the same type of PTFET tubing were used. For the purpose of the gravimetric syringe pump calibration, high precision Sartorius micro balance, model CPA225D, was used. Please, refer to Appendix 2A for further details on the experiment and pH calibration.

2.2.2. *Synthesis, Modification and Characterization of Silica Nanoparticles*

Synthesis, modification and characterization of silica nanoparticles were described in detail in Experimental Section of Chapter 1. Refer to sections 1.2.1 - 1.2.5, 1.2.9 and 1.2.11.

2.2.3. *Zeta potential Titrations*

Zeta titration procedure was described in detail in Experimental Section of Chapter 1. Refer to sections 1.2.10. Preparation of NaCl solutions was described in section 2.2.1.

2.2.4. *EPR Titration Experiments*

EPR titration procedure, including spectrometer settings, was described in detail in Experimental Section of Chapter 1. Refer to sections 1.2.6 and 1.2.7. Preparation of NaCl solutions was described in section 2.2.1.

2.3 Results and Discussion

2.3.1. *Characterization and modification of Silica Nanoparticles*

Silica NPs with an average diameter of 108 nm were synthesized using the Stöber process.[19] The obtained NPs were thoroughly characterized using SEM and DLS to confirm the size and monodispersity. Surface of the NPs was modified with (3-mercaptopropyl)

trimethoxysilane (MPTMS).[64] The functionalization efficiency was estimated to be of ~ 0.4 ligands/nm^2,[64] as it was inferred from the results of Brunauer–Emmett–Teller (BET) nitrogen absorption, providing specific surface area (SSA) and TGA analyses. Based on the SSA results, it was also concluded that the SiNPs have a low degree of porosity and that the silane ligands did not block the pores. The terminal thiol groups of the silane ligands were spin labeled with either IMTSL or IKMTSL spin probe (Figure 2.1) with a labeling efficiency of ~30 %. The details of the synthesis, surface functionalization, spin labeling, and NPs characterization were described in our previous work.[64]

2.3.2. *Zeta Potential Titrations*

Both bare and spin labeled SiNPs were characterized by ζ-potential measurement within a broad range of pH and ionic strength. When the pH of the medium approaches the region of ionization of the surface silanol groups of silica (pK_{a1}≈4.5, pK_{a2}≈8.5) (Eq. 2.1), the particle acquires a negative charge:

$$\mathrm{SiOH} \leftrightarrows \mathrm{SiO^-} + \mathrm{H^+} \tag{2.1}$$

Both the dissociation constant of silanols and the surface charge development are well known to depend on the solution ionic strength. For example, in NaCl solutions the isoelectric point of ζ-potential titration of colloid silica has been shown to vary from pH=2.0 (for 0.001 M) to pH=4.5 (for 0.4 M) depending on ionic strength of the solution.[66]

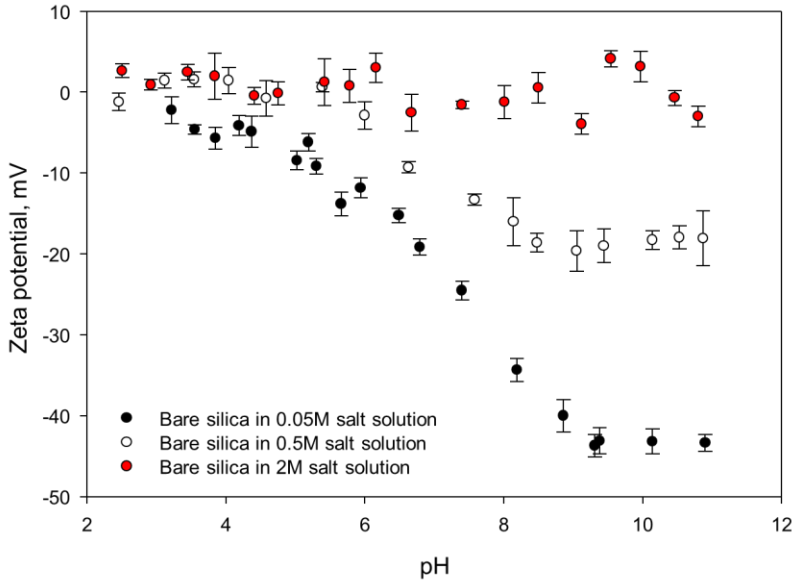

Figure 2.2. Zeta potentials of bare (nonmodified) 108 nm silica nanoparticles shown as a function of pH. Data were acquired at 21 ^{o}C, electrolyte (NaCl) concentrations were 0.05 M (filled circles), 0.5 M (open circles) and 2.0 M (red circles).

Figure 2.2 demonstrates the results of ζ-potential titration of bare silica NPs in aqueous solutions containing 0.05 M, 0.50 M and 2.0 M of NaCl. Data indicate a good agreement with the literature[37,65]: at [NaCl]= 0.05 M the low-pH side of the ζ-potential titration curve reaches the apparent plateau at approximately pH≈5 where potential equals ζ ≈–5 mV. Note that after reaching this plateau ζ-potential keeps going up as pH is decreasing. We believe that this is a result of protonation of a small fraction (~15%) of silanols with pK_a≈4.5.[24] At pH≈2.5 all these silanols seem to be protonated and the silica surface becomes electrically neutral (ζ≈0 mV) (Fig. 2.1, filled circles). This small potential change Δζ≈5 mV corresponds to only ≈11% of a total ζ-potential change during the titration. As we have already mentioned, the IMTSL, when attached to SH group of a thiol, covers the titration range of pH≈1.33÷5.33. This pH range is partially (~70 %)

overlapped with the pH range of pH≈2.50÷6.50 where silanol groups with acidic pK_a≈4.5 are ionized. Silanol groups in the overlapped area constitute only ~10 % of the total amount of the ionizable silanol groups. At [NaCl]=0.50 M the plateau was reached at pH≈4.5. At [NaCl]=1.0 M and [NaCl]=2.0 M the silica surface charges were found to be fully screened and ζ-potentials do not change with pH but only show fluctuations around ζ=0 (Fig. 2.2, data are shown for [NaCl]=2.0 M only). Overall, in our experiments the NP surface was found to be fully screened at [NaCl]≥1.0 M. Thus, based on our experimental ζ-potential measurements and the literature data,[20,36] the silica isoelectric points were assumed to be pH=2.5 for [NaCl]=0.05 M, pH=4.0 for [NaCl]=0.2 M and 0.3 M, and pH=4.5 for [NaCl]=0.5 M. As our previous experiments showed no measurable difference in ζ-potentials of bare and ligand-modified SiNPs,[64] the same zero-charge points were assumed for both modified and bare NPs. It is worth of noting that ζ-potential at [NaCl]=0.05 M is as twice as higher than that at [NaCl]=0.5 M (-43 mV vs. -19 mV; filled circles *vs*. open circles, Fig. 2.2).

2.3.3. *EPR Titrations of Spin labeled Silica Nanoparticles*

Figure 2.3 shows the X-band EPR spectra of IKMTSL-labeled SiNPs acquired at essentially the same pH≈2.9 and various NaCl concentrations ([NaCl]=0.05 M, 0.5 M, and 2.0 M, respectively). As it can be seen, the spectra are essentially identical. This observation indicates that the spectral changes that will be discussed below were not produced by the effect of the solution ionic strength but are solely the results of changes in the ionization (protonation) state of a nitroxide.

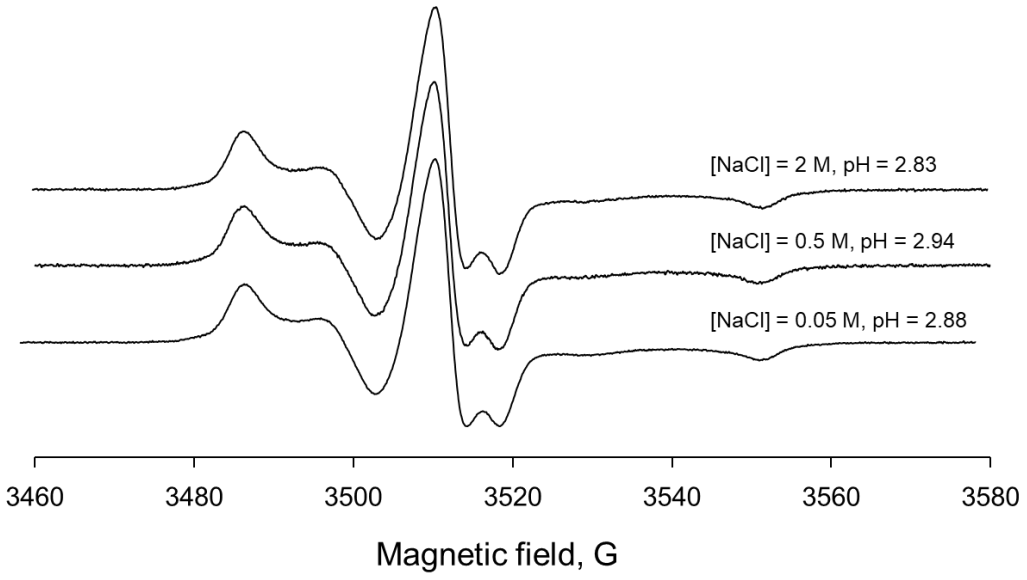

Figure 2.3. X-band EPR spectra of IKMTSL-labeled silica acquired at essentially the same pH but various NaCl concentrations. Spectra were taken at 21 °C.

Let us consider an isolated ionizable nitroxide at a water-silica interface. The observed $p\mathrm{K}_\mathrm{a}^{\mathrm{obs}}$ of such a nitroxide could be represented as a sum of several terms:

$$p\mathrm{K}_\mathrm{a}^{\mathrm{obs}} = p\mathrm{K}_\mathrm{a}^{\mathrm{w}} + \Delta p\mathrm{K}_\mathrm{a}^{\mathrm{el}} + \Delta p\mathrm{K}_\mathrm{a}^{\mathrm{pol}} \tag{2.2}$$

where $p\mathrm{K}_\mathrm{a}^{\mathrm{w}}$ is an intrinsic $p\mathrm{K}_\mathrm{a}$ of a nitroxide; $\Delta p\mathrm{K}_\mathrm{a}^{\mathrm{el}}$ is a contribution of non-zero surface electrostatic potential; $\Delta p\mathrm{K}_\mathrm{a}^{\mathrm{pol}}$ is a local polarity contribution, attributed to changes in relative permittivity of the surrounding environment.

To determine the intrinsic $p\mathrm{K}_\mathrm{a}^{\mathrm{w}}$ of the nitroxides attached to the nanoparticle-coating ligands, we pH-titrated the adducts formed by the corresponding spin labels and 2-mercaptoethanol – IMTSL-ME and IKMTSL-ME – in solutions with various NaCl concentrations. These adducts, as we have demonstrated before, model the properties of the spin labeled thiol ligands rather well.[67]

As we have mentioned earlier (see above), in the pH range pH≈1.33÷5.33 silica surface is weakly negatively charged, so the shift in the $p\mathrm{K}_\mathrm{a}$ of the nitroxide in IMTSL-SiNPs with respect

to the bulk aqueous solution represents the sum of both electrostatic ($\Delta p\mathrm{K}_\mathrm{a}^{el}$) and polarity ($\Delta p\mathrm{K}_\mathrm{a}^{\mathrm{pol}}$) effects. To test whether this $p\mathrm{K}_\mathrm{a}$ shift is affected by the solution ionic strength, we titrated IMTSL-labeled SiNPs in solutions containing 0.05 and 2.0 M NaCl and compared the titration data with that of IMTSL-ME titrated in the same conditions (Figure 2.5 and Table 2.1). The titration data for IMTSL-ME with [NaCl]=0.05 M were taken from the previous report.[59] Titration of IMTSL-ME with [NaCl]=2.0 M required the pH correction for solution ionic strength[68,69] (see Experimental part for details). The results of titration are shown in Table 2.1 and Figure 2.5. As it can be seen, the $p\mathrm{K}_\mathrm{a}^\mathrm{w}$ of IMTSL-ME increases from $p\mathrm{K}_\mathrm{a}^\mathrm{w}$=3.33±0.03 to $p\mathrm{K}_\mathrm{a}^\mathrm{w}$=3.96±0.03 ($\Delta p\mathrm{K}_\mathrm{a}$ =0.63±0.04) when [NaCl] changes from 0.05 M to 2.0 M. A similar effect was previously reported by us for pH-sensitive nitroxide 2,2,3,4,5,5-hexamethylimidazolidin-1-oxyl (HMI),[68] whose $p\mathrm{K}_\mathrm{a}^\mathrm{w}$ changed for ~0.8 pH units when [NaCl] changed from 0.05 M to 2.0 M. Note that the isotropic hyperfine coupling constants (A_{iso}) for both protonated and non-protonated forms of the nitroxide did not change (0.05 M, $A_{iso}R^{\bullet}$ = 15.86 ± 0.01 G, $A_{iso}R^{\bullet}H^{+}$ = 14.58 ± 0.01 G; 2.0 M, $A_{iso}R^{\bullet}$ = 15.86 ± 0.01 G, $A_{iso}R^{\bullet}H^{+}$ = 14.60 ± 0.01 G). It is well known that isotropic nitrogen hyperfine coupling constant (A_{iso}) is dependent on the solvent polarity.[70] In our previous experiments we have found that magnitude of the A_{iso} of a nitroxide was not affected by the change in the solution ionic strength.[67] Our observation seems to be contradicting with the literature data demonstrating that ε decreases with salt concentration.[71] A rationale for this effect is that in the presence of ions, the water dipoles will align along the electric field created by ions, rather than the external electric field. As a result, the contribution of water molecules in the ion solvation shell to the dielectric response will be significantly diminished.[72–74] However, such reorientation of water molecule dipoles seems does not change the extent of stabilization of the polar canonical form B of the

nitroxide, which determines the effective spin density on the nitrogen atom and, consequently, the nitrogen hyperfine coupling constant, A_{iso}.

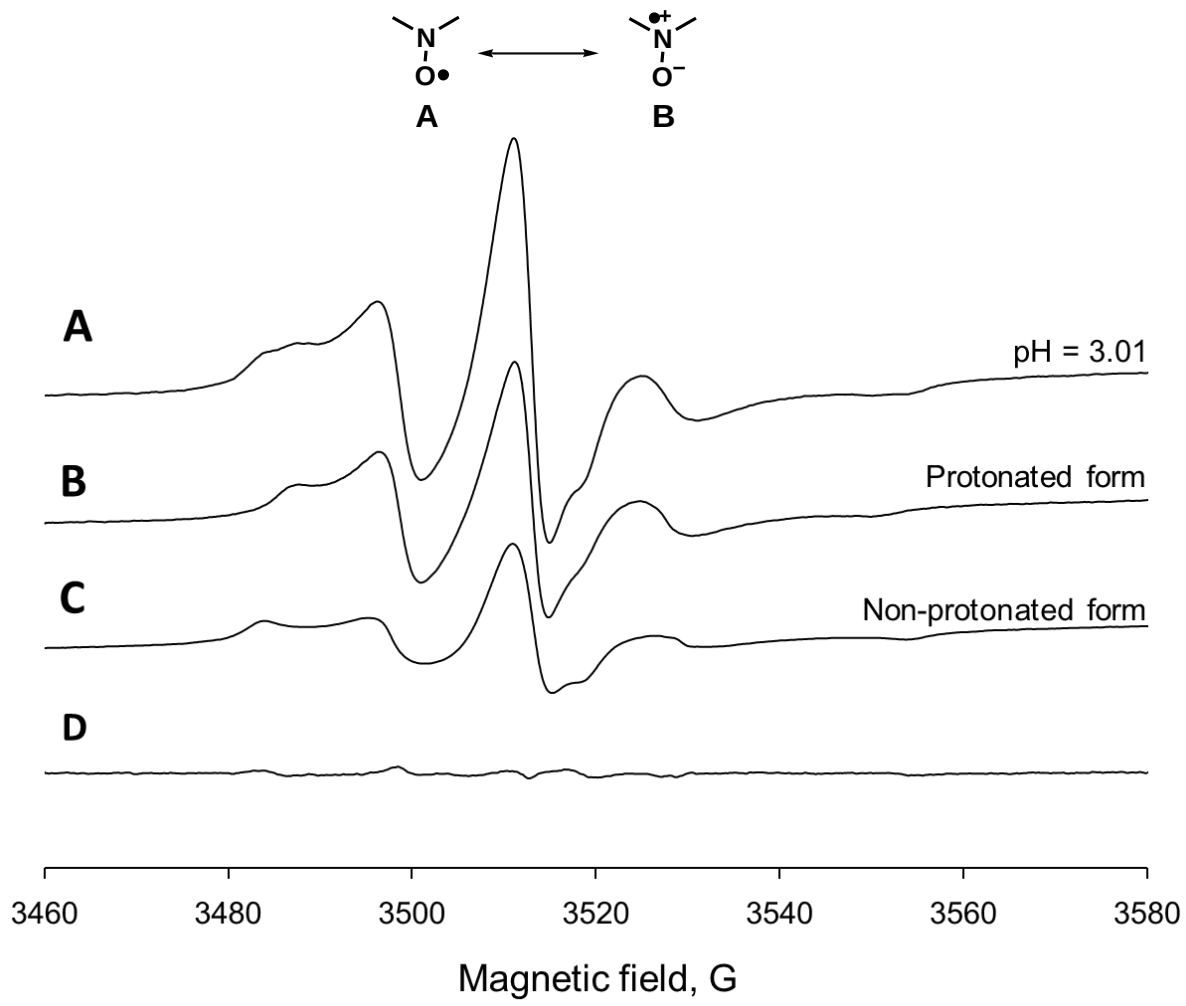

Figure 2.4. Representative experimental slow-motion X-band (9.5 GHz) EPR spectrum of the IMTSL-labeled SiNPs acquired at intermediate pH and its least-squares decomposition for the individual components corresponding to the protonated and non-protonated forms of the nitroxide. (A) Spectrum of IMTSL-SiNPs taken at pH=3.01. (B) and (C) spectral components corresponding to the protonated and non-protonated forms of the nitroxide, respectively. (D) The fit residual. Details of the spectra decomposition have been previously described by us.[75]

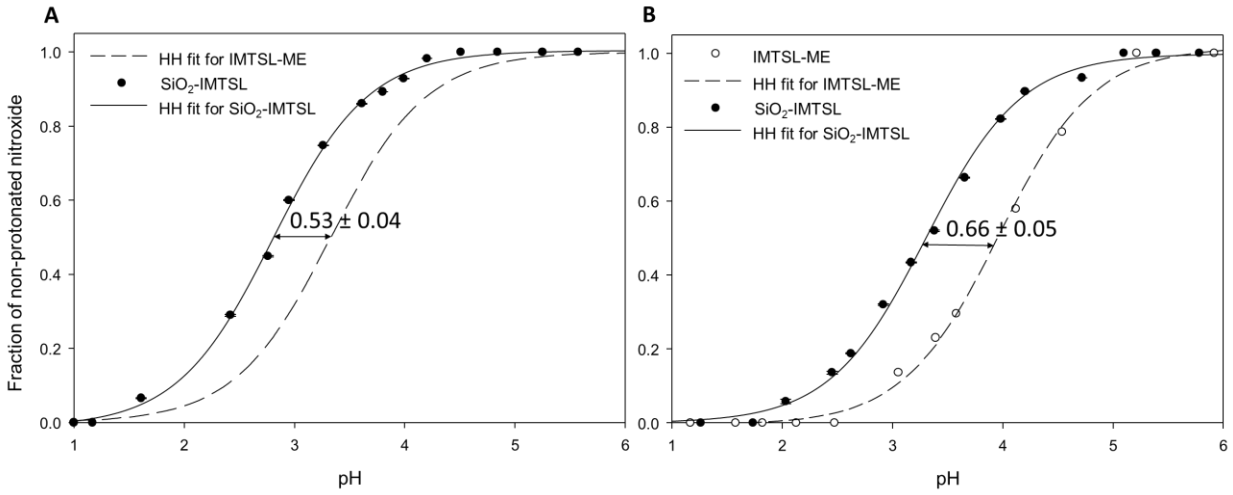

Figure 2.5. Titration of IMTSL-ME (open circles) and IMTSL-labeled SiNPs (filed circles) in aqueous solutions containing (A) 0.05 M NaCl and (B) 2.0 M NaCl. Solid and dashed lines represent the Henderson-Hasselbalch fits. Titration curve for IMTSL-ME at [NaCl]=0.05 M (panel A) was generated using Eq.2.3 and $p\mathrm{K_a}$=3.33 that was reported earlier.[59]

The three-component slow-motion EPR spectra (Fig. 2.4) obtained from pH-titration of IMTSL-SiNPs were least-squares decomposed for the individual components corresponding to the protonated and non-protonated forms of the nitroxide using the procedure previously described by us.[75] The experimentally obtained fraction of the non-protonated form of the nitroxide, *f*, was fitted into the Henderson–Hasselbalch equation:

$$f = \frac{1}{1 + 10^{p\mathrm{K_a^{obs}} - p\mathrm{H}}} \tag{2.3}$$

As it could be seen, the Henderson–Hasselbalch equation fits the experimental data for titration of IMTSL-labeled SiNPs rather well (Rsqr = 0.999 for 0.05 M and Rsqr = 0.998 for 2.0 M) (Fig. 2.5). Although both the surface electrostatics (see data of ζ-potential measurements) and interfacial polarity contribute to the titration data within this pH range, the quality of the fit indicates that the amount of the surface charges developed was insignificant to affect the shape of

the titration curve. As we have previously reported,[63] if the surface charge was gradually developed on the silica surface during the pH titration, it generated a "stretched" titration curve that we failed to fit using the Henderson–Hasselbalch equation. The results of the titration are summarized in Table 2.1.

Table 2.1. Data for titration of IMTSL-ME and IMTSL-labeled silica in aqueous solutions containing 0.05 M and 2.0 M NaCl. Dielectric constant, ε, was calculated using previously reported correlation between ε and NaCl concentration.[76]

[NaCl], M	pK_a^w, **IMTSL-ME**	**ε**	pK_a^{obs}, **SiO_2-IMTSL**	ΔpK_a^{pol}
0.05	3.33 ± 0.03	79.94 ± 0.18	2.80 ± 0.02	-0.53 ± 0.04
2.0[a]	3.77 ± 0.03	-	3.14 ± 0.02	-0.63 ± 0.04
2.0[b]	3.96 ± 0.03	58.73 ± 1.00	3.30 ± 0.02	-0.66 ± 0.04

[a]pH was experimentally measured with a pH electrode; [b]pH was corrected for a solution ionic strength.

As it was reported earlier, the increased salt concentration causes a stronger polarization and compression of Stern Layer (from approx. 1 nm at 0.01 M to 0.6 nm at 0.1 M[43,45]), and so does the region of polarized water molecules near the NP surface. We note here that the structure of water in this region closely resembles that of ice.[49,50] Thus, it is expected that when the thickness of the hydration water layer becomes thinner, the local environment of the nitroxide probe would change from ice-structured to a less ordered, resembling that of a bulk water. As we observed, when [NaCl] is changing from 0.05 to 2.0 M, the ΔpK_a^{pol} term is experiencing only minor change (≈0.13 of pH units) (Table 2.1). We also cannot rule out that this minor variation in the observed interfacial polarity could be the result of so-called "salting-out" effect.[77,78] The rationale behind this is increased cavity formation energy cost in aqueous solutions of NaCl that results in lower

solubility of nonpolar organic salutes.[78] The consequence of this effect for our experimental system is that the spin probe tethered to the silica surface is "pushed" from the "bulk" solution closer to the silica surface decorated with hydrophobic silane ligands. As a result, in 2.0 M NaCl solution the local environment of the spin probe is slightly less polar than that in 0.05 M solution.

The titration range of IKMTSL conveniently falls into the region of pH where surface of silica gradually charges, thus providing us with a unique tool for investigating ionic strength effects on the surface electrostatics and interfacial polarity. The titration data for IKMTSL-ME and IKMTSL-labeled SiNPs were obtained for aqueous solutions containing 0.05 M, 0.2 M, 0.3 M, 0.5 M, 1.0 M and 2.0 M NaCl, respectively. (Tables 2.2 and 2.3).

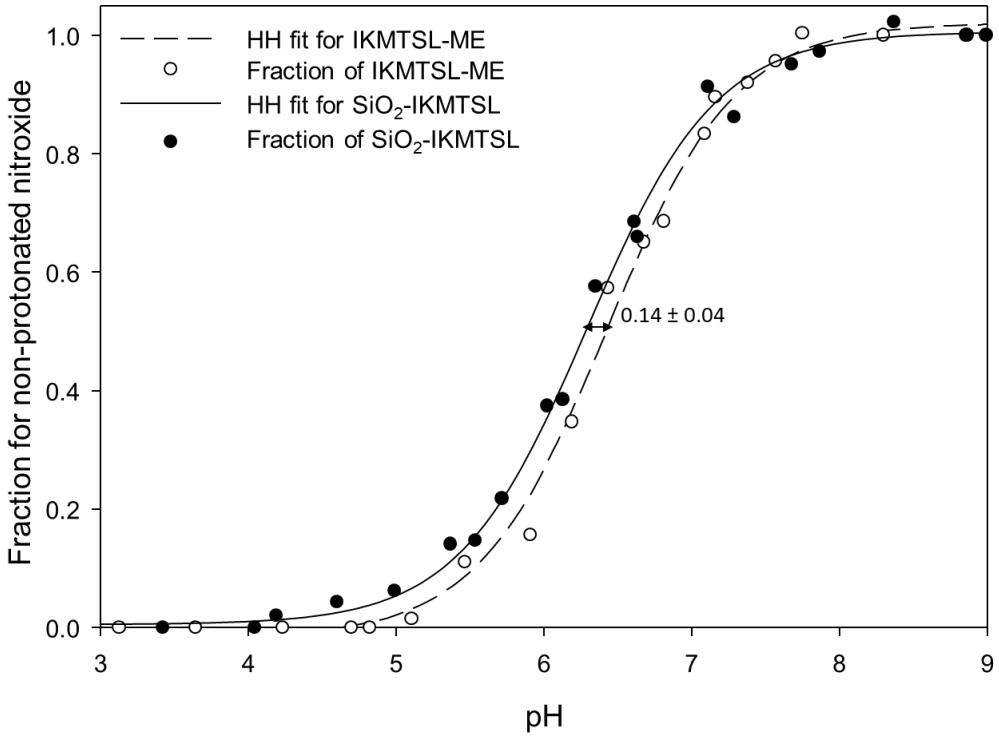

Figure 2.6. Comparison of IKMTSL-ME and SiO_2-IKMTSL titration curves acquired at 2.0 M NaCl. At this concentration surface charges of silica are completely screened, and the data are readily fit using the Henderson-Hasselbalch equation (solid and dashed lines). pH was corrected for ionic strength, see the Experimental Part.

Titration of IKMTSL-ME in aqueous solution with NaCl concentrations ranging from 0.05 to 2.0 M showed a gradual increase of $p\mathrm{K}_\mathrm{a}^\mathrm{w}$ from $p\mathrm{K}_\mathrm{a}^\mathrm{w}$ =6.01±0.04 to $p\mathrm{K}_\mathrm{a}^\mathrm{w}$=6.43±0.03 (Table 2.2). Titrations of SiO_2-IKMTSL at [NaCl]=1.0 M and [NaCl]=2.0 M showed that at these electrolyte concentrations the surface charges were fully screened, which manifested itself in a flawless fitting of the experimental data with Henderson–Hasselbalch equation (Rsqr=0.997 for both 1.0 and 2.0 M NaCl). Unlike IMTSL-ME and SiO_2-IMTSL in 2.0 M solution, a corresponding IKMTSL pair demonstrated only a moderate difference ($\Delta p\mathrm{K}_\mathrm{a}^\mathrm{pol}\approx$ 0.14 pH units) between $p\mathrm{K}_\mathrm{a}^\mathrm{w}$ and $p\mathrm{K}_\mathrm{a}^\mathrm{obs}$ (Figure 2.6 and Table 2.3). As a reminder, a corresponding IMTSL-ME and SiO_2-IMTSL pair demonstrated a more significant difference of $\Delta p\mathrm{K}_\mathrm{a}^\mathrm{pol}\approx$ 0.63 pH units (Table 2.1).

Besides the silica-water interface being less polar than bulk aqueous phase, there is another factor that makes $p\mathrm{K}_\mathrm{a}$ of the nitroxide probe attached to the surface of silica lower than that in solution. The negatively charged silica particles are surrounded by Stern layer, formed primarily by positively charged ions, whereas more mobile anions are depleted from the vicinity of the surface. This network of cations effectively destabilizes the protonated (positively charged) form of the nitroxides, thus decreasing its $p\mathrm{K}_\mathrm{a}$.

We estimated the effective dielectric constant for IKMTSL-ME in NaCl solutions, using previously reported data on the dependence of the solution dielectric constant on NaCl concentration[76] and our own data on the effect of NaCl concentration on the $p\mathrm{K}_\mathrm{a}$'s of the IKMTSL-ME (Table 2.2). The resulted $p\mathrm{K}_\mathrm{a}^\mathrm{obs}$-ε correlation plot is shown in Figure 2.7. We attempted to use this correlation plot to estimate the effective dielectric constant in the location of the spin probe in the IKMTSL-labeled SiNPs at high ionic strength, when surface electric charges were completely screened. We have found that in 1.0 M NaCl solution the spin probe in SiO_2-IKMTSL ($p\mathrm{K}_\mathrm{a}^\mathrm{obs}$=6.14±0.03) was experiencing the local dielectric environment with ε=75.20. In 2.0 M

NaCl solution ($p\mathrm{K}_\mathrm{a}^{\mathrm{obs}}$=6.29±0.02) SiO_2-IKMTSL was experiencing the local dielectric environment with ε=67.60. That means that effective dielectric constant in the location of the probe in IKMTSL-labeled SiNPs is significantly higher than that of IKMTSL-ME in NaCl solutions of the same concentration (Table 2.2). Overall, this observation is consistent with the results of ^{1}H NMR[79] and SFVS[41] studies suggesting that water-water hydrogen bonds are less stable and more prone to breaking in the presence of high NaCl concentrations[80] and that the presence of salt favors the silanol-water bonds formation, which further increases water polarization.[41] However, we cannot rule out the possibility that applying the correlation $p\mathrm{K}_\mathrm{a}^{\mathrm{obs}}$-ε obtained for homogeneous aqueous solutions to the surface-tethered nitroxide probe could be producing erroneous results. For example, according to original [NaCl]-ε correlation plot,[76] the dielectric environment with ε=75.20 that the spin probe in SiO_2-IKMTSL is experiencing in 1.0 M NaCl solution corresponds to an aqueous solution with [NaCl]≈0.39 M. For SiO_2-IKMTSL in 2.0 M NaCl solution the local dielectric environment of the probe with ε=67.60 translates, in turn, to [NaCl]≈1.03 M. Clearly, we find no physical reasons for NaCl concentration in the vicinity of silica nanoparticles being lower than in the bulk solution.

Table 2.2. Titration of IKMTSL-ME in aqueous solution with various NaCl concentrations. Dielectric constant, ε, was calculated using previously reported correlation between ε and NaCl concentration.[76]

[NaCl] M	0.05	0.2	0.3	0.5	1.0	2.0
$pK_a^{w\ a}$	6.00 ± 0.04	6.05 ± 0.04	6.07 ± 0.04	6.10 ± 0.03	6.12 ± 0.03	6.10 ± 0.04
$pK_a^{w\ b}$	6.01 ± 0.04	6.08 ± 0.04	6.11 ± 0.04	6.18 ± 0.03	6.28 ± 0.04	6.43 ± 0.03
ε	79.94 ± 0.18	77.74 ± 0.20	76.36 ± 0.22	73.78±0.28	68.03±0.48	58.73±1.00

[a]pH was experimentally measured with a pH electrode; [b]pH was corrected for a solution ionic strength.

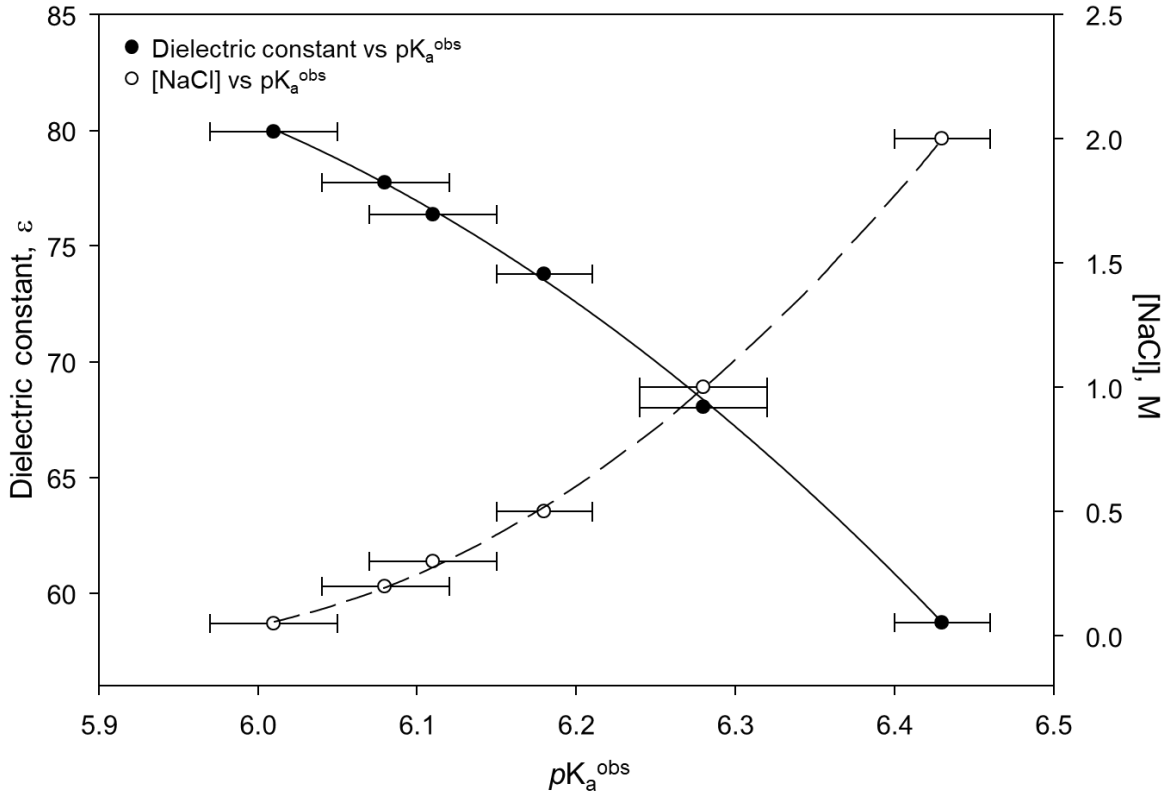

Figure 2.7. pK_a^{obs} of IKMTSL-ME shown as a function of a NaCl solution dielectric constant (ε) and NaCl concentration. Solid and dashed line represent the results of the polynomial fit, see the Appendix 2C.

Table 2.3. The results of titration of SiO_2-IKMTSL in aqueous solution with NaCl concentrations of 1.0 M and 2.0 M. The table shows the results for experimentally measured data and for the same data with the effect of ionic strength adjustment.

	Measured		Corrected	
[NaCl], M	**1.0**	**2.0**	**1.0**	**2.0**
pK_a^w, **IKMTSL-ME**	6.12 ± 0.03	6.10 ± 0.04	6.28 ± 0.04	6.43 ± 0.03
$\boldsymbol{pK_a^{obs}}$, **SiO_2-IKMTSL**	5.98 ± 0.03	5.98 ± 0.02	6.14 ± 0.03	6.29 ± 0.02
$\boldsymbol{\Delta pK_a^{pol}}$	-0.14 ± 0.04	-0.12 ± 0.04	-0.14 ± 0.05	-0.14 ± 0.04

As it can be seen from Table 2.2, the ionic strength has a weaker effect on the pK_a^w of IKMTSL-ME compared to that observed for IMTSL-ME (Table 2.1). Thus, when [NaCl] increased from 0.05 M to 2.0 M, pK_a^w of IKMTSL-ME changed for only $\Delta pK_a^w \approx 0.4$ pH units *vs.* $\Delta pK_a^w \approx 0.63$ pH units for IMTSL-ME. We believe that the reason for that lies in the structure of this nitroxide. As we suggested before,[68] the effect of the solution ionic strength on the equilibrium that involves charged species (e.g., reversible protonation of pH-sensitive nitroxide) originates from the electrostatic interactions between the positively charged protonated form of the nitroxide ($R^{\bullet}–H^+$) and the counter ions (Cl^-). An increase in Cl^- concentration stabilizes the protonated form ($R^{\bullet}–H^+$) of the nitroxide and shifts the protonation equilibrium towards higher pK_a values. The effectiveness of this ionic stabilization will depend on the properties of the charged species. For species carrying a localized charge, such stabilization is expected to be very effective. For species with a delocalized charge the ionic stabilization is expected to be less effective because the energy of the system is already lowered by the charge delocalization.[80] For example, in the protonated imidazolidine derivative IMTSL-ME (Fig. 2.1) the positive charge is localized at the nitrogen atom

in the 3rd position of the heterocycle, and, as a result, a significant shift of its $p\mathrm{K_a}$ (≈0.63 units of pH) is observed when [NaCl] increases from 0.05 M to 2.0 M. We observed even large $p\mathrm{K_a}$ shift (~0.8 units of pH) for HMI nitroxide when [NaCl] increased from 0.05 M to 2.0 M.[68] In the protonated IKMTSL-ME the positive charge is delocalized over the amidine functionality, so the interaction with anionic species does not result in further stabilization and we observe a much lower (~0.4 pH unit) $p\mathrm{K_a}$ shift.

At [NaCl] in the range 0.05 M÷0.5 M the surface charges are only partially screened, therefore, the surface electrostatic potential directly affects the $p\mathrm{K_a}$ of the attached nitroxide. For an isolated nitroxide attached to silica surface, the $p\mathrm{K_a^{obs}}$ is described by Equation 2.2. $\Delta p\mathrm{K_a^{el}}$ and surface electrostatic potential are related as:

$$\Delta p\mathrm{K_a^{el}} = \frac{-e\Psi}{ln(10)kT} \tag{2.4}$$

where *e* is the elementary charge, *k* is the Boltzmann constant.

Fraction of the non-protonated form of the nitroxide could be determined using the Equation 2.3. Then the equation that links surface electrostatic potential, pH, intrinsic $p\mathrm{K_a^w}$ and polarity contribution, $\Delta\mathrm{pK_a^{pol}}$, could be derived as follows:

$$\Psi = \frac{-\ln(10)\,kT}{\mathrm{e}}\left(log_{10}\left(\frac{1}{f}-1\right) + p\mathrm{H} - p\mathrm{K_a^w} - \Delta p\mathrm{K_a^{pol}}\right) \tag{2.5}$$

For an accurate calculation of the surface electrostatic potential, a proper reference for $\Delta p\mathrm{K_a^{pol}}$ has to be established. This could be done by using (*i*) the $p\mathrm{K_a}$ shift observed for fully screened SiO_2-IKMTSL ([NaCl]=2.0 M, $\Delta p\mathrm{K_a^{el}}$=0) (Figure 2.8), or (*ii*) the literature data[66] on silica isoelectric point confirmed by our own results of ζ-potential measurements (Figure 2.9).

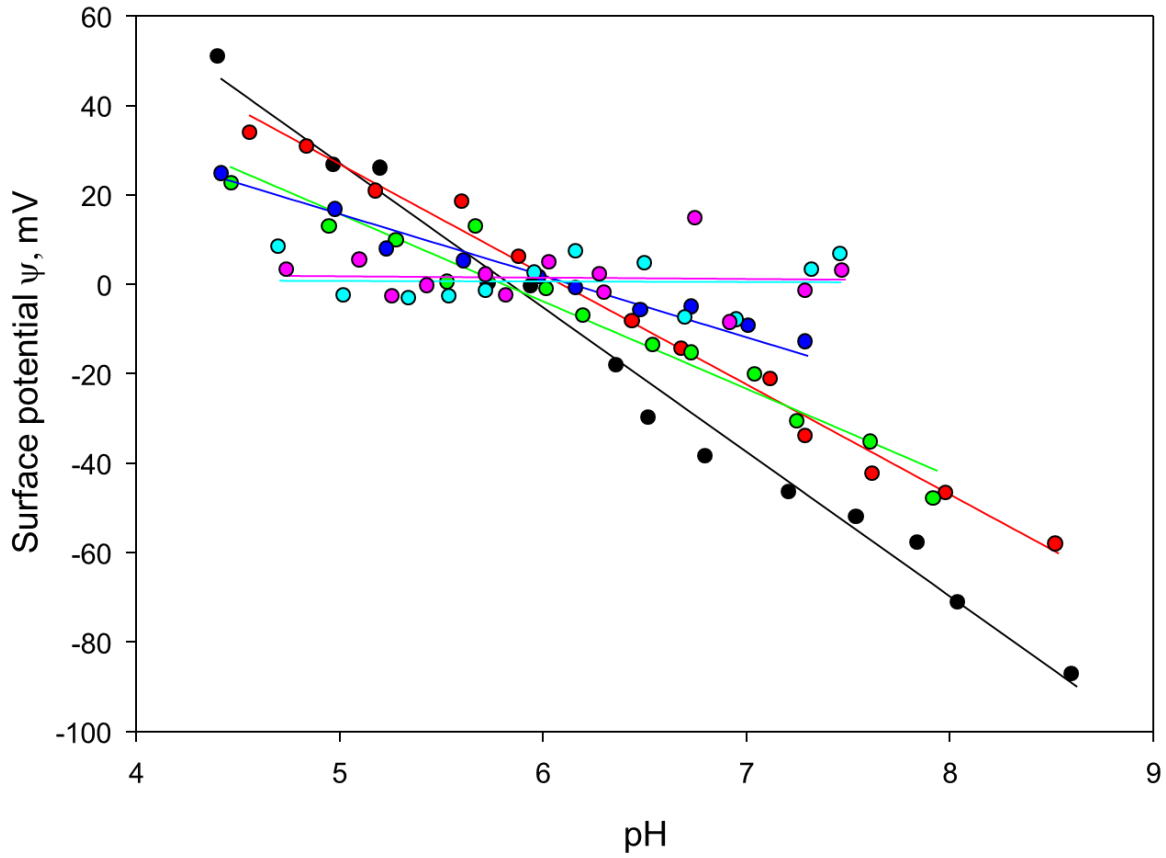

Figure 2.8. Surface potentials calculated based on the results of SiO_2-IKMTSL EPR titration in 2.0 M NaCl solution (ΔpK_a^{el}=0, ΔpK_a^{pol}= -0.14; see Table 2.3). The solid lines represent the results of the liner fit.

As we can see from Fig. 2.8, ΔpK_a^{pol} obtained from a single experiment is not reliable for using as a reference, because the polarity contribution changes with the ionic strength. We believe that to account for the dependence on the NaCl concentration, using the data on isoelectric point (pI) obtained from ζ-potential titration would be more accurate.

As we have already shown, the isoelectric point for silica NP depends on the salt concentrations. Thus, for the range of [NaCl] used in this work the following isoelectric points were chosen: pI = 2.5 for 0.05 M, pI = 4.0 for 0.2 M and 0.3 M, and pI = 4.5 for 0.5 M. We adjusted

ΔpK_a^{pol} parameter in the Equation 2.5 so the surface potentials for all the samples to be ζ=0 at pH=pI (Figure 2.9). The results of the linear fits of the experimental data into modified Eq. 2.5 are given in Table 2.4, and the calculated ΔpK_a^{pol} shifts are given in Table 2.5.

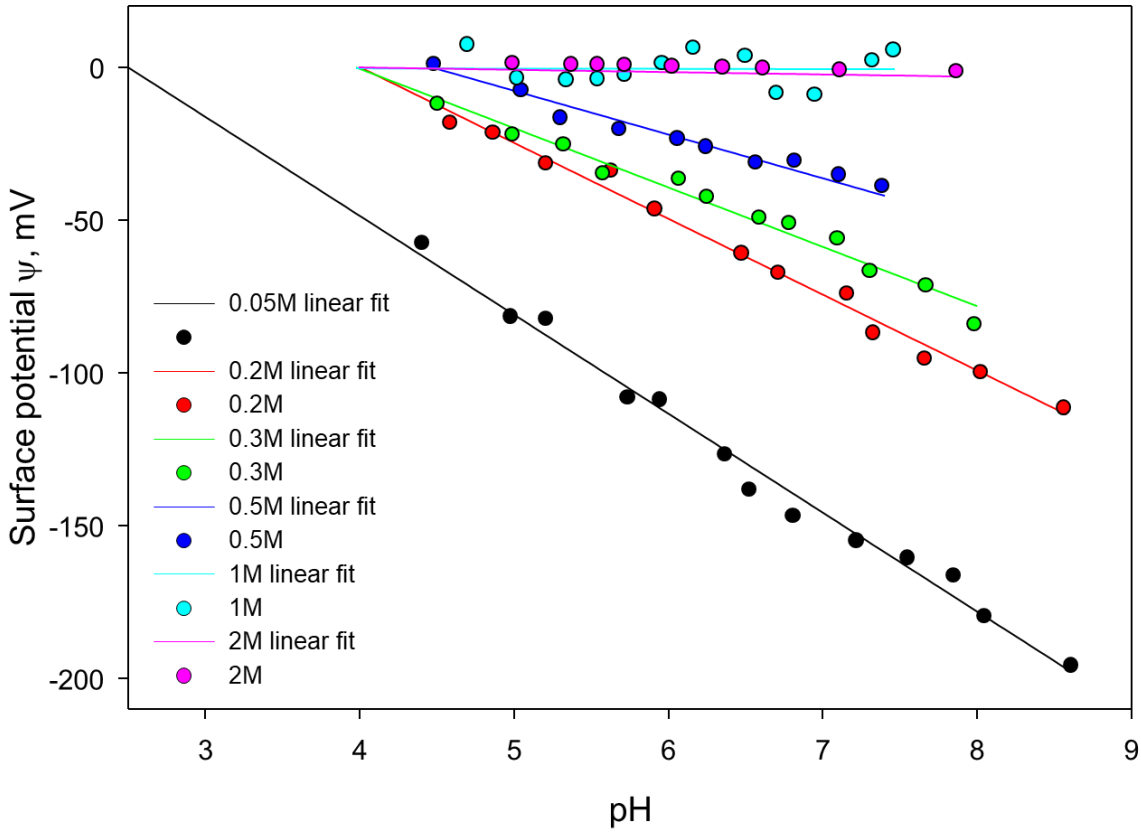

Figure 2.9. Electrostatic surface potentials calculated based on the assumption that at the isoelectric points ψ≈0. The following data for isoelectric points were used: pI = 2.5 for 0.05 M, pI = 4.0 for 0.2 M and 0.3 M, and pI = 4.5 for 0.5 M. Solid lines represent the results of linear fits. [NaCl]: 0.05 M (black), 0.2 M (red), 0.3 M (green), 0.5 (blue), 1 M (cyan), and 2 M (pink). The results of the linear fits are summarized in Table 2.4.

Table 2.4. Results of linear fits of surface potential data titration data for silica modified with IKMTSL (Figure 2.9). The isoelectric points used for calibrations are pI = 2.5 for 0.05 M, pI = 4.0 for 0.2 M and 0.3 M, and pI = 4.5 for 0.5 M.

[NaCl], M	ψ, mV	Rsqr
0.05	(80.91 ± 2.60) - (32.37 ± 0.41)pH	0.988
0.2	(98.97 ± 2.05) - (24.78 ± 0.34)pH	0.989
0.3	(76.92 ± 2.09) - (19.38 ± 0.33)pH	0.976
0.5	(64.08 ± 2.09) - (14.35 ± 0.34)pH	0.923

Using these fit results, the surface potentials at the locations of the nitroxide probe could be readily determined. For example, the samples with fully screened surfaces charges at [NaCl]= 1.0 M and 2.0 M show zero surface potentials throughout the whole titration region. As it could be seen from Table 2.5, the $p\mathrm{K_a}$ shift gradually decreases with [NaCl], suggesting that nitroxide local environment is highly dependent on the salt concentration.

Table 2.5. $\Delta p\mathrm{K_a^{pol}}$ shifts obtained based on the following isoelectric points: pI = 2.5 for 0.05 M, pI= 4.0 for 0.2 M and 0.3 M, and pI = 4.5 for 0.5 M.

[NaCl], M	0.05	0.2	0.3	0.5	1.0	2.0
$\boldsymbol{\Delta p\mathrm{K_a^{pol}}}$	-1.98	-1.02	-0.72	-0.55	-0.30	-0.23

Note that for 1.0 M and 2.0 M samples, the obtained $\Delta p\mathrm{K_a^{pol}}$ shifts are slightly different from what was determined from comparison of IKMTSL-ME and SiO_2-IKMTSL titration data (Table 2.3): the polarity shift was found to be $\Delta p\mathrm{K_a^{pol}}$= -0.14 ± 0.04 for both [NaCl]=1.0 M and 2.0 M. The difference, however, is not significant and can be attributed to an inaccuracy of magnitude of pI chosen for calculation. The fact that $\Delta\mathrm{pK_a^{pol}}$ of SiO_2-IKMTSL noticeably differ

from that of fully screened probe in SiO_2-IMTSL (Table 2.1, [NaCl] = 2.0 M) suggests that the locations of these probes relative to the silica surface are different.

2.4. Conclusions

Electrostatic and dielectric properties of silica nanoparticles in a wide range of salt concentrations ([NaCl] = 0.05 M ÷ 2.0 M) were studied by means of spin labeling EPR. Two pH-sensitive thiol-specific nitroxide probes – IMTSL and IKMTSL – were used to target pH regions where acidic (pK$_a$≈4.5) and basic (pK$_a$ ≈8.5) silanols undergo ionization. To determine the intrinsic $p\mathrm{K}_\mathrm{a}^\mathrm{w}$ of these probes attached to SH group of a thiol, we pH titrated adducts formed by IMTSL and IKMTSL with 2-mercaptoethanol. The titration pH region of the first adduct, IMTSL-ME ($p\mathrm{K}_\mathrm{a}^\mathrm{w}$=3.33), covers the acidic area; silanols in this group constitute ~15% of total silanol population. The titration range of the second adduct, IKMTSL-ME, ($p\mathrm{K}_\mathrm{a}^\mathrm{w}$=5.98) allows to target the pH range where silica nanoparticles develop a significant charge due to ionization of silanols of both types. To take into account the effect of ionic strength on the pH measured by glass electrode, a correction model was developed and applied to all pH measurements.

Ionic strength was found to have a strong effect on the pK$_a$ of the nitroxide probes. Thus, $p\mathrm{K}_\mathrm{a}^\mathrm{w}$ of IMTSL-ME changed from 3.33±0.03 to 3.96±0.03 when [NaCl] increased from 0.05 M to 2.0 M. In the same NaCl concentration range, $p\mathrm{K}_\mathrm{a}^\mathrm{w}$ of IKMTSL-ME changed from 6.01±0.04 to 6.43±0.03. Upon this ionic strength change, pK$_a$ of the spin labeled silica nanoparticles, SiO_2-IMTSL, changed from 2.80±0.02 to 3.30±0.02.

According to ζ-potential titration, in 2.0 M NaCl solution the surface charges are fully screened, therefore the pK_a shift is attributed to the polarity effect. Thus, for SiO_2-IMTSL $\Delta p\mathrm{K}_\mathrm{a}^\mathrm{pol}$ was found to be $\Delta p\mathrm{K}_\mathrm{a}^\mathrm{pol}$= - 0.66±0.04, whereas for SiO_2-IKMTSL $\Delta p\mathrm{K}_\mathrm{a}^\mathrm{pol}$= -0.14 ± 0.04.

At NaCl concentrations in the range from 0.05 M to 0.5 M the electric charges on the surface of silica are not screened, and we analyzed the surface electrostatic potentials as a function of pH. Surface potential at the location of the reporter group of the nitroxide was found to grow linearly with pH. Due to the partial screening of the SiNP's surface, the slopes are decreasing while NaCl concentration is increasing. The polarity term ($\Delta p\mathrm{K}_\mathrm{a}^{\mathrm{pol}}$) was found to inversely correlate with [NaCl].

Using the literature data on the dependence of dielectric constant, ε, on the NaCl concentration, and our own data on the dependence of $p\mathrm{K}_\mathrm{a}^{\mathrm{obs}}$of IKMTSL-ME on the NaCl concentration, a $p\mathrm{K}_\mathrm{a}^{\mathrm{obs}}$-ε correlation plot was generated. We applied this correlation to estimate the dielectric constant in the location of the surface-tethered nitroxide. We have found that in 1.0 M NaCl solution the spin probe in SiO_2-IKMTSL ($p\mathrm{K}_\mathrm{a}^{\mathrm{obs}}$=6.14±0.03) was experiencing the local dielectric environment with ε=75.20. In 2.0 M NaCl solution, SiO_2-IKMTSL ($p\mathrm{K}_\mathrm{a}^{\mathrm{obs}}$=6.29±0.02) was experiencing the local dielectric environment with ε=67.60. That means, that the environment of the probe attached to silica is more polar than that of the free probe in NaCl solution of the same concentration.

To conclude, the results of this spin probe EPR studies demonstrate that the ionic strength of a solution dramatically impacts both electrostatic and dielectric properties of water-silica interface.

References

(1) Caltagirone, C.; Bettoschi, A.; Garau, A.; Montis, R. Silica-Based Nanoparticles: A Versatile Tool for the Development of Efficient Imaging Agents. *Chem. Soc. Rev.* **2015**, *44* (14), 4645–4671. https://doi.org/10.1039/C4CS00270A.

(2) Slowing, I. I.; Trewyn, B. G.; Giri, S.; Lin, V. S.-Y. Mesoporous Silica Nanoparticles for Drug Delivery and Biosensing Applications. *Adv. Funct. Mater.* **2007**, *17* (8), 1225–1236. https://doi.org/https://doi.org/10.1002/adfm.200601191.

(3) Wang, X.-D.; Rabe, K. S.; Ahmed, I.; Niemeyer, C. M. Multifunctional Silica Nanoparticles for Covalent Immobilization of Highly Sensitive Proteins. *Adv. Mater.* **2015**, *27* (48), 7945–7950. https://doi.org/https://doi.org/10.1002/adma.201503935.

(4) Falipou, S.; Chovelon, J.-M.; Martelet, C.; Margonari, J.; Cathignol, D. New Use of Cyanosilane Coupling Agent for Direct Binding of Antibodies to Silica Supports. Physicochemical Characterization of Molecularly Bioengineered Layers. *Bioconjug. Chem.* **1999**, *10* (3), 346–353. https://doi.org/10.1021/bc9800421.

(5) Song, Y.; Li, Y.; Xu, Q.; Liu, Z. Mesoporous Silica Nanoparticles for Stimuli-Responsive Controlled Drug Delivery: Advances, Challenges, and Outlook. *Int. J. Nanomedicine* **2016**, *12*, 87–110. https://doi.org/10.2147/IJN.S117495.

(6) Durfee, P. N.; Lin, Y.-S.; Dunphy, D. R.; Muñiz, A. J.; Butler, K. S.; Humphrey, K. R.; Lokke, A. J.; Agola, J. O.; Chou, S. S.; Chen, I.-M.; Wharton, W.; Townson, J. L.; Willman, C. L.; Brinker, C. J. Mesoporous Silica Nanoparticle-Supported Lipid Bilayers (Protocells) for Active Targeting and Delivery to Individual Leukemia Cells. *ACS Nano* **2016**, *10* (9), 8325–8345. https://doi.org/10.1021/acsnano.6b02819.

(7) Acharya, B.; Chestnut, M.; Marek, A.; Smirnov, A. I.; Krim, J. A Combined QCM and AFM Study Exploring the Nanoscale Lubrication Mechanism of Silica Nanoparticles in Aqueous Suspension. *Tribol. Lett.* **2017**, *65* (3), 115. https://doi.org/10.1007/s11249-017-0898-5.

(8) Banerjee, S.; Das, J.; Alvarez, R. P.; Santra, S. Silica Nanoparticles as a Reusable Catalyst: A Straightforward Route for the Synthesis of Thioethers, Thioesters, Vinyl Thioethers and Thio-Michael Adducts under Neutral Reaction Conditions. *New J. Chem.* **2010**, *34* (2), 302–306. https://doi.org/10.1039/B9NJ00399A.

(9) Siddiqui, M. H.; Al-Whaibi, M. H. Role of Nano-SiO2 in Germination of Tomato (Lycopersicum Esculentum Seeds Mill.). *Saudi J. Biol. Sci.* **2014**, *21* (1), 13–17. https://doi.org/10.1016/j.sjbs.2013.04.005.

(10) Ziaee, M.; Ganji, Z. Insecticidal Efficacy of Silica Nanoparticles against Rhyzopertha Dominica F. and Tribolium Confusum Jacquelin Du Val. *J. Plant Prot. Res.* **2016**, *56* (3), 250–256. https://doi.org/10.1515/jppr-2016-0037.

(11) Li, Z.-Z.; Chen, J.-F.; Liu, F.; Liu, A.-Q.; Wang, Q.; Sun, H.-Y.; Wen, L.-X. Study of UV-Shielding Properties of Novel Porous Hollow Silica Nanoparticle Carriers for Avermectin. *Pest Manag. Sci.* **2007**, *63* (3), 241–246. https://doi.org/10.1002/ps.1301.

(12) Carcouët, C. C. M. C.; Van De Put, M. W. P.; Mezari, B.; Magusin, P. C. M. M.; Laven, J.; Bomans, P. H. H.; Friedrich, H.; Esteves, A. C. C.; Sommerdijk, N. A. J. M.; Van Benthem, R. A. T. M.; De With, G. Nucleation and Growth of Monodisperse Silica Nanoparticles. *Nano Lett.* **2014**, *14* (3), 1433–1438. https://doi.org/10.1021/nl404550d.

(13) Van Blaaderen, A.; Van Geest, J.; Vrij, A. Monodisperse Colloidal Silica Spheres from Tetraalkoxysilanes: Particle Formation and Growth Mechanism. *J. Colloid Interface Sci.* **1992**, *154* (2), 481–501. https://doi.org/10.1016/0021-9797(92)90163-G.

(14) Hartlen, K. D.; Athanasopoulos, A. P. T.; Kitaev, V. Facile Preparation of Highly Monodisperse Small Silica Spheres (15 to >200 Nm) Suitable for Colloidal Templating and Formation of Ordered Arrays. *Langmuir* **2008**, *24* (5), 1714–1720. https://doi.org/10.1021/la7025285.

(15) Depasse, J.; Watillon, A. The Stability of Amorphous Colloidal Silica. *J. Colloid Interface Sci.* **1970**, *33* (3), 430–438. https://doi.org/https://doi.org/10.1016/0021-9797(70)90235-3.

(16) Kobayashi, M.; Skarba, M.; Galletto, P.; Cakara, D.; Borkovec, M. Effects of Heat Treatment on the Aggregation and Charging of Stöber-Type Silica. *J. Colloid Interface Sci.* **2005**, *292* (1), 139–147. https://doi.org/https://doi.org/10.1016/j.jcis.2005.05.093.

(17) Graf, C.; Gao, Q.; Schütz, I.; Noufele, C. N.; Ruan, W.; Posselt, U.; Korotianskiy, E.; Nordmeyer, D.; Rancan, F.; Hadam, S.; Vogt, A.; Lademann, J.; Haucke, V.; Rühl, E. Surface Functionalization of Silica Nanoparticles Supports Colloidal Stability in Physiological Media and Facilitates Internalization in Cells. *Langmuir* **2012**, *28* (20), 7598–7613. https://doi.org/10.1021/la204913t.

(18) Claesson, E. M.; Philipse, A. P. Monodisperse Magnetizable Composite Silica Spheres with Tunable Dipolar Interactions. *Langmuir* **2005**, *21* (21), 9412–9419. https://doi.org/10.1021/la051127a.

(19) Stöber, W.; Fink, A.; Bohn, E. Controlled Growth of Monodisperse Silica Spheres in the Micron Size Range. *J. Colloid Interface Sci.* **1968**, *26* (1), 62–69. https://doi.org/https://doi.org/10.1016/0021-9797(68)90272-5.

(20) Metin, C. O.; Lake, L. W.; Miranda, C. R.; Nguyen, Q. P. Stability of Aqueous Silica Nanoparticle Dispersions. *J. Nanoparticle Res.* **2011**, *13* (2), 839–850. https://doi.org/10.1007/s11051-010-0085-1.

(21) Yokoi, T.; Wakabayashi, J.; Otsuka, Y.; Fan, W.; Iwama, M.; Watanabe, R.; Aramaki, K.; Shimojima, A.; Tatsumi, T.; Okubo, T. Mechanism of Formation of Uniform-Sized Silica Nanospheres Catalyzed by Basic Amino Acids. *Chem. Mater.* **2009**, *21* (15), 3719–3729. https://doi.org/10.1021/cm900993b.

(22) Zhuravlev, L. T. The Surface Chemistry of Amorphous Silica. Zhuravlev Model. *Colloids Surfaces A Physicochem. Eng. Asp.* **2000**, *173* (1–3), 1–38. https://doi.org/10.1016/S0927-7757(00)00556-2.

(23) Mueller, R.; Kammler, H. K.; Wegner, K.; Pratsinis, S. E. OH Surface Density of SiO2 and TiO2 by Thermogravimetric Analysis. *Langmuir* **2003**, *19* (1), 160–165. https://doi.org/10.1021/la025785w.

(24) Ong, S.; Zhao, X.; Eisenthal, K. B. Polarization of Water Molecules at a Charged Interface: Second Harmonic Studies of the Silica/Water Interface. *Chem. Phys. Lett.* **1992**, *191* (3), 327–335. https://doi.org/https://doi.org/10.1016/0009-2614(92)85309-X.

(25) Metin, C. O.; Bonnecaze, R. T.; Lake, L. W.; Miranda, C. R.; Nguyen, Q. P. Aggregation Kinetics and Shear Rheology of Aqueous Silica Suspensions. *Appl. Nanosci.* **2014**, *4* (2), 169–178. https://doi.org/10.1007/s13204-012-0185-6.

(26) Lundqvist, M.; Stigler, J.; Elia, G.; Lynch, I.; Cedervall, T.; Dawson, K. A. Nanoparticle Size and Surface Properties Determine the Protein Corona with Possible Implications for Biological Impacts. *Proc. Natl. Acad. Sci.* **2008**, *105* (38), 14265 LP – 14270. https://doi.org/10.1073/pnas.0805135105.

(27) Nel, A. E.; Mädler, L.; Velegol, D.; Xia, T.; Hoek, E. M. V; Somasundaran, P.; Klaessig, F.; Castranova, V.; Thompson, M. Understanding Biophysicochemical Interactions at the Nano-Bio Interface. *Nat. Mater.* **2009**, *8* (7), 543–557. https://doi.org/10.1038/nmat2442.

(28) Ostroverkhov, V.; Waychunas, G. A.; Shen, Y. R. New Information on Water Interfacial Structure Revealed by Phase-Sensitive Surface Spectroscopy. *Phys. Rev. Lett.* **2005**, *94* (4), 46102. https://doi.org/10.1103/PhysRevLett.94.046102.

(29) Sulpizi, M.; Gaigeot, M.-P.; Sprik, M. The Silica-Water Interface: How the Silanols Determine the Surface Acidity and Modulate the Water Properties. *J. Chem. Theory Comput.* **2012**, *8* (3), 1037–1047. https://doi.org/10.1021/ct2007154.

(30) Pfeiffer-Laplaud, M.; Costa, D.; Tielens, F.; Gaigeot, M.-P.; Sulpizi, M. Bimodal Acidity at the Amorphous Silica/Water Interface. *J. Phys. Chem. C* **2015**, *119* (49), 27354–27362. https://doi.org/10.1021/acs.jpcc.5b02854.

(31) Schindler, P.; Kamber, H. R. Die Acidität von Silanolgruppen. Vorläufige Mitteillung. *Helv. Chim. Acta* **1968**, *51* (7), 1781–1786. https://doi.org/https://doi.org/10.1002/hlca.19680510738.

(32) Bandura, A. V; Kubicki, J. D.; Sofo, J. O. Periodic Density Functional Theory Study of Water Adsorption on the α-Quartz (101) Surface. *J. Phys. Chem. C* **2011**, *115* (13), 5756–5766. https://doi.org/10.1021/jp1106636.

(33) Gierada, M.; Petit, I.; Handzlik, J.; Tielens, F. Hydration in Silica Based Mesoporous Materials: A DFT Model. *Phys. Chem. Chem. Phys.* **2016**, *18* (48), 32962–32972. https://doi.org/10.1039/C6CP05460A.

(34) Gaigeot, M.-P.; Sprik, M.; Sulpizi, M. Oxide/Water Interfaces: How the Surface Chemistry Modifies Interfacial Water Properties. *J. Phys. Condens. Matter* **2012**, *24* (12), 124106. https://doi.org/10.1088/0953-8984/24/12/124106.

(35) Leung, K.; Nielsen, I. M. B.; Criscenti, L. J. Elucidating the Bimodal Acid-Base Behavior of the Water-Silica Interface from First Principles. *J. Am. Chem. Soc.* **2009**, *131* (51), 18358–18365. https://doi.org/10.1021/ja906190t.

(36) Atalay, S.; Ma, Y.; Qian, S. Analytical Model for Charge Properties of Silica Particles. *J. Colloid Interface Sci.* **2014**, *425*, 128–130. https://doi.org/https://doi.org/10.1016/j.jcis.2014.03.044.

(37) Behrens, S. H.; Grier, D. G. The Charge of Glass and Silica Surfaces. *J. Chem. Phys.* **2001**, *115* (14), 6716–6721. https://doi.org/10.1063/1.1404988.

(38) Barisik, M.; Atalay, S.; Beskok, A.; Qian, S. Size Dependent Surface Charge Properties of Silica Nanoparticles. *J. Phys. Chem. C* **2014**, *118* (4), 1836–1842. https://doi.org/10.1021/jp410536n.

(39) Delgado, A. V; González-Caballero, F.; Hunter, R. J.; Koopal, L. K.; Lyklema, J. Measurement and Interpretation of Electrokinetic Phenomena. *J. Colloid Interface Sci.* **2007**, *309* (2), 194–224. https://doi.org/10.1016/j.jcis.2006.12.075.

(40) Delgado, A. V; González-Caballero, F.; Hunter, R. J.; Koopal, L. K.; Lyklema, J. Measurement and Interpretation of Electrokinetic Phenomena (IUPAC Technical Report). *Pure Appl. Chem. 77* (10), 1753–1805. https://doi.org/https://doi.org/10.1351/pac200577101753.

(41) Schaefer, J.; Gonella, G.; Bonn, M.; Backus, E. H. G. Surface-Specific Vibrational Spectroscopy of the Water/Silica Interface: Screening and Interference. *Phys. Chem. Chem. Phys.* **2017**, *19* (25), 16875–16880. https://doi.org/10.1039/C7CP02251D.

(42) Lovering, K. A.; Bertram, A. K.; Chou, K. C. New Information on the Ion-Identity-Dependent Structure of Stern Layer Revealed by Sum Frequency Generation Vibrational Spectroscopy. *J. Phys. Chem. C* **2016**, *120* (32), 18099–18104. https://doi.org/10.1021/acs.jpcc.6b05564.

(43) Brown, M. A.; Goel, A.; Abbas, Z. Effect of Electrolyte Concentration on the Stern Layer Thickness at a Charged Interface. *Angew. Chem. Int. Ed. Engl.* **2016**, *55* (11), 3790–3794. https://doi.org/10.1002/anie.201512025.

(44) Brown, M. A.; Redondo, A. B.; Sterrer, M.; Winter, B.; Pacchioni, G.; Abbas, Z.; van Bokhoven, J. A. Measure of Surface Potential at the Aqueous-Oxide Nanoparticle Interface by XPS from a Liquid Microjet. *Nano Lett.* **2013**, *13* (11), 5403–5407. https://doi.org/10.1021/nl402957y.

(45) Brown, M. A.; Abbas, Z.; Kleibert, A.; Green, R. G.; Goel, A.; May, S.; Squires, T. M. Determination of Surface Potential and Electrical Double-Layer Structure at the Aqueous Electrolyte-Nanoparticle Interface. *Phys. Rev. X* **2016**, *6* (1), 11007. https://doi.org/10.1103/PhysRevX.6.011007.

(46) Boamah, M. D.; Ohno, P. E.; Geiger, F. M.; Eisenthal, K. B. Relative Permittivity in the Electrical Double Layer from Nonlinear Optics. *J. Chem. Phys.* **2018**, *148* (22), 222808. https://doi.org/10.1063/1.5011977.

(47) Conway, B. E.; Bockris, J. O.; Ammar, I. A. The Dielectric Constant of the Solution in the Diffuse and Helmholtz Double Layers at a Charged Interface in Aqueous Solution. *Trans. Faraday Soc.* **1951**, *47* (0), 756–766. https://doi.org/10.1039/TF9514700756.

(48) Wander, M. C. F.; Clark, A. E. Structural and Dielectric Properties of Quartz−Water Interfaces. *J. Phys. Chem. C* **2008**, *112* (50), 19986–19994. https://doi.org/10.1021/jp803642c.

(49) Kurosaki, S. The Dielectric Behavior of Sorbed Water on Silica Gel. *J. Phys. Chem.* **1954**,

58 (4), 320–324. https://doi.org/10.1021/j150514a009.

(50) Graja, F.; Triki, A.; Tabellout, M.; Gargouri, M.; Depollier, C. Dielectric Relaxations of Confined Water in Porous Silica Ceramics. *Bull. Mater. Sci.* **2017**, *40* (7), 1489–1495. https://doi.org/10.1007/s12034-017-1501-2.

(51) Ionita, P.; Caragheorgheopol, A.; Gilbert, B. C.; Chechik, V. EPR Study of a Place-Exchange Reaction on Au Nanoparticles: Two Branches of a Disulfide Molecule Do Not Adsorb Adjacent to Each Other. *J. Am. Chem. Soc.* **2002**, *124* (31), 9048–9049. https://doi.org/10.1021/ja0265456.

(52) Ionita, P.; Caragheorgheopol, A.; Gilbert, B. C.; Chechik, V. Mechanistic Study of a Place-Exchange Reaction of Au Nanoparticles with Spin-Labeled Disulfides. *Langmuir* **2004**, *20* (26), 11536–11544. https://doi.org/10.1021/la048121q.

(53) Zachary, M.; Chechik, V. Hopping of Thiolate Ligands between Au Nanoparticles Revealed by EPR Spectroscopy. *Angew. Chemie Int. Ed.* **2007**, *46* (18), 3304–3307. https://doi.org/https://doi.org/10.1002/anie.200604070.

(54) Ionita, P.; Volkov, A.; Jeschke, G.; Chechik, V. Lateral Diffusion of Thiol Ligands on the Surface of Au Nanoparticles: An Electron Paramagnetic Resonance Study. *Anal. Chem.* **2008**, *80* (1), 95–106. https://doi.org/10.1021/ac071266s.

(55) Khlestkin, V. K.; Polienko, J. F.; Voinov, M. A.; Smirnov, A. I.; Chechik, V. Interfacial Surface Properties of Thiol-Protected Gold Nanoparticles: A Molecular Probe EPR Approach. *Langmuir* **2008**, *24* (3), 609–612. https://doi.org/10.1021/la702823n.

(56) Voinov, M. A.; Ruuge, A.; Reznikov, V. A.; Grigor'ev, I. A.; Smirnov, A. I. Mapping Local Protein Electrostatics by EPR of PH-Sensitive Thiol-Specific Nitroxide. *Biochemistry* **2008**, *47* (20), 5626–5637. https://doi.org/10.1021/bi800272f.

(57) Voinov, M. A.; Smirnov, A. I. Spin Labels and Spin Probes for Measurements of Local PH and Electrostatics by EPR. In *Electron Paramagnetic Resonance: Volume 22*; The Royal Society of Chemistry, 2011; Vol. 22, pp 71–106. https://doi.org/10.1039/9781849730877-00071.

(58) Voinov, M. A.; Smirnov, A. I. Ionizable Nitroxides for Studying Local Electrostatic Properties of Lipid Bilayers and Protein Systems by EPR. *Methods Enzymol.* **2015**, *564*, 191–217. https://doi.org/10.1016/bs.mie.2015.08.007.

(59) Voinov, M. A.; Kirilyuk, I. A.; Smirnov, A. I. Spin-Labeled PH-Sensitive Phospholipids for Interfacial PKa Determination: Synthesis and Characterization in Aqueous and Micellar Solutions. *J. Phys. Chem. B* **2009**, *113* (11), 3453–3460. https://doi.org/10.1021/jp810993s.

(60) Smirnov, A. I.; Ruuge, A.; Reznikov, V. A.; Voinov, M. A.; Grigor'ev, I. A. Site-Directed Electrostatic Measurements with a Thiol-Specific PH-Sensitive Nitroxide: Differentiating Local PK and Polarity Effects by High-Field EPR. *J. Am. Chem. Soc.* **2004**, *126* (29), 8872–8873. https://doi.org/10.1021/ja048801f.

(61) Voinov, M. A.; Scheid, C. T.; Kirilyuk, I. A.; Trofimov, D. G.; Smirnov, A. I. IKMTSL-PTE, a Phospholipid-Based EPR Probe for Surface Electrostatic Potential of Biological

Interfaces at Neutral PH: Effects of Temperature and Effective Dielectric Constant of the Solvent. *J. Phys. Chem. B* **2017**, *121* (11), 2443–2453. https://doi.org/10.1021/acs.jpcb.7b00592.

(62) Kovaleva, E. G.; Molochnikov, L. S.; Venkatesan, U.; Marek, A.; Stepanova, D. P.; Kozhikhova, K. V; Mironov, M. A.; Smirnov, A. I. Acid–Base Properties of Nanoconfined Volumes of Anodic Aluminum Oxide Pores by EPR of PH-Sensitive Spin Probes. *J. Phys. Chem. C* **2016**, *120* (5), 2703–2711. https://doi.org/10.1021/acs.jpcc.5b10241.

(63) Kovaleva, E. G.; Molochnikov, L. S.; Tambasova, D.; Marek, A.; Chestnut, M.; Osipova, V. A.; Antonov, D. O.; Kirilyuk, I. A.; Smirnov, A. I. Electrostatic Properties of Inner Nanopore Surfaces of Anodic Aluminum Oxide Membranes upon High Temperature Annealing Revealed by EPR of PH-Sensitive Spin Probes and Labels. *J. Memb. Sci.* **2020**, *604*, 118084. https://doi.org/https://doi.org/10.1016/j.memsci.2020.118084.

(64) Perelygin, V.; Voinov, M. A.; Marek, A.; Ou, E.; Krim, J.; Brenner, D.; Smirnova, T. I.; Smirnov, A. I. Dielectric and Electrostatic Properties of the Silica Nanoparticle–Water Interface by EPR of PH-Sensitive Spin Probes. *J. Phys. Chem. C* **2019**, *123* (49), 29972–29985. https://doi.org/10.1021/acs.jpcc.9b08007.

(65) Voinov, M. A.; Scheid, C. T.; Kirilyuk, I. A.; Trofimov, D. G.; Smirnov, A. I. IKMTSL-PTE, a Phospholipid-Based EPR Probe for Surface Electrostatic Potential of Biological Interfaces at Neutral PH: Effects of Temperature and Effective Dielectric Constant of the Solvent. *J. Phys. Chem. B* **2017**, *121* (11), 2443–2453. https://doi.org/10.1021/acs.jpcb.7b00592.

(66) Franks, G. V. Zeta Potentials and Yield Stresses of Silica Suspensions in Concentrated Monovalent Electrolytes: Isoelectric Point Shift and Additional Attraction. *J. Colloid Interface Sci.* **2002**, *249* (1), 44–51. https://doi.org/10.1006/jcis.2002.8250.

(67) Voinov, M. A. Spin-Labeled PH-Sensitive Phospholipids for Interfacial PKa Determination: Synthesis and Characterization in Aqueous and Micellar Solutions. *J Phys Chem B* **2009**, *23* (1), 1–7. https://doi.org/10.1021/jp810993s.

(68) Margita, K.; Voinov, M. A.; Smirnov, A. I. Effect of Solution Ionic Strength on the PK(a) of the Nitroxide PH EPR Probe 2,2,3,4,5,5-Hexamethylimidazolidin-1-Oxyl. *Cell Biochem. Biophys.* **2017**, *75* (2), 185–193. https://doi.org/10.1007/s12013-017-0780-y.

(69) Baumann, E. W. Determination of PH in Concentrated Salt Solutions. *Anal. Chim. Acta* **1973**, *64* (2), 284–288. https://doi.org/10.1016/s0003-2670(01)82448-x.

(70) Owenius, R.; Engström, M.; Lindgren, M.; Huber, M. Influence of Solvent Polarity and Hydrogen Bonding on the EPR Parameters of a Nitroxide Spin Label Studied by 9-GHz and 95-GHz EPR Spectroscopy and DFT Calculations. *J. Phys. Chem. A* **2001**, *105* (49), 10967–10977. https://doi.org/10.1021/jp0116914.

(71) Seal, S.; Doblhoff-Dier, K.; Meyer, J. Dielectric Decrement for Aqueous NaCl Solutions: Effect of Ionic Charge Scaling in Nonpolarizable Water Force Fields. *J. Phys. Chem. B* **2019**, *123* (46), 9912–9921. https://doi.org/10.1021/acs.jpcb.9b07916.

(72) Blüh, O. Die Dielektrizitätskonstanten von Elektrolytlösungen. *Zeitschrift für Phys.* **1924**, *25* (1), 220–229. https://doi.org/10.1007/BF01327524.

(73) Haggis, G. H.; Hasted, J. B.; Buchanan, T. J. The Dielectric Properties of Water in Solutions. *J. Chem. Phys.* **1952**, *20* (9), 1452–1465. https://doi.org/10.1063/1.1700780.

(74) Glueckauf, E. Bulk Dielectric Constant of Aqueous Electrolyte Solutions. *Trans. Faraday Soc.* **1964**, *60* (0), 1637–1645. https://doi.org/10.1039/TF9646001637.

(75) Kovaleva, E. G.; Molochnikov, L. S.; Stepanova, D. P.; Pestov, A. V; Trofimov, D. G.; Kirilyuk, I. A.; Smirnov, A. I. Interfacial Electrostatic Properties of Hydrated Mesoporous and Nanostructured Alumina Powders by Spin Labeling EPR. *Cell Biochem. Biophys.* **2017**, *75* (2), 159–170. https://doi.org/10.1007/s12013-016-0767-0.

(76) Buchner, R.; Hefter, G. T.; May, P. M. Dielectric Relaxation of Aqueous NaCl Solutions. *J. Phys. Chem. A* **1999**, *103* (1), 8–9. https://doi.org/10.1021/jp982977k.

(77) Savinell, R. F.; Ota, K.; Kreysa, G. *Encyclopedia of Applied Electrochemistry*; Springer, 2014.

(78) Endo, S.; Pfennigsdorff, A.; Goss, K.-U. Salting-Out Effect in Aqueous NaCl Solutions: Trends with Size and Polarity of Solute Molecules. *Environ. Sci. Technol.* **2012**, *46* (3), 1496–1503. https://doi.org/10.1021/es203183z.

(79) Nose, A.; Hojo, M.; Ueda, T. Effects of Salts, Acids, and Phenols on the Hydrogen-Bonding Structure of Water−Ethanol Mixtures. *J. Phys. Chem. B* **2004**, *108* (2), 798–804. https://doi.org/10.1021/jp0308312.

(80) Valadbeigi, Y. Comparison of Effects of Charge Delocalization and π-Electron Delocalization on the Stability of Monocyclic Compounds. *J. Mol. Graph. Model.* **2018**, *80*, 104–112. https://doi.org/10.1016/j.jmgm.2017.12.026.

Appendix 2A: Influence of Ionic Strength on pH Calibration

Using glass pH electrodes, one often observes significant errors due to the existence of cations similar to the proton in solutions. In particular, Li, Na, and K can give rise to proton measurement errors in concentrated solutions. These cations can exchange with the protons in the glass membrane of the pH electrode resulting in erroneous potentials across the membrane and thus erroneous pH. Another source of error is the change in proton activity due to the ionic strength of solution.

Here, we present a simple method of correcting a pH-meter calibration for the ionic strength effects in case of concentrated NaCl solutions based on a standard potentiometric titration experiment. A series of titrations in NaCl solutions at different ionic strength was performed. Experimentally obtained titration curves were fitted with theoretical curves allowing to vary parameters that linearly recalibrate the pH axis. We found that single multiplicative parameter, that essentially recalibrates the slope of the pH dependence on the electrode potential, was sufficient to obtain high quality titration fits. A series of these recalibration parameters was then plotted against the corresponding solution ionic strength. Again, it was found that a linear fit provides a sufficient description of the concentration dependence. Thus, a single proportionality parameter **p** = 0.0266 M^{-1} was obtained providing a simple means of calculating the difference between corrected pH values $\mathbf{pH_{corr}}$ and experimental readings $\mathbf{pH_{exp}}$ at a given ionic strength **I**:

$$pH_{corr} - pH_{exp} = p * pH_{exp} * I \tag{2A.1}$$

In order to estimate errors in pH readings a series of titration experiments was first performed. Batch solutions of NaCl in DI water at different ionic strength were prepared at concentrations 0M, 0.1M, 0.3M, 0.5M, 1.0M, 1.5M, 2.0M. For each concentration, a batch of 200mL was split in two bottles, 100mL each. Both bottles were thoroughly bubbled with argon

gas and stirred for about 1-2h in order to displace carbonates from the solution. The pH was continuously monitored with pH-meter connected to PC and Matlab code collecting and plotting data. After the pH readings settled one bottle was mixed with about 0.5mL of HCl, intended as the titrant solution at about pH≈1. Although rather arbitrary, the pH of the titrant was carefully measured as it is a required parameter for further evaluation. The other bottle was mixed with a half of a sodium hydroxide pellet, about 50mg, bringing pH of the solution to about pH≈12. Again, precise target pH value is rather arbitrary, but precisely measured later during the titration. Keeping solution values around pH≈12, and titrant pH values around pH≈1 allows to collect titration curve in the wide range of pH≈12 to pH≈2 at total titrant infusion volumes between 5-15mL per 30mL of initial volume of the solution.

Initial volume of the alkaline solution and infusion volumes of the acidic titrant are another necessary prerequisite for further evaluation. In order to precisely control infusion volumes, we utilized high precision syringe pump. The syringe pump takes as a parameter the diameter of the syringe used. Although manufacturers provide syringe diameters, we corrected the values using a simple gravimetric measurement. Dispensing a known volume **V** (10mL) of DI water of known mass density **ρ** (0.99707g/mL at 25^{o}C) one can weigh the mass of water **m** and correct syringe diameter given by manufacturer $\mathbf{D_{man}}$ to the corrected diameter $\mathbf{D_{corr}}$ according to following formula:

$$D_{corr} = D_{man}\sqrt{\frac{m}{\rho * V}} \tag{2A.2}$$

After having a precise volumetric control and well calibrated pH-meter in the anticipated range of titration extent, we dispensed precisely 30mL of solution in a small 50mL beaker. This small beaker was placed in another water jacketed beaker tempered at 25^{o}C and closed with laser

cut polystyrene lid with openings for pH-meter, and infusion and argon gas tubing. In fact, the whole infusion was done in such a manner that no contact of prior carefully bubbled titration solution with open air happened. The solution also remained well stirred with small magnetic bar and argon bubbled for the duration of the titration experiment. In a similar fashion we handled infusion of the acidic titrant. The infusion volumes were automatically controlled with a Matlab script allowing for collection of approximately pH equidistant points, set to about 0.1 pH step, but with minimal infusion volume about 5ul. The automatic titration was allowed to continue until target pH differential of 10 pH units or total infusion volume of 15mL was achieved, whichever came first.

In the following, accumulated titration data were fitted with theoretical curve based on standard solution of equations of mass balance, electro neutrality and first order kinetic equilibrium equations (water dissociation equation in this case). This is again the best handled with a Matlab script that calculates expected pH values dependence on total titrant infused volume and on other initial titration parameters. The basic initial parameters can be expressed in terms of the pH of the titrant, initial pH of the solution, and initial volume of the solution, that are fixed and readily know through direct measurement. However, one quickly finds that fits, especially at high ionic strength are rather poor. In order to rectify the discrepancy, we modified pH axis with a linearly scaled equation, introducing new scaling parameters p_1 and p_2:

$$pH_{corr} = p_1 * pH_{exp} + p_2 \tag{2A.3}$$

Varying parameter p_1 alone provided sufficient fit improvement. Varying parameter p_2 as well improves slightly overall fitness values but we decided to set it equal to zero. The meaning of the parameter p_2 is the pH offset at pH=0. Although physically meaningful it is expected to be a small value due to a high proton concentration in the solution (1 M at pH=0), which is for the

most part higher or comparable to the ionic strength range in this study. Such an offset would be most meaningful at ionic strength that maximizes deviation due to activity changes. Analyzing empirical Davie equation one can find that the most unfavorable case of ionic strength around 0.1 M results in pH changes of about 0.1 pH unit. Setting $\mathbf{p_2}$ equal to zero also simplifies scaling equation to a single parameter $\mathbf{p_1}$**.** Parameter $\mathbf{p_1}$ is still dependent on the ionic strength. By plotting fitted values against ionic strength we can establish yet another linear dependence. We can assume $\mathbf{p_1}$ equal to one at zero ionic strength, as it should be an ideal titration in pure DI water, and write

$$p_1 = p * I + 1 \tag{2A.4}$$

Thus, substituting equation (2A.4) into (2A.3) and setting $\mathbf{p_2}$=0 we arrive to the calibration equation (2A.1).

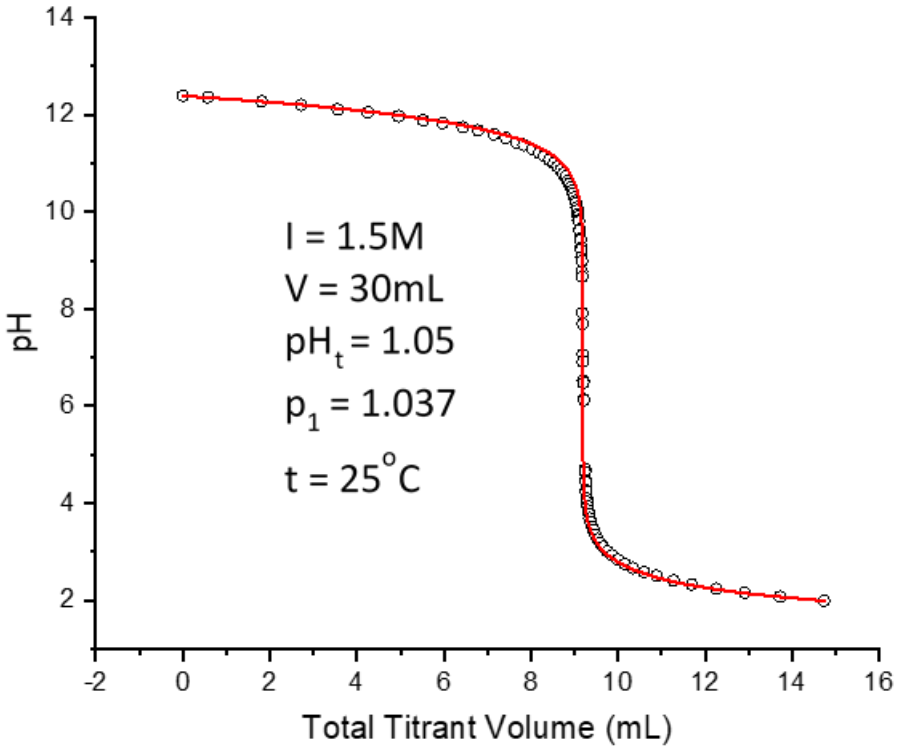

Figure 2A.1. Example of titration at ionic strength I = 1.5 M. Experimental values (black circles) were fitted with theoretical curve (red line). Fixed parameters of the fit were initial solution volume V = 30mL, titrant pH_t = 1.05 and temperature t = 25°C. Optimal fit was achieved for variable scaling parameter p_1=1.037.

Table 2A.1. Dependence of scaling coefficient p_1 on ionic strength of the solution. Linear fit with equation (2A.4) provides the scaling coefficient p = 0.0266 (0.0236, 0.0296) M^{-1} with 95% confidence bounds.

Ionic Strength (M)	0	0.1	0.3	0.5	1	1.5	2
Scaling Coeff. **p_1**	0.999	1.002	1.005	1.02	1.029	1.037	1.053

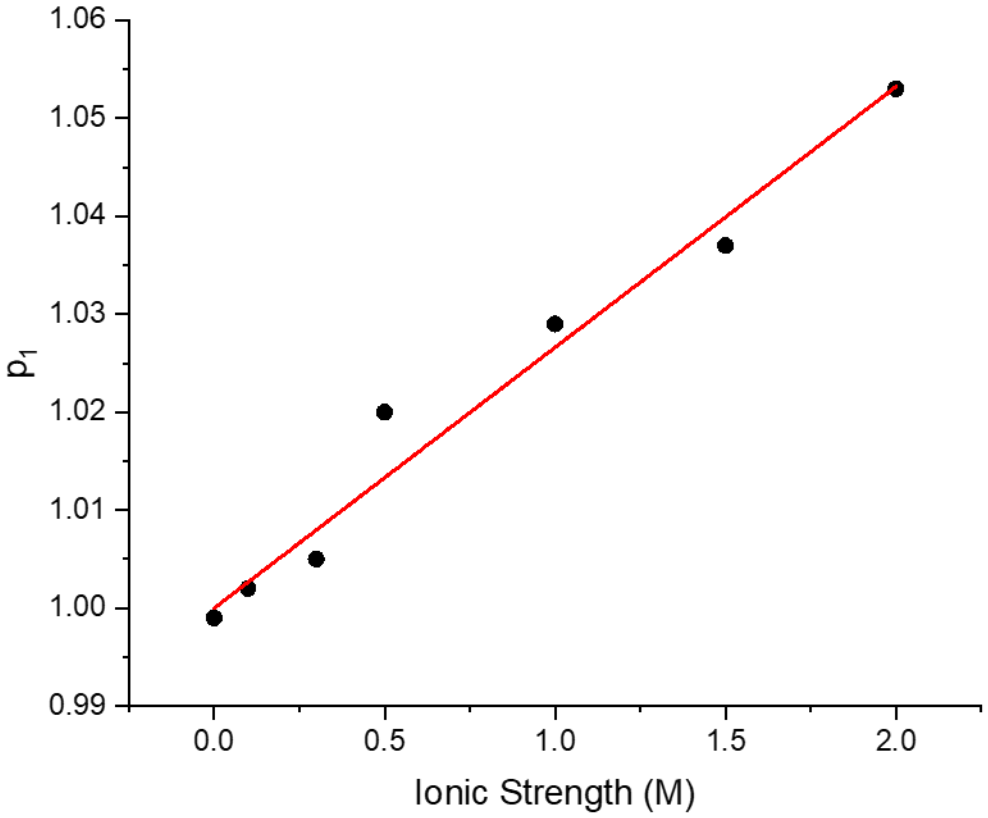

Figure 2A.2. Dependence of scaling coefficient p_1 on ionic strength of the solution. Graphical representation of Table 2A.1**.**

Appendix 2B: Electrostatic shifts (ΔpK_a^{el}) as a function of pH

Silica surface charges when the pH of a solution increases. During EPR titration, non-protonated nitroxide fraction dependence on pH diverges from the classical Henderson-Hasselbalch sigmoidal curve, which corresponds to eq.(2.3). This effect is shown in Figure 1.16 and thoroughly discussed in Results and Discussion section in Chapter 1. Due to the charging surface, an effective pK_a^{obs} of an attached nitroxide is dependent on pH because the ΔpK_a^{el}

contribution in eq.(2.2) grows as a function of pH. Its value differs from ~0, when pH equals the isoelectric point, and up to ~3.4, in the case of fully charged surface in 0.05 M solution, where the screening effect is minimal. It is possible to estimate ΔpK_a^{el} value using eq.(2.4) and function of ψ dependence on pH (Figure 2.9 and Table 2.4). Moreover, with calculated ΔpK_a^{el} and estimated ΔpK_a^{pol} (Table 2.5), we can find a dependence of effective pK_a^{obs} on pH. The results for salt solutions with different concentrations are summarized in Figure 2B.1 and Table 2B.1.

As the salt contraction increases, the more prominent screening effect becomes. When [NaCl] = 0.05 M, the probe is fully exposed to the surface potential, and therefore, it shows the broadest range of ΔpK_a^{el} (from 0 to 3.4) and the largest slope in Figure 2B.1 (black circles, black line). Meanwhile, when the surface is effectively screened, at [NaCl] = 0.5 M, ΔpK_a^{el} does not exceed 0.7, thus showing that the local environment of the nitroxide is not significantly affected by the electrostatic contribution.

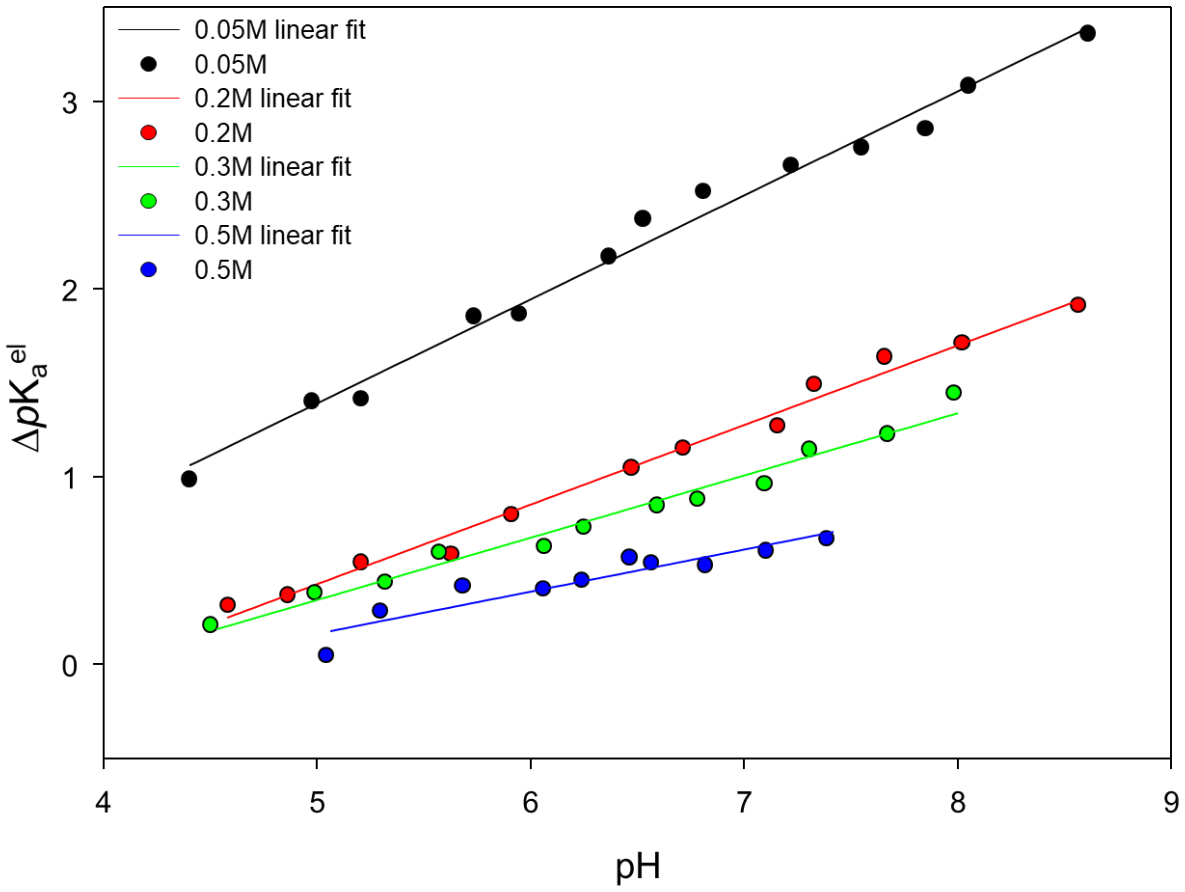

Figure 2B.1. Electrostatic pK_a shift (ΔpK_a^{el}) of IKMTSL spin probe attached to SiNP surface depending on pH in solutions with different NaCl concentrations.

Table 2B.1. Electrostatic pK_a shift (ΔpK_a^{el}) and corresponding pK_a^{obs} of IKMTSL spin probe attached to SiNP surface depending on the pH of the solution. The results are presented for each NaCl concentration.

[NaCl] = 0.05 M			**[NaCl] = 0.2 M**			**[NaCl] = 0.3 M**			**[NaCl] = 0.5 M**		
pH	**ΔpK_a^{el}**	**pK_a^{obs}**	**pH**	**ΔpK_a^{el}**	**pK_a^{obs}**	**pH**	**ΔpK_a^{el}**	**pK_a^{obs}**	**pH**	**ΔpK_a^{el}**	**pK_a^{obs}**
4.41	0.99	5.02	4.58	0.31	5.37	4.51	0.21	5.60	5.05	0.05	5.68
4.98	1.40	5.43	4.87	0.37	5.43	4.99	0.38	5.77	5.30	0.28	5.91
5.21	1.41	5.44	5.21	0.54	5.60	5.32	0.44	5.83	5.68	0.42	6.05
5.74	1.85	5.88	5.63	0.58	5.64	5.57	0.60	5.99	6.06	0.40	6.03
5.95	1.87	5.90	5.91	0.80	5.86	6.07	0.63	6.02	6.24	0.45	6.08
6.37	2.17	6.20	6.47	1.05	6.11	6.25	0.73	6.12	6.46	0.57	6.20

Table 2B.1. (continued).

6.53	2.37	6.40	6.72	1.15	6.21	6.59	0.85	6.24	6.57	0.54	6.17
6.81	2.52	6.55	7.16	1.27	6.33	6.78	0.88	6.27	6.82	0.53	6.16
7.22	2.66	6.69	7.33	1.49	6.55	7.10	0.96	6.35	7.10	0.60	6.23
7.55	2.75	6.78	7.66	1.64	6.70	7.31	1.14	6.53	7.39	0.67	6.30
7.85	2.85	6.88	8.02	1.71	6.77	7.67	1.23	6.62			
8.05	3.08	7.11	8.57	1.91	6.97	7.98	1.45	6.84			
8.61	3.36	7.39									

Appendix 2C: Dielectric constant calibration based on pKaobs of IKMTSL-ME in salt solutions with various concentrations

The effect of ionic strength on dielectric constant (ε) of bulk water has been thoroughly studied.[76] Combining our EPR titration data for IKMTSL-ME in various NaCl concentrations (Table 2.2) with the previously reported data for ε, we were able to build a collaboration equation that allows estimating dielectric constant based on the pK_a^{obs} of IKMTSL-ME spin probe (Figure 2.7, solid line):

$$\varepsilon = -(1537.66 \pm 233.19) + (568.20 \pm 74.96)*(pK_a^{Obs}) - (49.76 \pm 6.02)*(pK_a^{Obs})^2 \quad (2C.1)$$

CHAPTER 3

Thermal Unfolding and Monomer Migration in Anabaena Sensory Rhodopsin (ASR) in Lipid Bilayers by Site Directed Spin Labeling EPR

Vladislav Perelygin, Sergey Milikisiyants, Maxim A. Voinov and Alex I. Smirnov

3.1 Introduction

3.1.1 *Anabaena sensory rhodopsin (ASR) as a model system for membrane protein studies*

Structure and function of membrane proteins have been subjects of a large number of studies due to their key role in many cellular processes, such as ion regulation, enzymatic activity cellular reception, and many others.[1,2] Membrane receptor proteins relay signals between the cell's internal and external environments. Typically, proteins need to fold to a certain conformation in order to function properly. It's been shown that misfolding can be a primary cause for many severe diseases.[3] Therefore, it is of tremendous importance to understand the mechanisms behind membrane protein assembly. While folding mechanisms of soluble proteins have been extensively studied, membrane proteins are an extremely hard target due to the complexity of their environment. Factors, such as pH and ionic strength of the media, lipid composition of the membrane, temperature, have the most prominent effect on protein stability, folding, and an ability to form oligomers.[4] When designing an experiment, not only does a researcher need to express and purify a sufficient amount of the protein, but also it is necessary to artificially create the protein local environment closely mimicking the natural one.

Among many membrane proteins, the rhodopsin family has attracted a significant interest from the scientific community. Due to extensive research efforts, genes corresponding to different types of rhodopsin have been found in many organisms including archaea, fungi, numerous

eubacteria, and viruses.[5–7] The reason for such interest is that the diverse rhodopsin family is a part of G-protein-coupled receptors (GPCRs) superfamily, and they serve as a suitable model system for the research of membrane proteins and GPCRs in particular. GPCRs occupy a special place among other membrane proteins since they are one of the most common regulatory systems in the human body. There are approximately 950 genes corresponding to GPCR in human genome with half of them being sensory GPCR.[8] Therefore, it comes as no surprise that approximately 34% of FDA approved drugs target GPCR,[9] which creates a high demand in precise understanding of their function and structure.

Rhodopsin family is divided into two classes: bacterial rhodopsin, produced in Bacteria, Archaea, and some Eukaryotes, also recognized as type-I, and animal rhodopsins, known as type-II.[10] The very first representatives of these groups were bacteriorhodopsin (BR), light-dependent proton pump of *Halobacteria* bacteria,[11] and Type II bovine visual rhodopsin,[12] which was used as a model system to study vision in animals and humans. Several advantages, including high expression level and ease of isolation, made them a remarkable model for studying membrane proteins and their folding pathways using experimental techniques such as X-ray crystallography,[13] solid-state NMR (ssNMR),[14] cryogenic electron microscopy (cryo-EM),[15] and high-speed Atomic Force Microscopy (AFM).[16]

Although rhodopsins of different origins often considerably vary by their amino acid composition, they have the similar secondary structure of seven transmembrane α-helices (TM), also known as Opsin, which is a distinct feature of all GPCRs (Figure 3.1). Another property that is shared by majority of rhodopsins is the ability to bind with a chromophore retinal, which serves as a light-absorbing and energy-storing agent. After the retinal binding, a photoactive protein can

use it to execute one of its diverse functions, such as ion transport, enzymatic activity, and signal transfer in light registering complexes.

Figure 3.1 demonstrates basic structural properties of rhodopsins with the C-terminus merged inside the cell and N-terminus placed outside of the cell. Its cofactor retinal is bound by forming a Schiff base with lysine in TM 7 helices.[17] The Schiff base protonation state of the retinal serves as a trigger for signaling or transport activity.

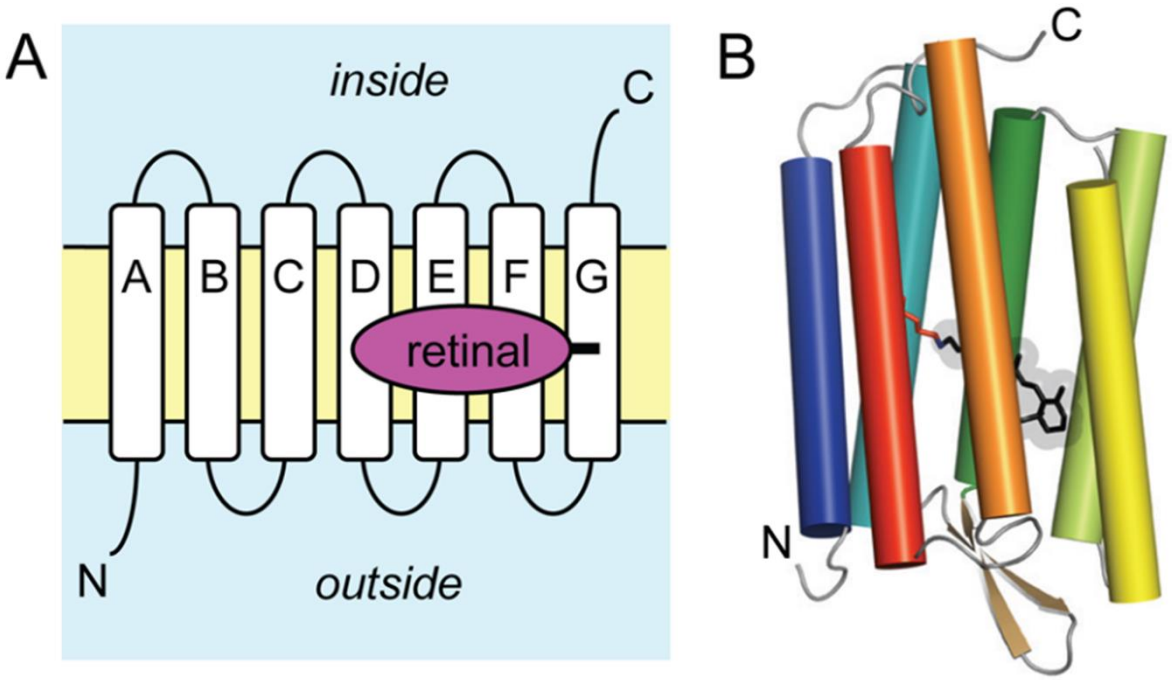

Figure 3.1. Cartoon representation of structure of a typical rhodopsin. **(**A) Rhodopsin immersed in a lipid membrane with retinal bound to TM 7 helix. (B) BR helixes arrangement. Adapted from literature.[17]

Rhodopsin is functionally activated when its cofactor retinal captures a photon of an appropriate wavelength. A closer look at this process reveals one of the fundamental differences between type-I and type-II rhodopsins (Figure 3.2). Bacterial rhodopsins typically have an all-

trans configuration of retinal and, upon light absorption, it undergoes photoisomerization to 13-*cis* retinal. Meanwhile, type-II retinal is in 11-*cis* conformation and it converts to all-*trans* form.[10] The absorption maximum, corresponding to the energy of $\pi - \pi^*$ transition, is determent by the length of the π-conjugated polyene chain, protonation state of the Schiff base, and local environment, that includes pH and ionic strength.[18] Thus, retinal can absorb light in the range of 400−700 nm depending on the conditions, causing different coloration in rhodopsins of different origins.

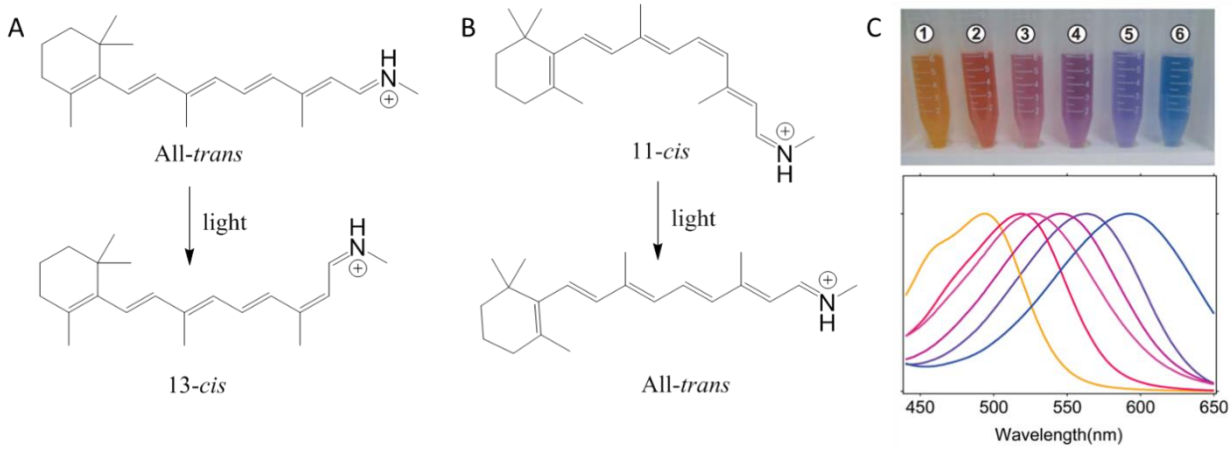

Figure 3.2. Retinal structure transitions upon light absorption. (A) Retinal transition in bacterial rhodopsins. (B) Light-driven transition in animal rhodopsin. (C) Diversity of rhodopsin types with an absorption maximum at different wavelengths; numbers correspond to the following rhodopsins: (1) a blue- proteorhodopsin (LC1-200, pH 7), (2) Q105L mutant of LC1-200 (pH 7), (3) a green-proteorhodopsin (EBAC31A08, pH 7), (4) A178R mutant of green-proteorhodopsin (pH 7), (5) bacteriorhodopsin (pH 7), (6) *H. salinarum* sensory rhodopsin I (pH 4).[17]

In order to enhance their stability, many proteins of the rhodopsin family tend to form oligomers. It has also been shown that oligomerization is directly correlated with protein

allostery.[19] Oligomerization is affected by many factors, and its underlying mechanism may rely on different intra-molecular interactions. For instance, *Gloeobacter* rhodopsin forms the His87−Asp121 bond, also known as a salt bridge, which leads to trimerization of the protein.[20] While the formation of salt bridges seems to be a common feature, other interactions often have a significant effect on the process. For example, it has been shown that in bacteriorhodopsin oligomerization is promoted by intrinsic glycolipid molecules.[21] In Halorhodopsins this process is supported by intermolecular interaction between aromatic residues of the individual monomers.[22] Among the most common oligomerization patterns are dimers (*e.g.* channelrhodopsin[23]), trimers (*e.g. Halobacterium salinarum* bacteriorhodopsin[24]), penta- and hexamers (*e.g.* blue light-absorbing PR[25]). Such multi-protein structures are hard to study due to the complexity of the local protein environment.

Although it was shown that rhodopsin monomers are functionally active, monomerization might affect its activity and stability. In the attempt to find what might cause monomerization, researchers tried to use point mutations and diverse stress factors, including elevated temperatures and detergents.[22,26,27] For instance, it was demonstrated that oligomers can be decomposed to monomers when they are solubilized in a detergent[28,29], while mutation in His residue (H87M) of *Gloeobacter* rhodopsin, was shown to break the salt bridge, causing monomerization.[20]

Thermal stability of integral membrane protein rhodopsin is crucial for many organisms living in elevated temperatures. Each of the rhodopsin molecules contains covalently bound cofactor retinal. Because half-life time of a liberated retinal is about 1 h at 52 °C and shorter at higher temperatures,[30] it has to be conformationally protected in the protein binding pocket in order to retain functionality. This is the case for *Thermus thermophilus* JL-18, a thermophilic bacterium

that lives at high temperature (75 °C). *Thermus thermophilus* uses thermophilic rhodopsin (TR) as a light-activated proton pump.

Numerous studies demonstrated that a native lipid environment greatly promotes thermal stability of rhodopsins and prevents monomerization. For example, by using Size-Exclusion Chromatography (SEC) and visible Circular Dichroism (CD) spectroscopy, it was shown that the TR trimers dissolved in a detergent irreversibly dissociate to monomer at 68 °C.[31] However, the consequent AFM, ssNMR, and Raman spectroscopy studies revealed that in lipid environment TR forms pentamers and retains its oligomeric structure at its physiological temperature (75 °C).[32] In addition to that, it was shown that monomeric TR remains functional, although it led to helixes conformational changes, and specifically in the retinal pocket.[31]

The protein of interest in this work, *Anabaena* sensory rhodopsin (ASR), is a cyanobacteria rhodopsin that serves as a translational regulator and is known to be responsible for activation a soluble transducer protein for photosensory reception.[33] In contrast to TR, ASR demonstrates an enhanced oligomer stability. Using ssNMR, it was shown that ASR forms trimers that retain their structure even in the presence of detergents and when it is reconstituted in lipid environment.[34,35] Furthermore, a study, where ASR thermal unfolding was monitored through H/D exchange, suggested that trimers do not dissociate even at 80 °C, and that the oligomerization might be the key reason of its high thermal stability.[36] Combination of site-directed spin labeling (SDSL), EPR and ssNMR allowed to elucidate the structure of the trimer (Figure 3.3), where EPR was used to provide constraints with respect to intra-trimer distances between selected residues.[37]

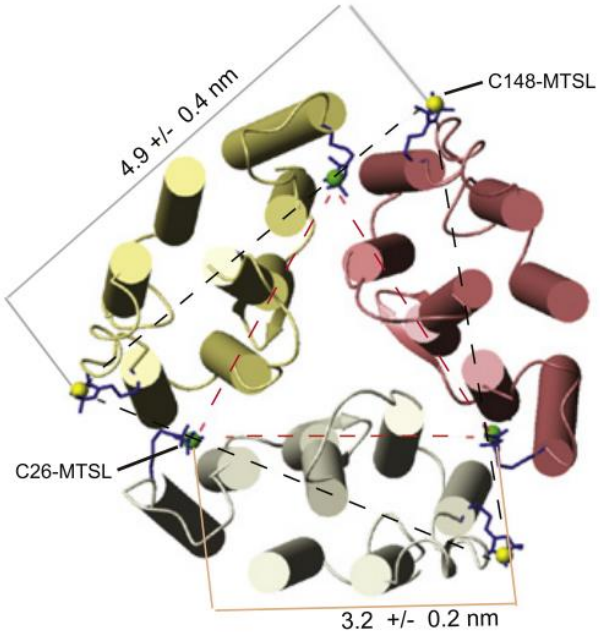

Figure 3.3. ASR trimer with indicated mutation sites and corresponding distances. Thus, distance between two S26C mutation sites is approximately 3.2 nm, while labels at N148C sites show 4.9 nm. Adapted from literature.[37]

The studies of conformation of integral membrane proteins are particularly difficult because of the severely limited arsenal of chemicals to induce controllable monomerization and unfolding, as well as the pronounced propensity of such proteins to aggregate. Thermal denaturation methods are becoming increasingly popular to characterize the protein stability because of ease of implementation and nearly universal applicability to different protein classes. While many biophysical methods could be employed to monitor thermal rearrangements in proteins at a large scale, SDSL EPR brings in the capability to monitor local unfolding events.

In this study, CW EPR and site-directed spin labeling were employed to elucidate the mechanism of thermal unfolding in ASR monomers. To target different regions of the protein, two

mutations were introduced, S26C to the helix A and N148C to the loop E-F. Then the cysteine was labeled with MTLS spin label (Figure 3.3) according to the procedure described earlier.[37] It was previously proven that these mutations do not cause protein misfolding.[38,39] In addition, Double electron-electron resonance (DEER) traces have been measured for S26C ASR with paramagnetic dilution factors 1:6 (labeled to unlabeled mutants) and 1:4 (labeled mutant to wild-type ASR). The effect on the protein conformation upon heat exposure was investigated, resulting in a proposition of a monomer exchange model.

3.1.2 Double electron-electron resonance (DEER) theory

Over the past two decades, double electron-electron resonance (DEER) spectroscopy has been established as one of the most applied tools for measuring nanometer scale distances and distance distributions in disordered (non-crystalline) samples.

Up to this date, the dead-time free four-pulse DEER sequence[40] remains the most used pulsed EPR method for inter-spin distance measurements. This pulse employs microwave pulses at two separate frequencies: three pulses at "observer" frequency ν_1 and one pulse at "pump" frequency ν_2 (Figure 3.4). Thus, electron spins involved in a DEER experiment are of two groups: A-spins, excited by the three observer pulses and B-spins, excited by the single pump pulse. These two spin sub-ensembles are selected to be spectrally well separated to avoid simultaneous excitation by both applied frequencies. In a DEER experiment, interspin distance information is obtained via direct observation of their magnetic dipole-dipole coupling.

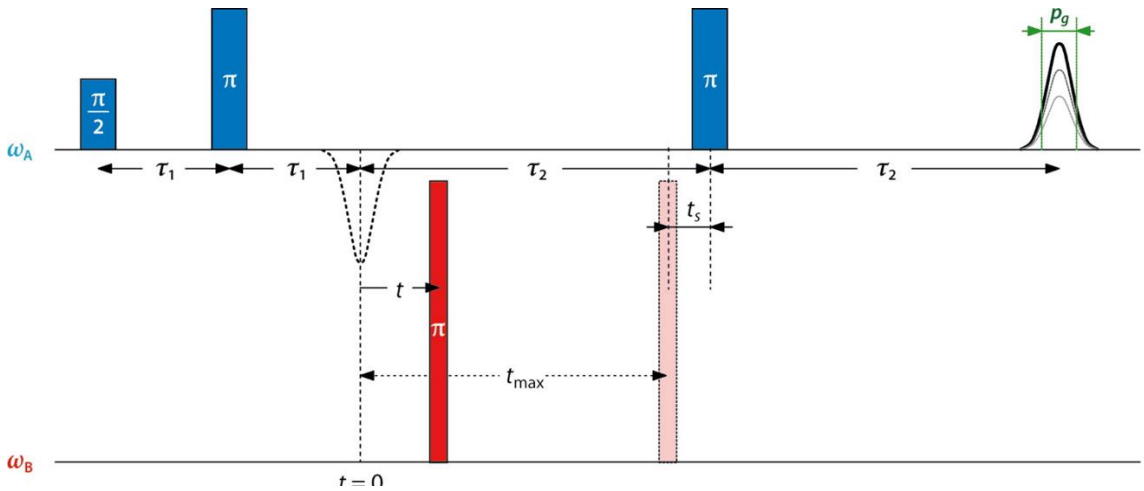

Figure 3.4 Schematic representation of the four-pulse DEER sequence. Delays τ_1 and τ_2 between the observer pulses (blue) are fixed, delay *t* between the primary echo and the pump pulse (red) is varied. Refocused echo intensity, observed at time $2 * (\tau_1 + \tau_2)$ after the first observer pulse, is monitored as a function of the delay *t*. Picture adapted from the literature.[41]

In further description of DEER, we will neglect electron spin relaxation for simplicity. Without the pump pulse, the observer spins would be fully refocused to their initial magnetization at time$2 * (\tau_1 + \tau_2)$ after the first observer pulse creating a refocused spin echo. When the pump π-pulse flips B spins, it inverses the direction of the dipolar magnetic field induced by these spins and therefore changes the local magnetic field experienced by A spins. This shifts the precession frequency of A-spins by $\pm\omega_{ee,i}$ (corresponding to A-B_i magnetic coupling), which in turn induces the phase shift of their magnetization $\phi = \pm\omega_{ee,i}t$. This phase shifts decrease the refocused echo amplitude inducing periodic modulations (as t is valied) of the observed signal. In real systems, its spin pairs are not fully isolated.. Therefore, it is usually necessary to take into account the effect of multiple B-spins simultaneously interacting with each of the A-spin. Let's denote by $\lambda < 1$ the

fraction of B-spins flipped by the pump pulse. Thus, the dependence of echo amplitude on $\omega_{ee,i}$ is defined by equation:

$$\nu(t) = \prod_i (1 - \lambda_i[1 - \cos(\omega_{ee,i}t)]) \tag{3.1}$$

where $\nu(t)$ – amplitude of refocused echo signal, $\omega_{ee,i}$ -electro-electron coupling, λ_i – fraction of the magnetically coupled B-spins excited by the "pump" pulse.[41]

Magnetic dipole-dipole coupling between two isolated spins A and B depends on the angle Θ between the external static field and the vector connecting these spins:

$$\omega_{ee} = \omega_{dd}(3cos^2\Theta - 1) \tag{3.2}$$

Here ω_{dd} is dipole-dipole coupling constant defined as,

$$\omega_{dd} = \frac{g_A g_B \mu_\beta^2 \mu_0}{4\pi h} \frac{1}{r^3} \tag{3.3}$$

where g_A and g_B – g-values for A and B spins, μ_β - Bohr magneton, r – distance between the spins. By measuring spin echo amplitude as a function of time *t*, it is possible to obtain the distance between the spins.

The B-spins coupled to an A-spin usually consist of a single B-spin located on the same molecular frame with the A-spin and multiple B-spins not rigidly connected to the A-spin and thus randomly distributed in space with respect to the A-spin. In this case, the observed spin echo amplitude (DEER signal) can be written in the following form:

$$\nu(t) = \left(1 - \lambda\left[1 - \int_0^1 \cos\left(\omega_{dd}\,(1 - 3\,cos^2\Theta)t\right)\, d\,\cos\Theta\right]\right) \mathrm{B(t)} \tag{3.5}$$

Here ω_{dd} is the coupling between the A-spin and spatially correlated B-spin (intramolecular contribution) and B(t) is a background decay coming from randomly distributed B-spins(intermolecular contribution).

During the signal post-processing, B(t) is carefully estimated and subtracted. Thus, permits extraction of the so-called form factor - periodically modulated function corresponding to spatially correlated A-B spins dipolar coupling (Figure 3.5). One of the essential features of the DEER form factor is its modulation depth. In case, where more than one B-spin is spatially correlated with an A-spin, the modulation depths is proportional to the number of spatially correlated B-spins (Figure 3.5 B). This property for example can be used to count number of monomers in an oligomer.

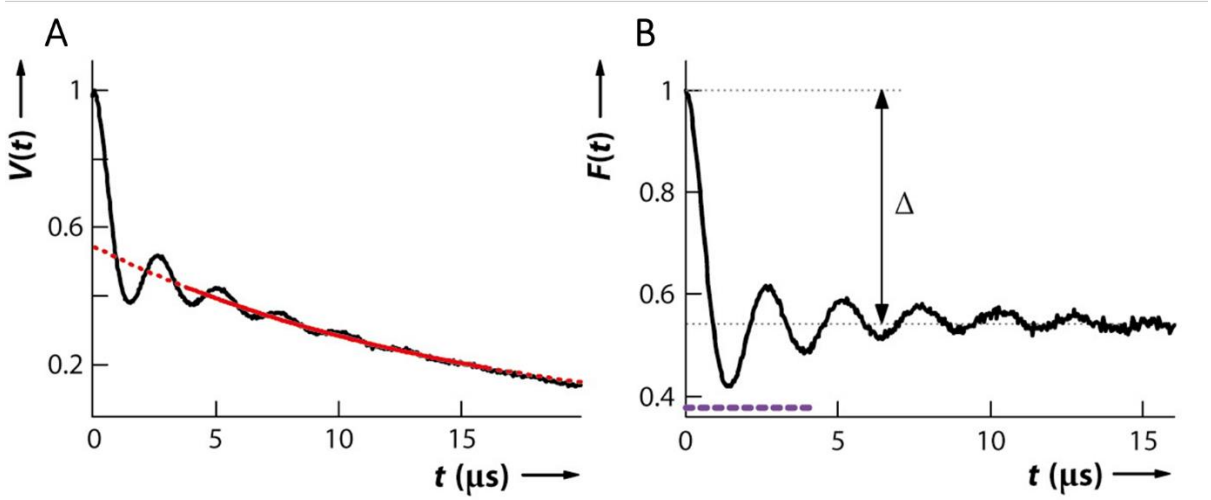

Figure 3.5. (A) An example of a DEER trace. The background function (solid red line) is fitted and subtracted during the signal postprocessing. (B) The extracted form factor, representing a dumped oscillating function and corresponding to spatially correlated B-spins. Adapted from literature.[41]

3.2 Experimental Section

3.2.1 *ASR expression, labeling and reconstitution in lipids*

Samples were expressed, labeled, and reconstituted by Prof. Ladizhansky's research group (University of Guelph, Guelph, ON, Canada). The two Cys mutants of ASR, N148C and S26C, were employed in this study. S26C mutation is located on the A-helix loop facing towards the confined space between the helixes. N148C is located on the E-helix loop, exposed to the environment outside the protein. Protein samples were labeled with a nitroxide MTSL-methanethiosulfonate (Figure 1.7, Chapter 1) spin label highly specific to SH groups of cysteines. The spin labeling procedure was applied to a protein solubilized in detergent (DDM). When the spin labeling procedure was complete, the spin labeled protein was reconstituted into DMPC-DMPA (9:1, w/w) lipid vesicles; excess detergent was removed using Bio-beads (SM-II, Bio-Rad Laboratories, Inc., Hercules, CA, USA). Two samples were prepared: 1 to 6 mixture of labeled and unlabeled ASR, respectively, as well as 1 to 4 labeled to wild type ASR. The need for dilution was due to fact that pure labeled ASR demonstrated short electron spin relaxation times (in particular T_2) and, subsequently, fast echo decay during DEER experiments. Also, the unwanted background signal in the DEER traces caused by intermolecular magnetic interactions was strongly pronounced in the undiluted samples. The diamagnetic dilution both, increased electron spin relaxation and strongly decreased the background signal, which in turn helped to improve accuracy of determination of distance distribution especially over the longer distances. The diamagnetic dilution ratios 1:4 and 1:6 were shown to be optimal for DEER spectroscopy.[37] Finally, the samples were suspended in D_2O based buffer with 24 mM Chess, 10 mM NaCl and adjusted to pH=8.9. The solution was transferred to Q-band quartz tubes (O.D. = 1.6 nm, I.D. = 1.1 nm, VitroCom, Maintain Lake, N), and the liquid excess was removed.

3.2.2 *EPR measurement of ASR thermal unfolding*

X-band (9.5 GHz) continuous wave (CW) EPR spectra of the spin labeled protein were acquired using either Bruker Biospin (Billerica, MA) ELEXSYS E500 spectrometer equipped with a Selected Super High-Q Sensitive Resonator or ELEXSYS E580 spectrometer equipped with a standard rectangular TE_{102} microwave cavity. The magnets with EPR probeheads were located at about 8 ft from each other allowing for a rapid (a few seconds) switching between the experimental condition. All CW EPR spectra were obtained using following experimental settings: modulation amplitude was set to 1 G; time constant, 20.48 ms; conversion time 20.55 ms, scan width 120 G, sweep time 42.09 s, incident microwave power, 6.3 mW. The number of accumulated scans was varied depending on the EPR signal intensity. On average, 15 scans were collected and averaged out to achieve a satisfactory signal-to-noise ratio.

The ELEXSYS E500 spectrometer was outfitted with The Digital Temperature Control System, ER 4141VT, which was employed to control the temperature inside the microwave resonator. To avoid the effects of unwanted temperature gradients and accurately estimate actual temperature of the sample, a thermocouple emerged in mineral oil inside a Q-band quartz tube was used to mimic the thermal properties of the sample.

CW EPR spectral acquisition was performed in the following steps. First, the sample was rapidly inserted to the pre-heated cavity of the ELEXSYS E500 spectrometer and a spectrum was collected over ca. 2 min period. After that, the sample was cooled back to room temperature, and another spectrum was collected using ELEXSYS E580 at room temperature (21 ^{o}C). Therefore, two CW EPR spectra were collected for each temperature step: *i*) during the heat exposure and *ii*) at room temperature after. The CW EPR spectra were analyzed using a two-state model to derive

the fraction of the unfolded component that was plotted as a function of temperature. CW EPR measured at room temperature was used to control label stability upon heat exposure.

The spectra were analyzed using a two-state model to derive the fraction of the unfolded component that was plotted as a function of temperature. Double integrals of the spectra at room temperature were calculated to evaluate stability of the nitroxide upon the heat exposure.

3.2.3 *Reversible thermal monomerization-trimerization of ASR followed by DEER*

Trimer exchange in ASR protein was studied by Q-band (34 GHz) DEER spectroscopy. The spectra were measured using a custom-built Bruker ELEXSYS E580 spectrometer outfitted with SuperQ-FT bridge and SuperQ-FT Solid State 10 W Amplifier (all components are from Bruker Biospin, Billerica, MA, USA). Bruker ER 4118CF flow cryostat operated with liquid nitrogen was employed to maintain 74 K during the measurements. Dead-time-free four-pulse sequence[40] was used with the following parameters: pump and observer frequencies equal 33.786GHz and 33.726 GHz, respectively; magnetic field was set to 12.009.8 G; three observer pulses had fixed position; time separation between the first and the second pulse of $\tau 1$ = 140 ns, and the separation between the second and the third pulse was $\tau 2$ = 2340 ns; the lengths of the observer pulses were set to 16 and 28 ns for the $\pi/2$- and π-pulses, respectively, and the pump pulse was 22 ns; pump pulse increment was 2-ns for the overall range of 2200 ns.

A lipid reconstituted SR sample in a Q-band capillary tube was subjected to heating for 30 s at a target temperature. To do that, the sample was inserted into a pre-heated copper block with a drilled hole to closely match the diameter of the Q-band tube. The temperature of the sample was monitored by a thermocouple immersed in the mineral oil inside a separate Q-band tube inserted into another hole of the same copper block. The copper block was placed in a compartment of a thermocycler (VWR, analog dry block heater, Model #949310) which was set to a desired

temperature. The measurements with a thermocouple indicated that the sample was fully equilibrated to a target temperature in less than 30 s upon insertion of the Q-band EPR tube into the pre-equilibrated copper block.

After the equilibration of the sample at a target temperature, the sample was flash-frozen by immersing the tube into *iso*-pentane maintained at approximately -150 ^{o}C (123 K). A beaker with *iso*-pentane was placed into a liquid nitrogen bath, and when the temperature in the beaker reached ~-150 ^{o}C, ASR sample was flash-frozen. The Q-band tube with a frozen ASR was inserted into a precooled EPR cryostat at 77 K. After each measurement and before the next heat exposure, ASR was kept wrapped in aluminum foil for 5 to 10 min to let it completely equilibrate with room temperature. The same protein sample (S26C or N148C mutant) was used in the heating-cooling cycles, so the collected data are the result of cumulative hearing steps each time to a higher temperature.

3.3 Results and Discussion

A series of CW EPR measurements were performed to investigate thermal unfolding of ASR. Rotational correlation time of a nitroxide spin label is an extremely sensitive indicator of the label local environment. That is reflected in the shape of CW EPR spectra. These changes provide means for monitor local effects of thermal unfolding. An EPR spectrum corresponding to a spin label in a slow-motion regime suggests that the label is conformationally restricted. Such molecular movement restrictions indicate that the protein is in its compact folded conformational state. The protein unfolding decreases steric restrictions. This decreases the rotational correlation time of a spin label which in turn decreases spectral line width resulting in observable sharpening of the spectral features. It should be noted, however, that due to motion restriction imposed by the

linker and covalent attachment of the probe, EPR spectra inevitably exhibit broadening of the spectral features caused by incomplete averaging of magnetic anisotropies.

The two mutants studied, N148C (Figure 3.6) and S26C (Figure 3.7), were found to have different transition temperatures. EPR spectra acquired at room temperature demonstrate the spin label being in a slow-motion regime, suggesting that the protein is in the folded state. Gradual temperature increase results in observable changes of the EPR spectra, caused by a decrease of rotation correlation time. As temperature increased, the spectral features corresponding to the unfolded protein became more pronounced. Finally, at 74 ^{o}C for N148C and 96 ^{o}C for S26C, the spectral features corresponding to the folded form of ASR completely vanished. EPR spectra did not change when the protein was further exposed to higher temperatures, which confirmed that the unfolding was complete. Thus, for N148C the spectral changes were observed in the temperature range 55 to 70 ^{o}C (Figure 3.6 A), while S26C demonstrates the transition at higher temperatures - from 74 to 94 ^{o}C (Figure 3.7 A). This suggests that the S26 site is located in a more confined local environment, which is also confirmed by its spectral features corresponding to slower spin label motion. That is expected since the S26C spin probe faces the inter-helical space.

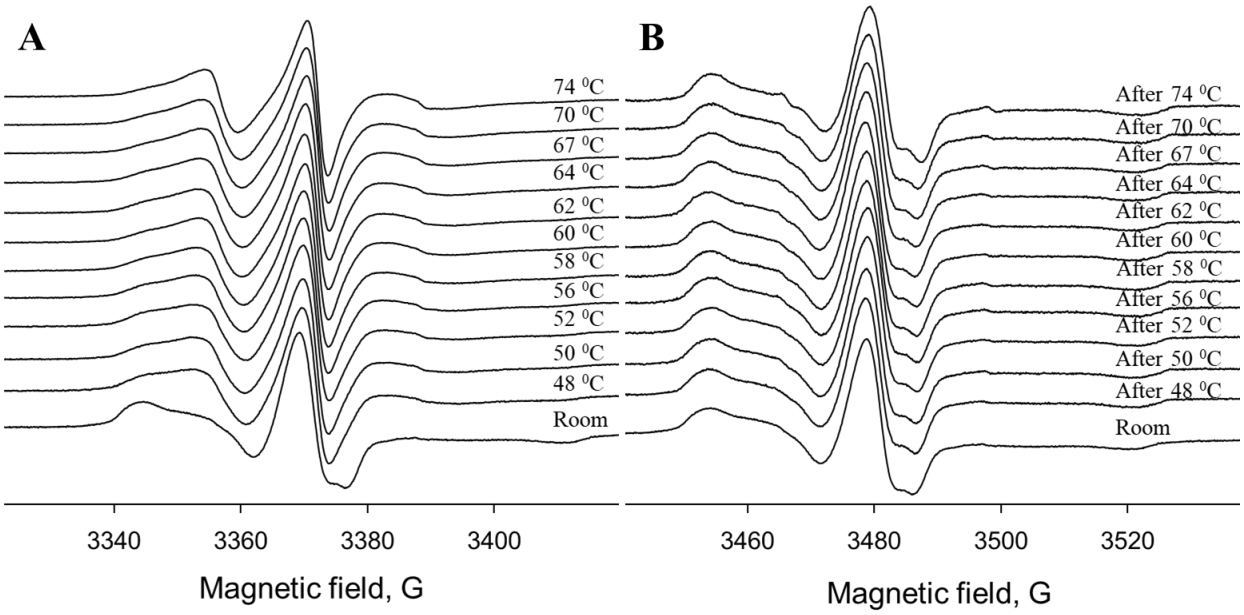

Figure 3.6. Thermal unfolding of N148C mutant monitored by CW EPR spectroscopy. (A) EPR spectra, each on measured at indicated temperature. (B) EPR spectra, each measured at room temperature after the sample exposure at indicated temperature.

After each heat treatment cycle, an EPR spectrum was acquired at room temperature for each of the mutants (Figure 3.6 B and Figure 3.7 B for N148C and S26C mutants respectively). All room temperature spectra demonstrate the same pattern: regardless of the treatment temperature that the protein was exposed to, each room temperature adapted sample showed spectral features corresponding to the slow-motion regime of the spin label indicating that the nitroxide is located in a conformationally restricted region. Moreover, all the room temperature adapted spectra were nearly identical to that measured prior to the heat treatments.

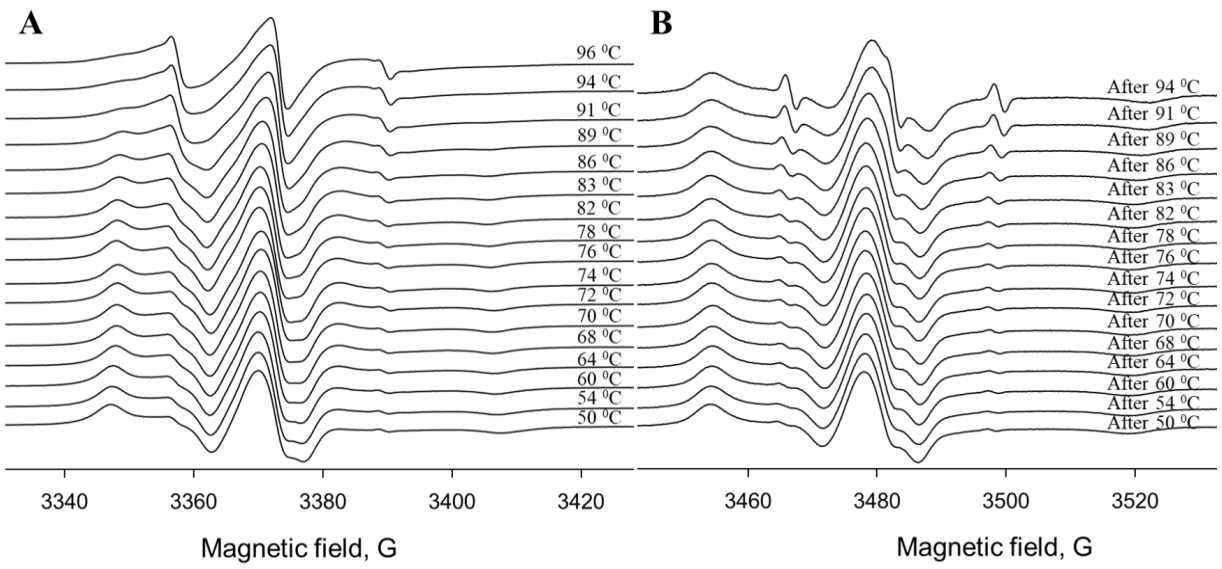

Figure 3.7. Thermal unfolding of S26C mutant monitored by CW EPR spectroscopy. (A) EPR spectra, each on measured at indicated temperature. (B) EPR spectra, each measured at room temperature after the sample exposure at indicated temperature.

This suggests, that after being exposed to elevated temperatures, the protein returns to its original folded conformation upon adapting it to room temperature. This in turn strongly indicates an important property: the unfolding process caused by the protein heat treatment is fully reversible, at least on the scale of the spin label conformational volume (~1nm).

It is important to note here however, that for S26C mutant (Figure 3.7 B) a very small fraction of free radical appeared on the EPR spectra corresponding to temperatures above ~70 ^{o}C gradually growing upon accumulation of the heat exposure. This could be due to incomplete labeling, which provides conditions for thiol-disulfide exchange reaction.[42]

For each of the measured EPR spectra the double integral over the magnetic field axis has been numerically calculated (Figure 3.8). Its value is proportional to the total number of spins in the sample and hence can be used to monitor the changes in the overall spin concentration. The

observed spin concentration remained roughly the same throughout the whole thermal unfolding process for N148C and started to decline at temperature above ~83 ^{o}C for S26C. At 89 ^{o}C, the S26C sample lost ~11% of its initial spin labels. After exposure to 91 ^{o}C the number of the spins decreased by ~19%. Eventually, at 94 ^{o}C, S26C sample retained about 77% of its original spin label concertation. However, the room temperature adapted spectrum measured after this heat treatment showed only a minor fraction of free label (in the order of 1%), suggesting that the signal intensity reduction might be due to a partial reduction of the nitroxide label occurring at higher temperatures. This effect is minor at lower exposure temperatures and becomes more pronounced at ~89 ^{o}C and above. It is also worth noting that the disulfide attachment of the spin probe is sufficiently stable.

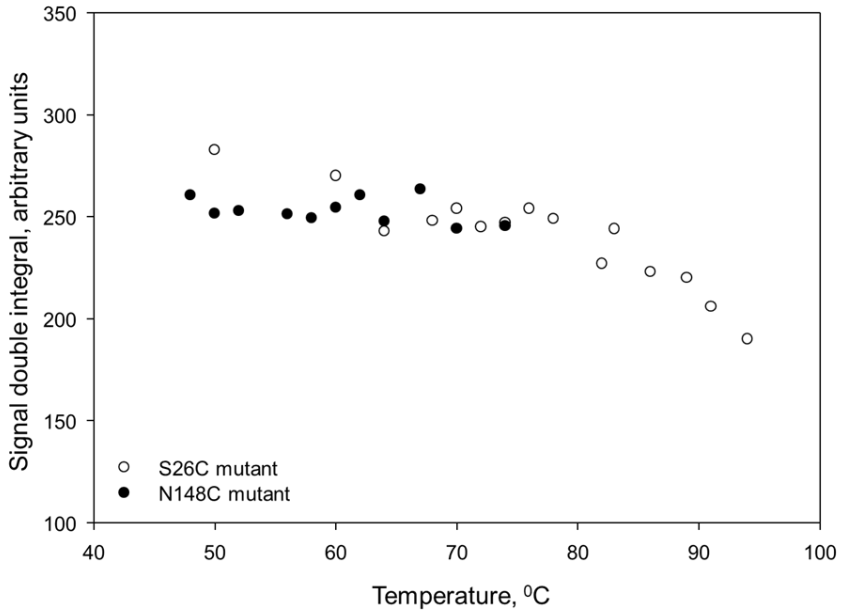

Figure 3.8. Dependence of the doubly integrated EPR signal measured for room temperature adapted samples on heat exposure temperature. Data correspond to S26C (open circles) and N148C (filled circles).

EPR spectra at intermediate range heat exposure temperatures represented a superposition of two fractions: corresponding to folded (native) and unfolded protein conformations (Figure 3.9), confirming the above suggested idea of a two-state folding process.

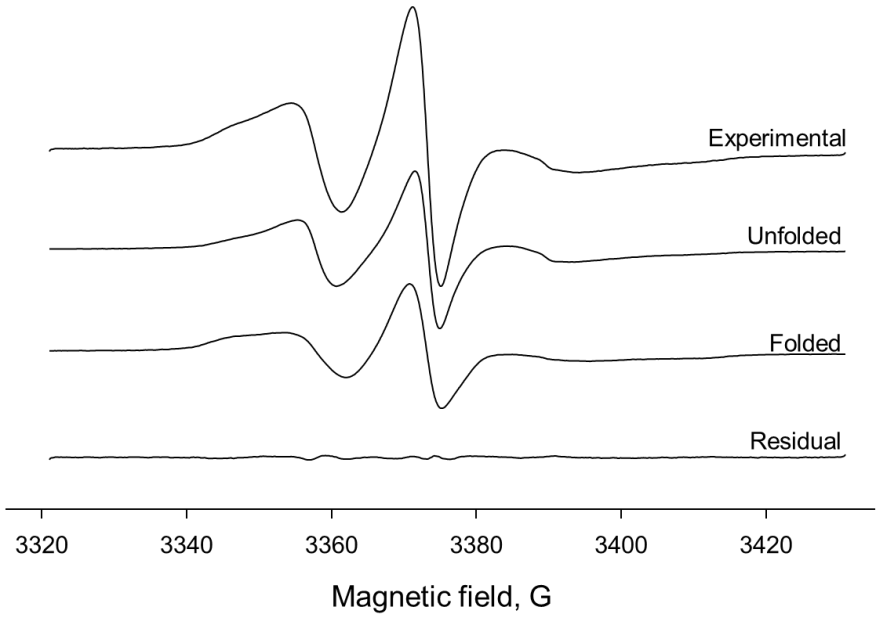

Figure 3.9. Numerical decomposition of the experimental EPR spectrum of N148C acquired at 64 ^{o}C into two fractions: corresponding to folded and unfolded state.

For each target temperature, the fraction of the unfolded ASR was determined and plotted as a function of the target temperature (Figures 3.10 A and 3.11 A for N148C and S26C mutants respectively). The sigmoidal shape of these functions is characteristic of a two-state transition process, providing another indirect confirmation of the proposed two-state folding model. Rather unexpectedly, the temperature related parameters of the s-shaped dependencies were found to be strikingly different for two mutants. Specifically, for N148C the unfolding transition was found to be approximately within the range of 52 ^{o}C to 70 ^{o}C with the denaturation midpoint (T_m) equal 62 ^{o}C. On the other hand, S26C site experienced thermal unfolding at 76 to 94 ^{o}C and $T_m \approx 88$ ^{o}C.

This indicates that the site on A-helix is thermodynamically more stable than on E-helix. In contrast to the inter-helical label at S26 position, the probe located in the loop region at N148 site faces the external environment, which imposes fewer conformation restrictions, resulting in substantially lower measured T_m.

Taking into account the fact that the experimental results suggest the unfolding process is reversible at least locally in the vicinity of the labeled sites, the Van't Hoff approach can be employed to estimate their unfolding activation parameters, namely reaction enthalpy $\Delta\mathbf{H}$ and reaction entropy $\Delta\mathbf{S}$. For that purpose, equilibrium constants were calculated using the following expression (calculated for each experimental temperature point):

$$K_{eq} = \frac{[unfolded]}{[native]} \tag{3.6}$$

where $[unfolded]$ and $[native]$ are unfolded and folded protein fractions, respectively.

Figures 8B-9B show dependencies of log-scaled K_{eq} on inverse temperature for N148C and S26C, respectively. Using the slopes and intercepts of the least square linear fits, the values of ΔH and ΔS for were estimated for both mutants and are summarized in Table 3.1. Alternatively, fractions can be fitted with a sigmoidal curve obtained from Van’t Hoff equation:

$$f = \frac{1}{1 + \frac{1}{K_{eq}}} = \frac{1}{1 + \exp\left(\frac{1}{R}\left(\frac{\Delta \mathrm{H}}{T} - \Delta \mathrm{S}\right)\right)} \tag{3.7}$$

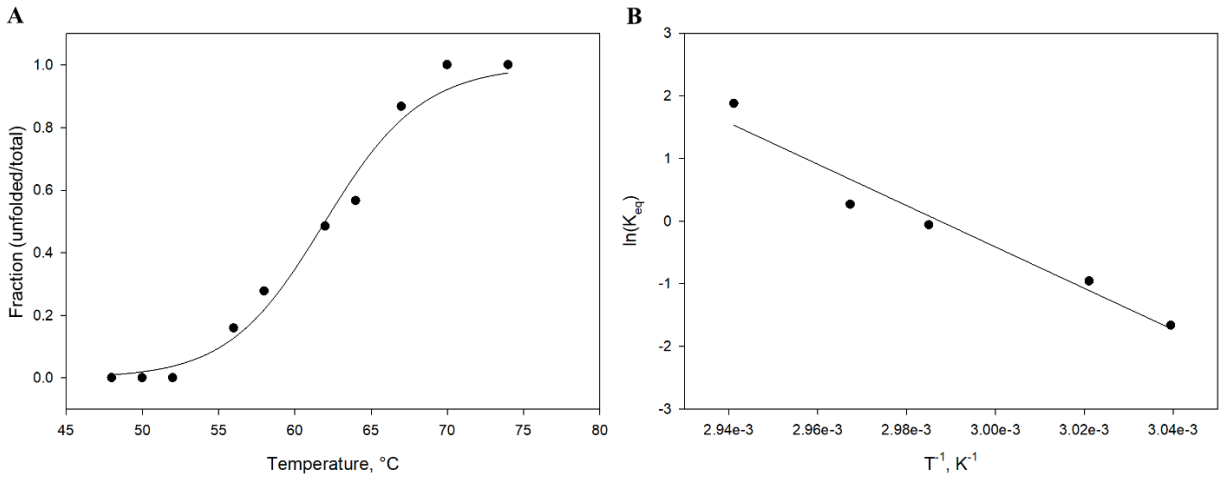

Figure 3.10. (A) Dependence of the unfolded fraction on heating temperature for the N148C mutant. Sigmoidal fit was obtained using eq.(3.7); (B) The corresponding Van‘t Hoff plot.

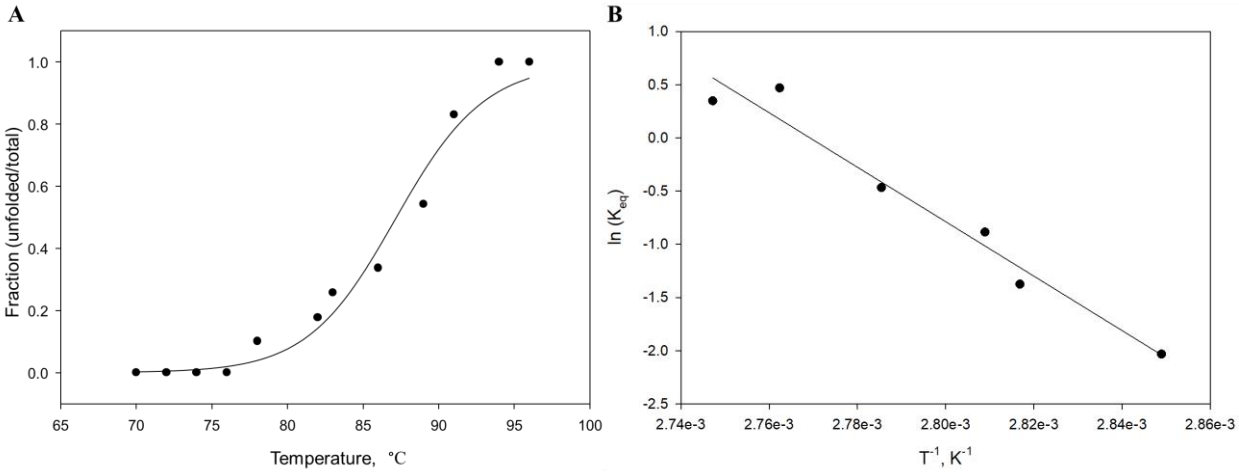

Figure 3.11. (A) Dependence of the unfolded fraction on heating temperature for the S26C mutant. Sigmoidal fit was obtained using eq.(3.7); (B) The corresponding Van‘t Hoff plot.

Table 3.1. Estimated values of thermal unfolding enthalpy (ΔH) and entropy (ΔS) for N148C and S26C mutants based on the Van‘t Hoff method.

Sample	**N148C**	**S26C**
[a] **ΔH, kcal*mol^{-1}**	70.24 ± 7.88	87.68 ± 10.75
[b] **ΔH, kcal*mol^{-1}**	65.60 ± 8.22	50.84 ± 4.99
[a] **ΔS, kcal*mol^{-1}*K^{-1}**	0.209 ± 0.023	0.243 ± 0.030
[b] **ΔS, kcal*mol^{-1}*K^{-1}**	0.196 ± 0.025	0.141 ± 0.014
T_m, ^oC	62.0 ± 0.4	87.3 ± 0.4

[a]The values are calculated based on the sigmoidal Van‘t Hoff fit, eq.(3.7) (Fig. 3.10 A and 3.11 A); [b]Calculationd based on the linear fit using classical Van‘t Hoff plot (Fig. 3.10 B and 3.11 B).

In order to further investigate the process of thermal unfolding a series of DEER experiments was performed for a sample containing spin labelled S26C mutant diamagnetically diluted (using the unlabeled S26C mutant) with 1:6 ratio (labeled to unlabeled ASR). It has been shown previously that DEER spectroscopy can be successfully applied to detect intra-monomer distances, while the interaction between trimers in hexagonal lattice contributes only to the background signal and their distance distribution cannot be extracted.[37] The distance between the labeled intra-trimer monomers (Figure 3.3) of the untreated sample was remeasured and found to be identical (within small experimental inaccuracy) to the previously reported 3.27 ± 0.26 nm[37] and taken as a reference for the following experiments.

As an attempt to capture the protein in its unfolded state, a rapid freeze trapping of thermally unfolded protein was applied. In the case of successful trapping, the distance was expected to change compared to the untreated sample. If in turn a subsequent DEER measurement

for the room temperature adapted sample provided the distance identical to the reference (distance in the untreated sample), that would provide additional support to suggested reversibility of the ASR unfolding. However, analysis of the acquired DEER traces did not reveal any noticeable changes in distance distribution between the freeze trapped and room temperature adapted samples (Figure 3.12). Considering the clear observation of thermal unfolding of ASR by CW EPR spectroscopy, one may conclude that the time scale of the freeze-trapping process might be insufficiently fast, thus providing enough time for the protein to relax to its folded state.

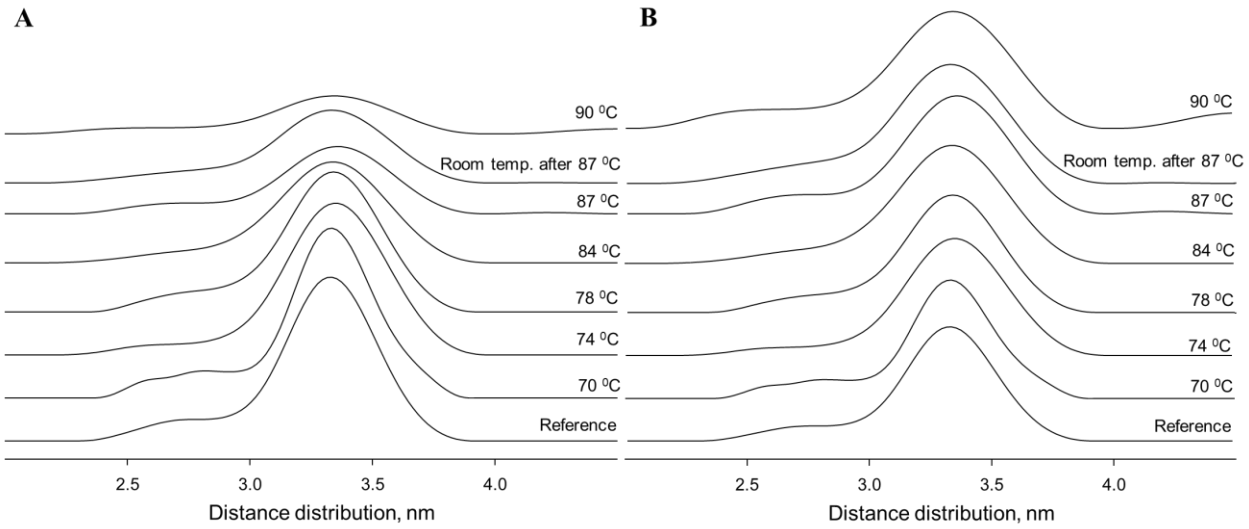

Figure 3.12. Distance distributions for the S26C ASR (1:6 diamagnetically diluted by the unlabeled trimers) freeze-trapped immediately after the heat exposure. The distance distributions of for the untreated sample (labeled as Reference) as well as for the sample exposed to 87 °C for 30 seconds and shock-frozen after being room temperature adapted are also shown. (A) raw (as extracted from the actual DEER traces) distributions; (B) normalized distributions.

Figure 3.12 shows distance distributions obtained for the heat-treated sample as well as the distance distribution measured for the untreated sample and used as a reference. All

distributions correspond to the same average intra-monomer distance that equals approximately 3.3 nm. The shape distance distribution was found to slightly broaden, and the value of its integral was found to decrease significantly with the increase of temperature of the heat exposure. The most likely explanation of this phenomenon is the inter-trimer monomer exchange process, which will be further discussed in more details.

Besides the shape of the distance distribution, the value of its first integral, which is directly proportional to the DEER signal modulation depth, Δ, is another useful source of information about electron spin-spin interactions. By monitoring the DEER modulation depth, one can analyze the labeled vs unlabeled fractions within the ASR trimers. The modulation depth of S26C sample with a paramagnetic dilution factor of 1:6 was measured and is shown in Figure 3.13A. Its value directly depends on the probability of more than one spin to be within the same ASR trimer. However, to properly assess this number, it is necessary to take into account the probability to excite a so called "pumped" spin during a DEER experiment. The equation that expresses DEER modulation depth, Δ, and the "pumped" spin excitation probability, λ was provided previously:[37]

$$\Delta = 2\lambda - \lambda^2 \tag{3.8}$$

Simple rearrangement of the equation yields:

$$\lambda = 1 - \sqrt{1 - \Delta} \tag{3.9}$$

DEER modulation depth as a function of heat exposure temperature (above 70 ^{o}C) is shown in the Figure 3.13A (filled circles), this includes modulation depth measured for the untreated sample (one empty circle). Corresponding spin excitation probabilities calculated using Equation 3.9 and subsequently normalized to yield 1.0 for the untreated sample are shown in Figure 3.13B. As can be seen, the cumulative heat exposure decreases spin excitation probability

, thus suggesting that fewer chance of two more spins to be within the same ASR trimer. This trend continues to a point where the normalized excitation probability reaches the value of $\lambda \approx 0.35 \pm 0.06$ for 90 ^{o}C. After that, λ showed only a minor decline ($\lambda \approx 0.26 \pm 0.03$) even upon dramatic increase of the heat exposure (3 minutes exposure at 84 ^{o}C) (Figure 3.13B, red circle). Moreover, the subsequent exposure for 6 min at 84 ^{o}C (Figure 3.13B, green circle) did not indicate any substantial change ($\lambda \approx 0.23 \pm 0.03$), suggesting that the sample approaches a plateau corresponding to the value of its lower bound. Existence of the non-zero lower bound for λ is more evident if λ is considered as a function of cumulative heat exposure. As a parameter characterizing, we have used a product of exposure time and trimer exchange rate introduced to the discus later. The corresponding plot is shown in Figure 3A.1 of Appendix 3A.

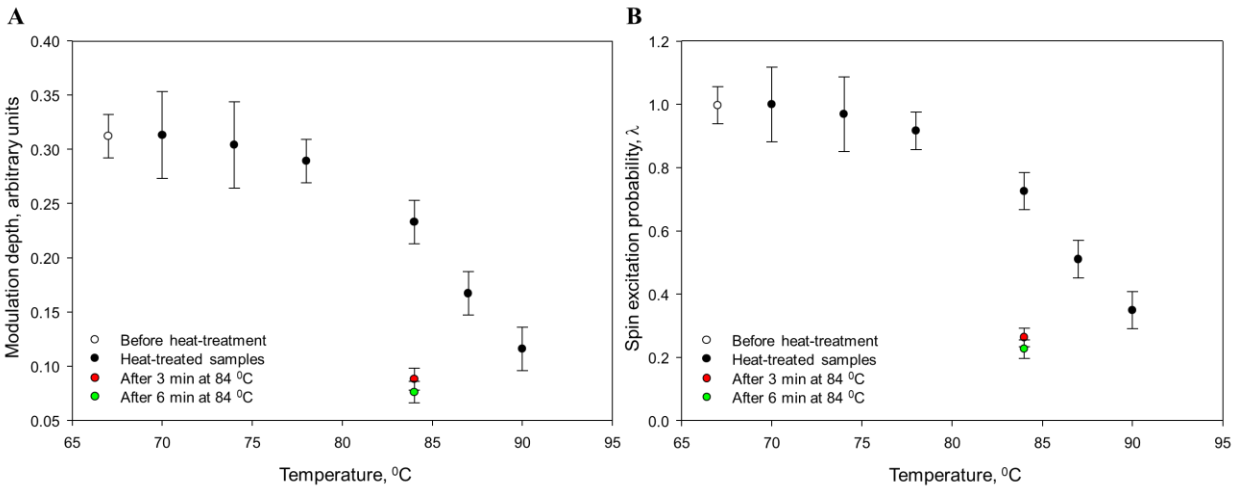

Figure 3.13. S26C sample with 1:6 diamagnetic dilution subjected to heat exposure at different temperatures (filled circles). The open circles show the untreated sample. Red and green circles show 3- and 6-min exposure at 84 ^{o}C, respectively. (A) DEER modulation depth (Δ). (B) Normalized spin excitation probability (λ).

To exclude the possibility that the λ decrease might be due to thermally induced disulfide bond breakage, which would result in a spin label detachment, CW spectra for several selected heat expose temperatures were acquired right after to the corresponding DEER experiments. The spectra are shown in Figure 3.14. The spectra were virtually to those previously measured to investigate the thermal unfolding (Figure 3.7 B). Only a very minor fraction of free label appeared after substantial cumulative heat exposure. However, the comparison of double integrals of the measured CW EPR spectra between 90 ^{o}C (for 30 sec) and 84 ^{o}C (for 6 min) spectra indicates more pronounced but still rather minor decay of spin concentration, by approximately 13%. This suggests that a small fraction of the spin label was reduced upon the cumulative heat exposure. However, in contrast to the previous experiment (Figure 3.8) the rates were much slower due to the shorter treatment time (30 sec vs 2 min), and subsequently smaller level of the cumulative heat exposure.

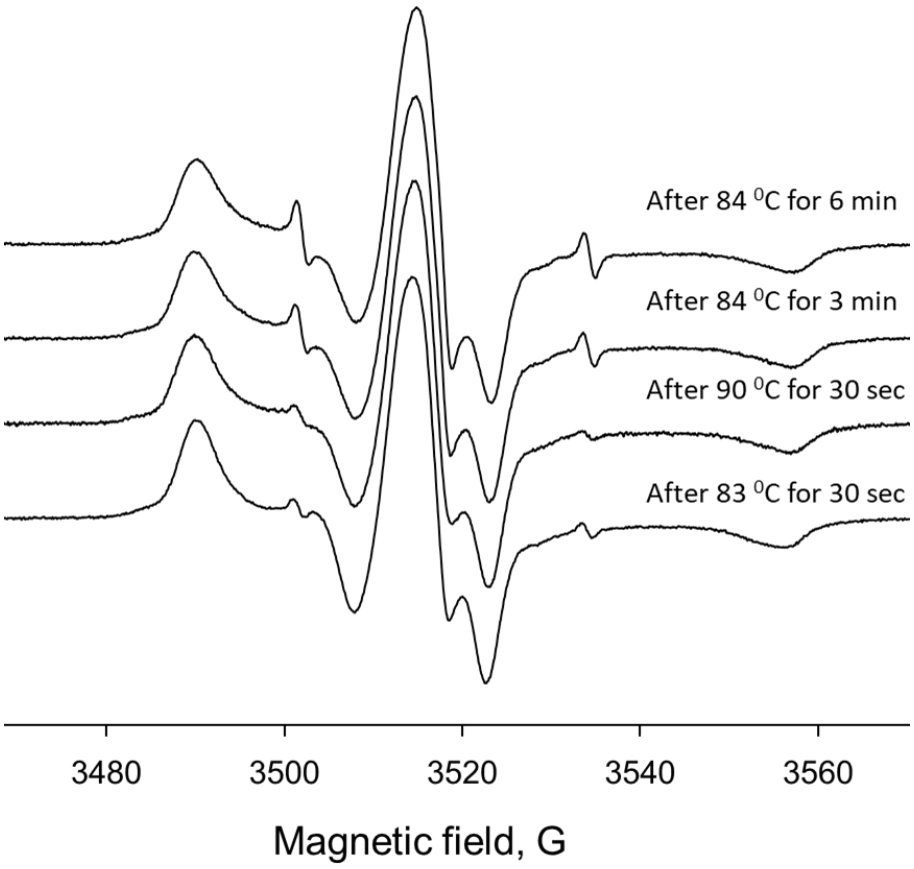

Figure 3.14. CW spectra of the 1:6 diamagnetically diluted S26C sample. The spectra were taken at room temperature after the indicated heat exposure.

The most probable reason for the modulation depth behavior upon the cumulative heat exposure could be explained using the specifics of ASR oligomerization. In a DEER experiment the echo amplitude and hence the monitored signal is proportional to the number of spins being excited by the "observer" pulses. Within a trimer an observer spin may interact with none, one or two "pumped" nitroxide spins , corresponding to one, two or three spin labeled monomers in a trimer, respectively. If there is zero spin labeled monomer in a trimer, no DEER signal is detected. If only one spin labeled monomer is present in the trimer, DEER signal is not modulated and represents pure background decay due to inter-molecular interactions. It has been shown

previously that upon solubilization and subsequent reconstitution in lipids, ASR trimers remain in their composition.[43,44] Therefore, it is expected that in untreated samples, the hexagonal lattice of ASR consists of a random mixture of fully labeled and fully unlabeled trimers. Once the sample is subjected to a substantial thermal stimulus, monomers from neighboring trimers exchange their positions, effectively "mixing" the oligomer compositions (Figure 3.15). This process continues until the protein lattice reaches its equilibrium state when the trimers represent a fully random combination of labeled and unlabeled monomers. This leads to the decrease of the observed DEER modulation via decrease of the probability of two or three spins to be within the sample ASR trimer (Figure 3.12 A). When the "randomization" process is complete for the 1:6 paramagnetic dilution sample, the probabilities to detect a trimer with two and three labeled monomers are 0.245 and 0.020, respectively. Considering that in each fully labeled trimer an observer spin interacts with two other spins, the average number of neighboring spins (within the same trimer containing the "observer" spin) is 0.285. That value is in good agreement with the estimated lower bound of the normalized excitation probability, λ, for the 1:6 ASR sample, ($\approx 0.26 \pm 0.03$), thus confirming the proposed inter-trimer monomer exchange mechanism. The small difference between the λ values corresponding to exposures at 84 ^{o}C (for 3 min) and 84 ^{o}C (for 6 min) (Figure 3.13 red and green circles) by a factor of 1.16 ± 0.20 times, is negligibly small and most likely attributed to a minor fraction of nitroxide being reduced.

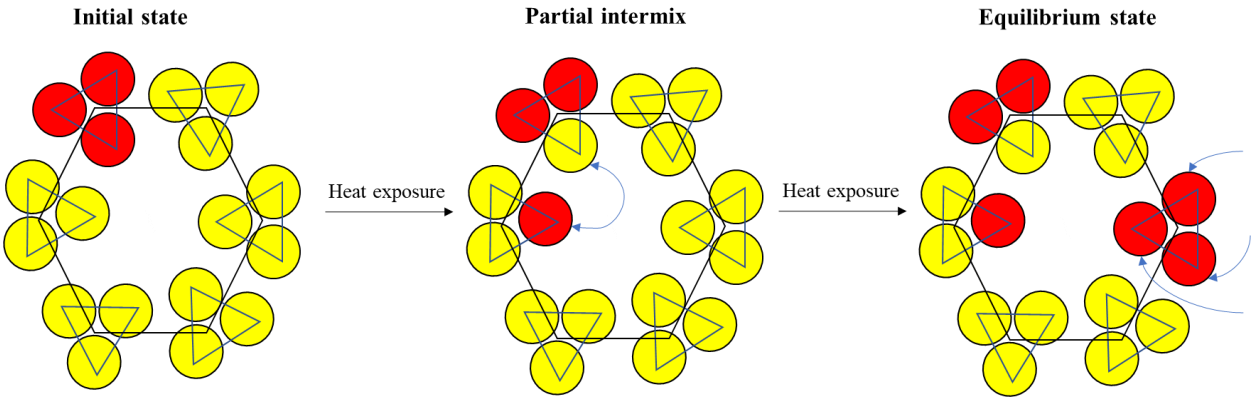

Figure 3.15. Cartoon representation of the inter-trimer monomer exchange mechanism for 1:6 dilution sample. Blue pointers indicate the exchange process. Initially, all hexamers contain either fully labeled (red circles) or unlabeled (yellow circles) monomers. After heat exposure, some labeled monomers exchange their positions with unlabeled ones. Finally, the sample reaches its fully "randomized" equilibrium state.

Assuming that the monomer exchange is the 1-st order kinetic process, the reaction rates can be estimated using the following equation:

$$\frac{d\lambda}{dt} = \frac{\lambda_0 - \lambda - \lambda_{lim}}{\tau} \tag{3.10}$$

where λ is current "pumped" spin excitation probability, λ_0 corresponds to the previous state, λ_{lim} is the lower bound that was estimated experimentally, t is the heat exposure time, τ is exchange time constant

The value of λ corresponding to the current state can be found:

$$\lambda = \lambda_0 e^{-rt} + \lambda_{lim} \tag{3.11}$$

where, exchange rate $r = 1/\tau$ was introduced.

Since the heat exposure was a series of subsequent events, Equation 3.11 can be rewritten in recursive form:

$$\lambda_i = \lambda_{i-1} e^{-r_i t} + \lambda_{lim} \tag{3.12}$$

Finally, simple rearrangement yields:

$$r_i = \frac{-\ln\left(\frac{\lambda_i - \lambda_{lim}}{\lambda_{i-1}}\right)}{t} \tag{3.13}$$

In general, the value of λ_{lim} depends on the paramagnetic dilution factor. In the case of 1:6 sample, its value can be estimated ad ≈0.26 ± 0.03, the value of λ corresponding to 3 min exposure time at 84 ^{o}C. The monomer exchange rates calculated using Equation 3.13 are shown as a function of exposure temperature in Figure 3.16 A.

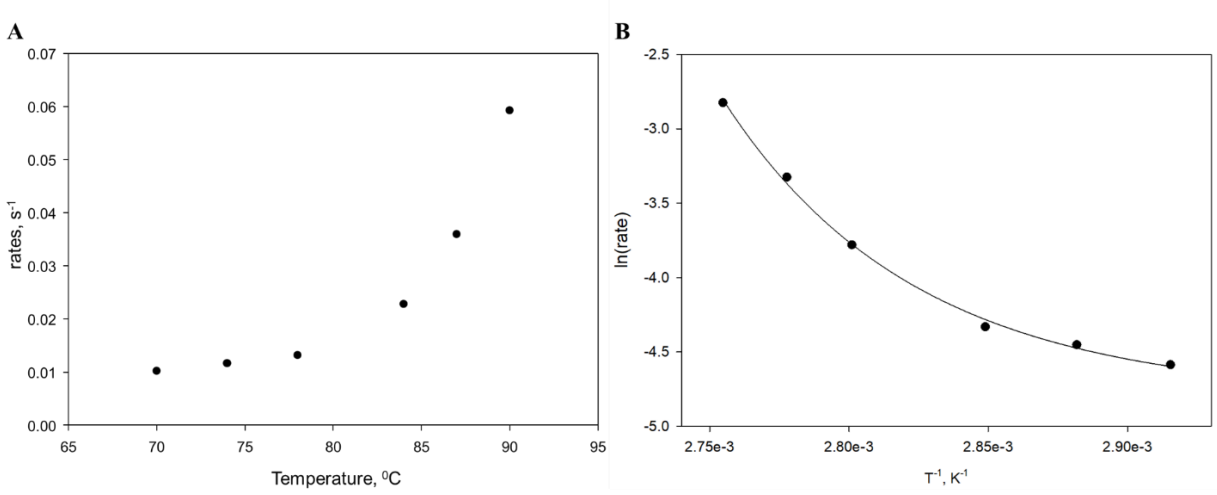

Figure 3.16. Calculated exchange rates and the corresponding d-Arrhenius plot for 1:6 ASR. (A) The rates calculated using Equation 3.13; (B) d-Arrhenius plot: the solid line represents the least square fit with the function provided in Equation 3.14. The function parameters can be found in Table 3.2.

Using the calculated rate values, it is possible to estimate activation energy for the monomer exchange process. For that purpose, natural logarithm of the rates is plotted against the reverse temperature (Figure 3.16 B). The graph demonstrates a profound concave shape, an indication that the activation energy grows as a function of temperature. Such process property is known in the literature as Sub-Arrhenius behavior.[45] Generally, it is observed in chemical reactions and attributed to quantum tunneling. However, in our case, the quantum tunneling is highly unprovable due do large size of the monomers. Thus, an alternative explanation of this experimental observation is required. One of the possible reasons for the observed temperature dependence of the calculated activation energy is that Equation 6 assumes the total number of spin labeled monomers to be unchanged during the duration of the experiment. In reality as we mentioned earlier, cumulative heat treatment results are minor but clearly observable chemical reduction of the nitroxide based labels. This, in turn would result in decrease of the observed monomer exchange rates and increase of the effective activation energies. Nevertheless, the Sub-Arrhenius can be used to take into account the observed non-linearity and estimate the barrier energy of the transition (E_0), employing the equation, known as deformed Arrhenius (d-Arrhenius):[45,46]

$$r(T) = A\left(1 - d\frac{E_0}{RT}\right)^{\frac{1}{d}} \tag{3.14}$$

where $r(T)$ is the temperature dependent rate constant, E_0 is the energy barrier, d is the deformation parameter, A is the empirical pre-exponential factor, T is the absolute temperature, R is the universal gas constant.

Equation 3.14 was used to fit the Sub-Arrhenius data. The corresponding results are summarized in Table 3.2.

Table 3.2. Parameters of the d-Arrhenius plot fitting for the 1:6 dilution ASR sample.

E_0, kcal mol^{-1} K^{-1}	**A - constant,** 10^{-3}	**d - constant**
76.60 ± 8.19	8.14 ± 0.68	-0.016 ± 0.002

To further confirm the proposed inter-trimer monomer exchange model and exclude the possibility of only spin label being exchanged between the non-exchangeable monomers, similar DEER measurements for the sample diamagnetically diluted with wild-type ASR (1:4 ratio) was conducted. The modulation depth and normalized "pumped" spin excitation probability are shown in the Figure 3.17 and compared to those obtained earlier for the sample diluted using the unlabeled S26C mutant (1:6 ratio).

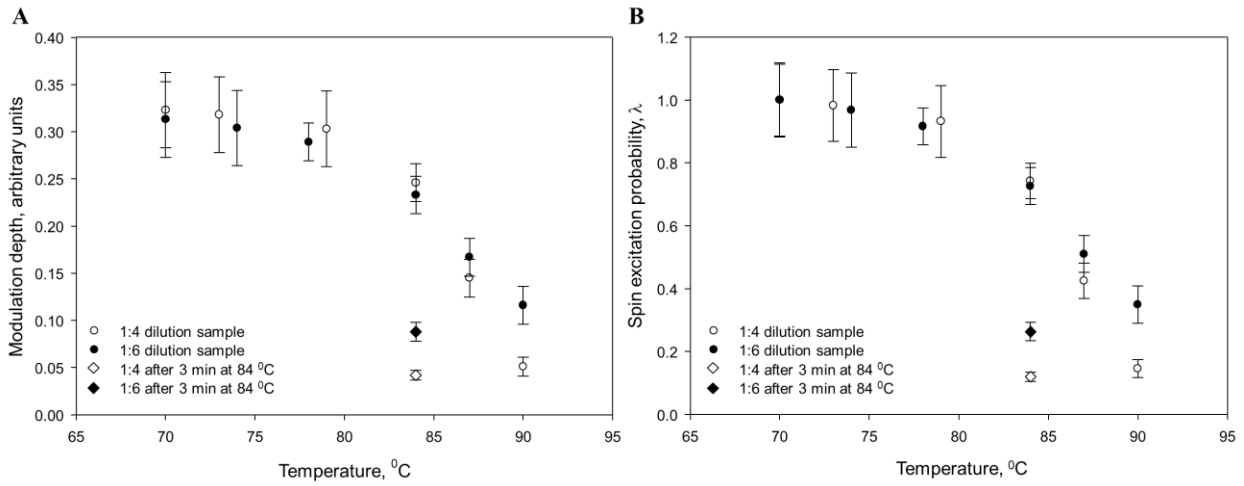

Figure 3.17. Comparison of DEER measurements for two different type of dilutions of spin labeled S26C ASR: 1:6 labeled/unlabeled and 1:4 labeled/wild-type. Circles represent heat-exposure at the indicated temperatures for 30 sec. Diamonds show the exposure at 84 °C for 3 min. (A) Comparison of the measured DEER modulation depths. (B) Comparison of the calculated normalized "pumped" spin excitation probabilities (λ).

For the untreated and low exposure temperatures, the observed modulation depth was nearly identical for both samples, as was expected due to fact that for untreated samples, the trimers are either fully labeled or fully unlabeled/wild-type. Therefore, the dilution factor did not have any effect before the heat-induced "mixing" started. During the heat-treatment, the samples showed similar rates of modulation depth decay until they were exposed to ~85 ^{o}C and above. Eventually, the normalized "pumped" spin excitation probability, λ, for the 1:4 dilution sample approached its plateau at the estimated lower bound of $\approx 0.15 \pm 0.03$. Further heat-treatment at 84 ^{o}C for 3 min (Figure 3.17, white diamond) did not show any significant change of the observed modulation depth. Assuming the inter-trimer monomer exchange model, it is expected that parameter λ for the 1:4 labeled/wild-type dilution sample would asymptotically approach the lower bound of ≈ 0.44, which 2.9 times higher than estimated experimentally.

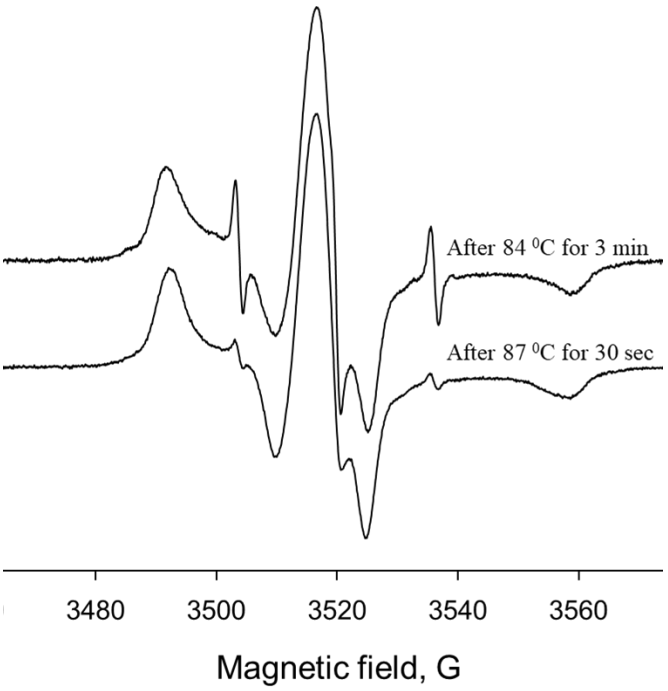

Figure 3.18. CW EPR spectra of 1:4 dilution ASR after corresponding heat-exposure. All spectra were acquired at room temperature.

To estimate the thermal stability of the spin label CW EPR spectra of the room temperature adapted samples after selected heat treatments were measured for the 1:4 dilution sample. The spectra, shown in the Figure 3.18 do not show a significant free label content, suggesting the similar level of disulfate bond stability as it was found earlier for the 1:6 dilution sample. As compared to 1:6 dilution, the double integral indicated an elevated level of signal decline. The CW EPR spectrum of the 1:4 diluted sample had a 1.28-times drop of its double integral value between the heat treatments indicated in Figure 3.18. In contrast, the double integral of the 1:6 sample in similar conditions decreased only by 1.13-times (between 90 ^{o}C (for 30 sec) and 84 ^{o}C (for 6 min) spectra). This is an indication that the most likely reason for the discrepancy between the expected and measured lower bounds of λ for the 1:4 dilution sample could be the increased reduction of the spin probe in case when the labeled S26C mutant is diluted with the wild-type ASR. While the spin concentration decrement between the indicated conditions was insufficiently large to fully explain the observed discrepancy, a cumulative effect of the additional heat exposures, especially those at high temperatures might be significantly larger. It is not entirely clear at this point, however, why the 1:4 dilution sample might have been more susceptible to chemical reduction of the nitroxide labels. Since these two samples were prepared independently, the possible explanation might be related to the sample preparation procedure. This yet unanswered question will be addressed in the future investigations.

3.4 Conclusions

Thermal unfolding of ASR monomers using a combination of CW EPR, pulsed EPR nitroxide site directed spin labeling was investigated, providing the local structure denaturation midpoint temperatures of 62 ^{o}C and 88 ^{o}C for N148 and S26 sites, respectively. The observed midpoint temperature difference is explained by higher steric restriction and thus lower

conformational freedom of the nitroxide label at S26C as compared to N148C site. This assumption is also confirmed by the lineshapes of the corresponding CW EPR spectra. It has been found that thermal unfolding of ASR is at least a locally (in the vicinity of the two investigated spin probe locations) reversible process. The unfolding enthalpy as well as entropy were estimated using Van't Hoff plot and summarized in Table 3.1.

DEER spectroscopy was used to investigate thermal effect on ASR oligomerization. While the proposed freeze-trapping procedure was proven to be insufficiently fast to capture the protein in the unfolded state, the obtained distance distributions showed that following the protein relaxation to its native structure, the inter-monomer distance remains unaffected by the heat exposure. This further confirmed the proposed idea of thermal unfolding being a reversible process. On the other hand, analysis of DEER modulation depths provided evidence of an irreversible monomer exchange between the trimers. Upon increased accumulation of the protein heat exposure, the DEER modulation depth approached a non-zero lower bound, suggesting that a fully random distribution of spin labeled monomers among all trimers. For the sample diamagnetically diluted with unlabeled S26C mutants (1:6 ratio), the observed lower bound for the normalized "pumped" spin excitation probability was in good agreement with the theoretical predictions. Thus, a thermally activated inter-trimer monomer exchange model was proposed. The kinetic and thermodynamic properties of the process were quantitatively characterized, providing the empirical temperature dependent exchange rates and an estimate of the exchange activation energy.

The same type of DEER experiments but using different type of diamagnetic dilution (1:4 dilution ratio using wild-type ASR) was conducted. While as expected the modulation depth as well as normalized "pumped " spin excitation probability exhibited presence of their lower non-

zero bounds, the observed value of the lower bound for the spin excitation probability was 2.9-times lower than predicted theoretically. The discrepancy was suggested to be due to sample preparation dependent chemical reduction of the nitroxides, which was not taken into account in the calculations.

To completely resolve the discrepancy, additional experiments are required, where simultaneously to the DEER measurements a detailed monitoring of the spin concentration in the sample is performed via CW EPR spectroscopy.

References

(1) Cournia, Z.; Allen, T. W.; Andricioaei, I.; Antonny, B.; Baum, D.; Brannigan, G.; Buchete, N.-V.; Deckman, J. T.; Delemotte, L.; Del Val, C.; Friedman, R.; Gkeka, P.; Hege, H.-C.; Hénin, J.; Kasimova, M. A.; Kolocouris, A.; Klein, M. L.; Khalid, S.; Lemieux, M. J.; Lindow, N.; Roy, M.; Selent, J.; Tarek, M.; Tofoleanu, F.; Vanni, S.; Urban, S.; Wales, D. J.; Smith, J. C.; Bondar, A.-N. Membrane Protein Structure, Function, and Dynamics: A Perspective from Experiments and Theory. *J. Membr. Biol.* **2015**, *248* (4), 611–640. https://doi.org/10.1007/s00232-015-9802-0.

(2) Muller, M. P.; Jiang, T.; Sun, C.; Lihan, M.; Pant, S.; Mahinthichaichan, P.; Trifan, A.; Tajkhorshid, E. Characterization of Lipid–Protein Interactions and Lipid-Mediated Modulation of Membrane Protein Function through Molecular Simulation. *Chem. Rev.* **2019**, *119* (9), 6086–6161. https://doi.org/10.1021/acs.chemrev.8b00608.

(3) Ng, D. P.; Poulsen, B. E.; Deber, C. M. Membrane Protein Misassembly in Disease. *Biochim. Biophys. Acta - Biomembr.* **2012**, *1818* (4), 1115–1122. https://doi.org/https://doi.org/10.1016/j.bbamem.2011.07.046.

(4) Stanley, A. M.; Fleming, K. G. The Process of Folding Proteins into Membranes: Challenges and Progress. *Arch. Biochem. Biophys.* **2008**, *469* (1), 46–66. https://doi.org/10.1016/j.abb.2007.09.024.

(5) Brown, L. S.; Jung, K. H. Bacteriorhodopsin-like Proteins of Eubacteria and Fungi: The Extent of Conservation of the Haloarchaeal Proton-Pumping Mechanism. *Photochem. Photobiol. Sci.* **2006**, *5* (6), 538–546.

(6) Brown, L. S. Eubacterial Rhodopsins - Unique Photosensors and Diverse Ion Pumps. *Biochim. Biophys. Acta* **2014**, *1837* (5), 553–561. https://doi.org/10.1016/j.bbabio.2013.05.006.

(7) Yutin, N.; Koonin, E. V. Proteorhodopsin Genes in Giant Viruses. *Biol. Direct* **2012**, *7*, 34. https://doi.org/10.1186/1745-6150-7-34.

(8) Palczewski, K. G Protein-Coupled Receptor Rhodopsin. *Annu. Rev. Biochem.* **2006**, *75*, 743–767. https://doi.org/10.1146/annurev.biochem.75.103004.142743.

(9) Hauser, A. S.; Attwood, M. M.; Rask-Andersen, M.; Schiöth, H. B.; Gloriam, D. E. Trends in GPCR Drug Discovery: New Agents, Targets and Indications. *Nat. Rev. Drug Discov.* **2017**, *16* (12), 829–842. https://doi.org/10.1038/nrd.2017.178.

(10) Spudich, J. L.; Yang, C. S.; Jung, K. H.; Spudich, E. N. Retinylidene Proteins: Structures and Functions from Archaea to Humans. *Annu. Rev. Cell Dev. Biol.* **2000**, *16*, 365–392.

(11) OESTERHELT, D.; STOECKENIUS, W. Rhodopsin-like Protein from the Purple Membrane of Halobacterium Halobium. *Nat. New Biol.* **1971**, *233* (39), 149–152. https://doi.org/10.1038/newbio233149a0.

(12) Palczewski, K.; Kumasaka, T.; Hori, T.; Behnke, C. A.; Motoshima, H.; Fox, B. A.; Le Trong, I.; Teller, D. C.; Okada, T.; Stenkamp, R. E.; Yamamoto, M.; Miyano, M. Crystal Structure of Rhodopsin: A G Protein-Coupled Receptor. *Science (80-.).* **2000**, *289* (5480),

739–745.

(13) Nango, E.; Royant, A.; Kubo, M.; Nakane, T.; Wickstrand, C.; Kimura, T.; Tanaka, T.; Tono, K.; Song, C.; Tanaka, R.; Arima, T.; Yamashita, A.; Kobayashi, J.; Hosaka, T.; Mizohata, E.; Nogly, P.; Sugahara, M.; Nam, D.; Nomura, T.; Shimamura, T.; Im, D.; Fujiwara, T.; Yamanaka, Y.; Jeon, B.; Nishizawa, T.; Oda, K.; Fukuda, M.; Andersson, R.; Båth, P.; Dods, R.; Davidsson, J.; Matsuoka, S.; Kawatake, S.; Murata, M.; Nureki, O.; Owada, S.; Kameshima, T.; Hatsui, T.; Joti, Y.; Schertler, G.; Yabashi, M.; Bondar, A.-N.; Standfuss, J.; Neutze, R.; Iwata, S. A Three-Dimensional Movie of Structural Changes in Bacteriorhodopsin. *Science (80-.).* **2016**, *354* (6319), 1552 LP – 1557. https://doi.org/10.1126/science.aah3497.

(14) Judge, P. J.; Watts, A. Recent Contributions from Solid-State NMR to the Understanding of Membrane Protein Structure and Function. *Curr. Opin. Chem. Biol.* **2011**, *15* (5), 690–695. https://doi.org/10.1016/j.cbpa.2011.07.021.

(15) Hendrickson, W. A. Atomic-Level Analysis of Membrane-Protein Structure. *Nat. Struct. Mol. Biol.* **2016**, *23* (6), 464–467. https://doi.org/10.1038/nsmb.3215.

(16) Shibata, M.; Yamashita, H.; Uchihashi, T.; Kandori, H.; Ando, T. High-Speed Atomic Force Microscopy Shows Dynamic Molecular Processes in Photoactivated Bacteriorhodopsin. *Nat. Nanotechnol.* **2010**, *5* (3), 208–212. https://doi.org/10.1038/nnano.2010.7.

(17) Ernst, O. P.; Lodowski, D. T.; Elstner, M.; Hegemann, P.; Brown, L. S.; Kandori, H. Microbial and Animal Rhodopsins: Structures, Functions, and Molecular Mechanisms. *Chem. Rev.* **2014**, *114* (1), 126–163. https://doi.org/10.1021/cr4003769.

(18) Kakitani, H.; Kakitani, T.; Rodman, H.; Honig, B. On the Mechanism of Wavelength Regulation in Visual Pigments. *Photochem. Photobiol.* **1985**, *41* (4), 471–479. https://doi.org/10.1111/j.1751-1097.1985.tb03514.x.

(19) Gabizon, R.; Friedler, A. Allosteric Modulation of Protein Oligomerization: An Emerging Approach to Drug Design. *Front. Chem.* **2014**, *2*, 9. https://doi.org/10.3389/fchem.2014.00009.

(20) Tsukamoto, T.; Kikukawa, T.; Kurata, T.; Jung, K. H.; Kamo, N.; Demura, M. Salt Bridge in the Conserved His-Asp Cluster in Gloeobacter Rhodopsin Contributes to Trimer Formation. *FEBS Lett* **2013**, *587* (4), 322–327. https://doi.org/10.1016/j.febslet.2012.12.022.

(21) Weik, M.; Patzelt, H.; Zaccai, G.; Oesterhelt, D. Localization of Glycolipids in Membranes by in Vivo Labeling and Neutron Diffraction. *Mol Cell* **1998**, *1* (3), 411–419.

(22) Tsukamoto, T.; Sasaki, T.; Fujimoto, K. J.; Kikukawa, T.; Kamiya, M.; Aizawa, T.; Kawano, K.; Kamo, N.; Demura, M. Homotrimer Formation and Dissociation of Pharaonis Halorhodopsin in Detergent System. *Biophys. J.* **2012**, *102* (12), 2906–2915. https://doi.org/10.1016/j.bpj.2012.05.008 S0006-3495(12)00561-9 [pii].

(23) Kato, H. E.; Zhang, F.; Yizhar, O.; Ramakrishnan, C.; Nishizawa, T.; Hirata, K.; Ito, J.; Aita, Y.; Tsukazaki, T.; Hayashi, S.; Hegemann, P.; Maturana, A. D.; Ishitani, R.;

Deisseroth, K.; Nureki, O. Crystal Structure of the Channelrhodopsin Light-Gated Cation Channel. *Nature* **2012**, *482* (7385), 369–374. https://doi.org/10.1038/nature10870.

(24) Bayburt, T. H.; Grinkova, Y. V; Sligar, S. G. Assembly of Single Bacteriorhodopsin Trimers in Bilayer Nanodiscs. *Arch. Biochem. Biophys.* **2006**, *450* (2), 215–222. https://doi.org/https://doi.org/10.1016/j.abb.2006.03.013.

(25) Shastri, S.; Vonck, J.; Pfleger, N.; Haase, W.; Kuehlbrandt, W.; Glaubitz, C. Proteorhodopsin: Characterisation of 2D Crystals by Electron Microscopy and Solid State NMR. *Biochim. Biophys. Acta* **2007**, *1768* (12), 3012–3019.

(26) Tong, Y.; Hughes, D.; Placanica, L.; Buck, M. When Monomers Are Preferred: A Strategy for the Identification and Disruption of Weakly Oligomerized Proteins. *Structure* **2005**, *13* (1), 7–15. https://doi.org/10.1016/j.str.2004.10.018.

(27) Shionoya, T.; Mizuno, M.; Tsukamoto, T.; Ikeda, K.; Seki, H.; Kojima, K.; Shibata, M.; Kawamura, I.; Sudo, Y.; Mizutani, Y. High Thermal Stability of Oligomeric Assemblies of Thermophilic Rhodopsin in a Lipid Environment. *J. Phys. Chem. B* **2018**, *122* (27), 6945–6953. https://doi.org/10.1021/acs.jpcb.8b04894.

(28) Heyn, M. P.; Cherry, R. J.; Dencher, N. A. Lipid-Protein Interactions in Bacteriorhodopsin-Dimyristoylphosphatidylcholine Vesicles. *Biochemistry* **1981**, *20*, 840–849.

(29) Dencher, N. A.; Heyn, M. P. Formation and Properties of Bacteriorhodopsin Monomers in the Non-Ionic Detergents Octyl-Beta-D-Glucoside and Triton X-100. *FEBS Lett* **1978**, *96* (2), 322–326. https://doi.org/0014-5793(78)80427-X [pii].

(30) Ikeura, Y.; Shimono, K.; Iwamoto, M.; Sudo, Y.; Kamo, N. Arg-72 of Pharaonis Phoborhodopsin (Sensory Rhodopsin II) Is Important for the Maintenance of the Protein Structure in the Solubilized State¶. *Photochem. Photobiol.* **2003**, *77* (1), 96–100. https://doi.org/https://doi.org/10.1562/0031-8655(2003)0770096AOPPSR2.0.CO2.

(31) Tsukamoto, T.; Demura, M.; Sudo, Y. Irreversible Trimer to Monomer Transition of Thermophilic Rhodopsin upon Thermal Stimulation. *J Phys Chem B* **2014**, *118* (43), 12383–12394. https://doi.org/10.1021/jp507374q.

(32) Shionoya, T.; Mizuno, M.; Tsukamoto, T.; Ikeda, K.; Seki, H.; Kojima, K.; Shibata, M.; Kawamura, I.; Sudo, Y.; Mizutani, Y. High Thermal Stability of Oligomeric Assemblies of Thermophilic Rhodopsin in a Lipid Environment. *J. Phys. Chem. B* **2018**, *122* (27), 6945–6953. https://doi.org/10.1021/acs.jpcb.8b04894.

(33) Kondoh, M.; Inoue, K.; Sasaki, J.; Spudich, J. L.; Terazima, M. Transient Dissociation of the Transducer Protein from Anabaena Sensory Rhodopsin Concomitant with Formation of the M State Produced upon Photoactivation. *J Am Chem Soc* **2011**, *133* (34), 13406–13412. https://doi.org/10.1021/ja202329u.

(34) Ward, M. E.; Wang, S.; Munro, R.; Ritz, E.; Hung, I.; Gor'kov, P. L.; Jiang, Y.; Liang, H.; Brown, L. S.; Ladizhansky, V. In Situ Structural Studies of Anabaena Sensory Rhodopsin in the E. Coli Membrane. *Biophys. J.* **2015**, *108* (7), 1683–1696. https://doi.org/10.1016/j.bpj.2015.02.018.

(35) Wang, S.; Munro, R. A.; Shi, L.; Kawamura, I.; Okitsu, T.; Wada, A.; Kim, S.-Y.; Jung, K.-H.; Brown, L. S.; Ladizhansky, V. Solid-State NMR Spectroscopy Structure Determination of a Lipid-Embedded Heptahelical Membrane Protein. *Nat. Methods* **2013**, *10* (10), 1007-+. https://doi.org/10.1038/nmeth.2635.

(36) Xiao, P.; Bolton, D.; Munro, R. A.; Brown, L. S.; Ladizhansky, V. Solid-State NMR Spectroscopy Based Atomistic View of a Membrane Protein Unfolding Pathway. *Nat. Commun.* **2019**, *10* (1), 3867. https://doi.org/10.1038/s41467-019-11849-8.

(37) Milikisiyants, S.; Wang, S.; Munro, R. A.; Donohue, M.; Ward, M. E.; Bolton, D.; Brown, L. S.; Smirnova, T. I.; Ladizhansky, V.; Smirnov, A. I. Oligomeric Structure of Anabaena Sensory Rhodopsin in a Lipid Bilayer Environment by Combining Solid-State NMR and Long-Range DEER Constraints. *J. Mol. Biol.* **2017**, *429* (12), 1903–1920. https://doi.org/10.1016/j.jmb.2017.05.005.

(38) Ward, M. E.; Wang, S.; Krishnamurthy, S.; Hutchins, H.; Fey, M.; Brown, L. S.; Ladizhansky, V. High-Resolution Paramagnetically Enhanced Solid-State NMR Spectroscopy of Membrane Proteins at Fast Magic Angle Spinning. *J Biomol NMR* **2014**, *58* (1), 37–47. https://doi.org/10.1007/s10858-013-9802-2.

(39) Wang, S.; Munro, R. A.; Kim, S. Y.; Jung, K.-H.; Brown, L. S.; Ladizhansky, V. Paramagnetic Relaxation Enhancement Reveals Oligomerization Interface of a Membrane Protein. *J. Am. Chem. Soc.* **2012**, *134* (41), 16995–16998. https://doi.org/10.1021/ja308310z.

(40) Pannier, M.; Veit, S.; Godt, A.; Jeschke, G.; Spiess, H. W. Dead-Time Free Measurement of Dipole–Dipole Interactions between Electron Spins. *J. Magn. Reson.* **2000**, *142* (2), 331–340. https://doi.org/http://dx.doi.org/10.1006/jmre.1999.1944.

(41) Jeschke, G. DEER Distance Measurements on Proteins. *Annu. Rev. Phys. Chem.* **2012**, *63*, 419–446. https://doi.org/10.1146/annurev-physchem-032511-143716.

(42) Bach, R. D.; Dmitrenko, O.; Thorpe, C. Mechanism of Thiolate−Disulfide Interchange Reactions in Biochemistry. *J. Org. Chem.* **2008**, *73* (1), 12–21. https://doi.org/10.1021/jo702051f.

(43) Wang, S.; Munro, R. A.; Shi, L.; Kawamura, I.; Okitsu, T.; Wada, A.; Kim, S. Y.; Jung, K. H.; Brown, L. S.; Ladizhansky, V. Solid-State NMR Spectroscopy Structure Determination of a Lipid-Embedded Heptahelical Membrane Protein. *Nat. Methods* **2013**, *10* (10), 1007–1012. https://doi.org/10.1038/nmeth.2635.

(44) Wang, S. L.; Munro, R. A.; Kim, S. Y.; Jung, K. H.; Brown, L. S.; Ladizhansky, V. Paramagnetic Relaxation Enhancement Reveals Oligomerization Interface of a Membrane Protein. *J. Am. Chem. Soc.* **2012**, *134* (41), 16995–16998. https://doi.org/10.1021/ja308310z.

(45) Silva, V. H. C.; Aquilanti, V.; De Oliveira, H. C. B.; Mundim, K. C. Uniform Description of Non-Arrhenius Temperature Dependence of Reaction Rates, and a Heuristic Criterion for Quantum Tunneling vs Classical Non-Extensive Distribution. *Chem. Phys. Lett.* **2013**, *590*, 201–207. https://doi.org/10.1016/j.cplett.2013.10.051.

(46) Mustakim, M.; Anil Kumar, A. V. Sub-Arrhenius Diffusion in a Classical System: Binary Colloidal Mixture in an External Potential. *Phys. A Stat. Mech. its Appl.* **2021**, *563*, 125462. https://doi.org/10.1016/j.physa.2020.125462.

Appendix 3A: Cumulative heat exposure

To assess the effect of the cumulative heat exposure, normalized "pumped" spin excitation probability (λ) were considered as a function of the cumulative parameter composed of the exchange rate multiplied by the corresponding exposure time. Figure 3A.1 shows the obtained results. The graphs are especially suitable to demonstrate that λ asymptotically approaches its non-zero lower bound.

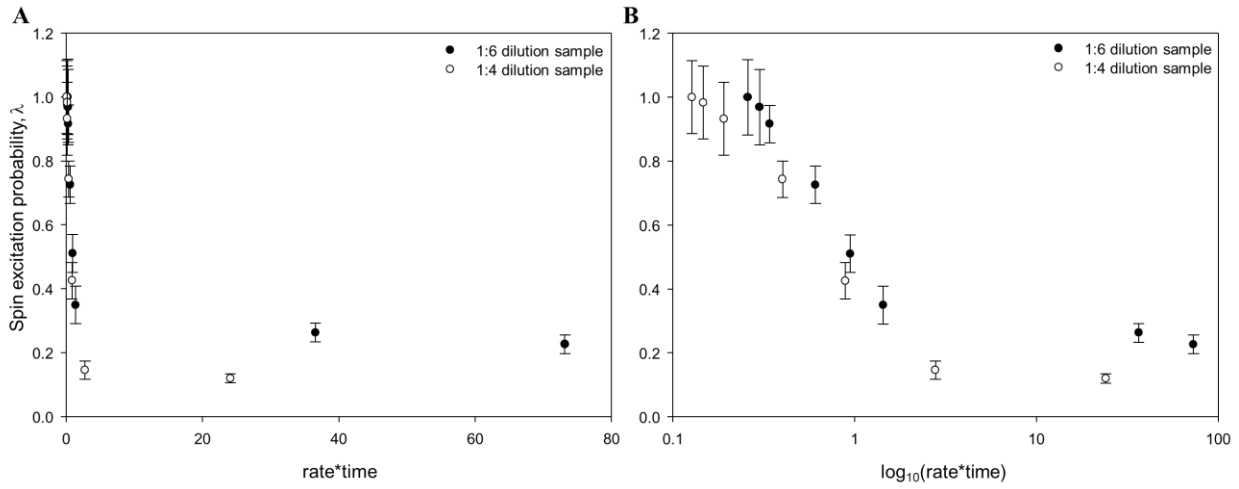

Figure 3A.1. Graphical representation of the effects of the cumulative heat exposure. (A) Spin excitation probabilities (λ) as a function of cumulative value of the inter-trimer exchange rate multiplied by the corresponding exposure time. (B) The same graph but plotted with a $\log_{10}$ scale for the vertical axis.